HEAT TRANSFER AND VISUALIZATION IN LARGE FLATTENED-TUBE CONDENSERS WITH VARIABLE INCLINATION

BY

WILLIAM A. DAVIES

THESIS

Submitted in partial fulfillment of the requirements
for the degree of Master of Science in Mechanical Engineering
in the Graduate College of the
University of Illinois at Urbana-Champaign, 2016

Urbana, Illinois

Adviser:

Professor Predrag S. Hrnjak

Abstract

An experimental study of convective condensation of steam in a large, inclined, finned tube is presented. This study extends previous work in the field on inclined, convective condensation in small, round tubes to large, non-circular tubes with low inlet mass flux of vapor. The steel condenser tube in this study was designed for use in a power-plant air-cooled-condenser array with forced convection of air. The tube was cut in half lengthwise and covered with a polycarbonate viewing window. The half tube had inner dimensions of 214mm x 6.3mm and a length of 10.72m. The viewing window allowed visualization of the steam flow and condensation. This study investigated heat transfer and void fraction results for a mass flux of steam of 7.5 kg/m^2-s over a range of inclination angles. The angle of inclination of the condenser tube was varied from 0.3^o (horizontal) to 13.2^o downward flow. The experiments were performed with uniform crossflowing air with velocity of 2 m/s. Both dropwise and filmwise condensation were observed on the tube wall, and depth of the condensate river at tube bottom was seen to decrease with an increase in inclination angle. Average steam-side heat transfer coefficient was shown to increase with an increase in inclination angle. However, average steam-side heat transfer coefficient was much lower than the predictions of both vertical flat-plate Nusselt condensation, as well as Kroger's correlation for condensation in air-cooled condensers. Overall, the results suggest that an improvement in steam-side heat transfer performance can be achieved by varying the tube inclination angle. Pressure drop results are presented in a companion paper.

Acknowledgments

I first and foremost must acknowledge and offer many thanks to my adviser, Dr. Predrag Hrnjak. He provided the inspiration and support for this project, and guided me through every step. Without his help, I would not have started, let alone finished this thesis. I would also like to thank Yu Kang, who toiled alongside me in building and testing this system, and kept on moving forward even during our many setbacks. I also owe a deep gratitude to Don Beeler and all of the employees of Creative Thermal Solutions (CTS) who always took time out of their days to help me with my work, show me around the facility, and teach me the basics of facility construction. All of my fellow grad students in the ACRC deserve my gratitude for sharing their hard-earned knowledge and time and inspiring me to keep moving forward in this research process. Special thanks must go out to Feini Zhang, who took time out of her own research to bring me into the clean room and help me use the goniometer. Another special thanks goes to Houpei Li, for taking the time to review and edit my thesis. I must acknowledge as well Dr. Anthony Jacobi, who was always able to provide encouragement, and not only solutions to my research problems, but a myriad of new directions to explore. I would also like to thank the sponsors, the National Science Foundation and the Electric Power Research Institute, for their support of the project. Finally, I must thank my parents, Bill and Candy Davies, my sister, Kim Davies, and my girlfriend, Maria Piñeros Leaño, for always being willing to chat, for keeping me on track, for showing interest in my work, and for just generally being great to spend time with.

Contents

List of Figures vi
List of Tables ix
Nomenclature x
Chapter 1: Introduction 1
Chapter 2: Literature Review 4
2.1 Internal Convective Condensation 4
2.2 Inclined Condensation 7
2.3 Non-Circular Ducts 12
2.4 Air-Cooled Condensers 13
Chapter 3: Experimental Facility 14
3.1 Overview 14
3.2 Measurements 16
3.3 Visualization Facility 19
Chapter 4: Visualization 21
4.1 Flow Pattern 21
4.2 Effect of Inclination 26
Chapter 5: Heat Transfer 29
5.1 Data Reduction 29
5.2 Heat Transfer Results and Discussion 31
Chapter 6: Conclusion 40
6.1 Summary 40
6.2 Future Work 41
Appendix A: Calculation of Condensate River Cross-Sectional Area 43
Appendix B: Air Velocity Measurement 47
Appendix C: Heat Loss Calibration 52
Appendix D: Air (T_{ao}) Temperature Profile 58
Appendix E: Energy Balance Verification 61
Appendix F: Contact Angle Measurements 62
Appendix G: Engineering Design 65
G.1 Inlet Steam Heater 65
G.2 Inlet Flow Guides 67
G.3 Air Duct and Fan Design 70
G.4 Wall Temperature Measurement 75

G.5 Condenser and Viewing Window 77
G.6 Avoiding Condensation on Viewing Window 80
G.7 T_{ao} Radiation Shield 84
G.8 Construction Drawings 86
Appendix H: Selected Temperature Measurements 89
Appendix I: Uncertainty 92
I.1 Instrument Uncertainties 92
I.2 Total Measurement Uncertainties 92
I.3 Uncertainties of Determined Quantities 94
References 99

List of Figures

Figure 1: Schematic diagram of a forced-convection air-cooled condenser (ACC) [2] 2
Figure 2: Diagram of vapor and condensate flow in condenser tube 2
Figure 3: Mixed Convection a) Horizontal Tube b) Vertical Tube [9] 7
Figure 4: Schematic drawing of condenser test facility 14
Figure 5: Photograph of condenser test facility raised to 13.2^o inclination 15
Figure 6: Test facility cross-section 16
Figure 7: Condenser cross-section with dimensions 16
Figure 8: Average air velocity per 1m section along the condenser, measured at the inlet…….. to the fins 17
Figure 9: Configuration of T_{ab} and T_{at} thermocouples. Fins were returned to proper……. angle after installation 18
Figure 10: Schematic drawing of temperature and pressure measurements 19
Figure 11: Mixed-mode condensation at z = 10m; left shows dropwise condensation…… and rivulets, right shows condenser surface before steam is run in order to clarify the……. 'wet' image 22
Figure 12: Schematic diagram of wavy condensate region 23
Figure 13: Waves in the condensate river caused by high-velocity vapor shear 23
Figure 14: Condensate river in transition section 24
Figure 15: Mixed-mode condensation near tube outlet 25
Figure 16: Mixed-mode condensation near tube outlet 25
Figure 17: Film condensation alongside dropwise condensation in vertical downward flow 26
Figure 18: Depth of condensate river at discrete locations along condenser, at……. six different inclination angles 27
Figure 19: Condensate river depth at different inclination angles, at five discrete points……. along the condenser 27
Figure 20: Schematic diagram of local heat transfer coefficient measurements…… a) condenser face; b) condenser cross-section 31
Figure 21: Steam-side heat transfer coefficient normalized to HTC in the horizontal…… inclination 32
Figure 22: Steam-side heat transfer coefficient vs. inclination angle 33
Figure 23: Measured steam-side heat transfer coefficient compared to predictions from……. Nusselt [3] and Kroger [22] 33
Figure 24: Air-side heat flux over 0-3m axial position along the condenser,……. normalized to the horizontal inclination 34
Figure 25: Air-side heat flux over 3-6m axial position along the condenser,…….. normalized to the horizontal inclination 34
Figure 26: Air-side heat flux over 6-9m axial position along the condenser,……. normalized to the horizontal inclination 34
Figure 27: Air-side heat flux over 9-10.7m axial position along the condenser,…….. normalized to the horizontal inclination 34
Figure 28: q'_a and v_a along the condenser for 0.3^o inclination 35
Figure 29: q'_a and v_a along the condenser for 2.87^o inclination 35
Figure 30: q'_a and v_a along the condenser for 6.0^o inclination 35
Figure 31: q'_a and v_a along the condenser for 8.7^o inclination 35

Figure 32: q'_a and v_a along the condenser for 11.7^o inclination 36
Figure 33: q'_a and v_a along the condenser for 13.2^o inclination 36
Figure 34: Normalized air-side heat flux vs air velocity 36
Figure 35: Normalized heat flux along the condenser controlled for variations in……..
air velocities 37
Figure 36: Heat flux along the condenser normalized to inlet heat flux at the horizontal……..
inclination 38
Figure 37: Local steam-side heat transfer coefficient, from wall temperature 39
Figure 38: Physical model of the flattened tube of Cheng et al. [17] 44
Figure 39: Schematic diagram of condensate in half-tube..... 45
Figure 40: Assumptions of condensate river consisting of two right triangles above…….
the main flow 45
Figure 41: Air velocity measurement points..... 48
Figure 42: Anemometer in position to measure air velocity at middle of fins. Note…….
screws covering 1/11 of duct face area. 48
Figure 43: Air velocity per section, and average air velocity for the entire condenser 49
Figure 44: TSI Anemometer calibration results..... 49
Figure 45: Anemometer calibration facility..... 50
Figure 46: Heat loss at three different inlet temperatures, along with line of best fit 53
Figure 47: Schematic diagram of condenser cross-section during heat loss calibration 53
Figure 48: Modeled velocity and measured temperature profiles in air duct 58
Figure 49: Schematic drawing of air temperature measurement 58
Figure 50: Axial fan profile for fluent model 59
Figure 51: Velocity vectors of airflow in air duct. A high velocity gradient is present in…….
the vicinity of the Tao measurement..... 59
Figure 52: Clean condenser face..... 63
Figure 53: Rusted condenser face 63
Figure 54: Static water droplet on rusted condenser surface 63
Figure 55: Static water droplet on clean condenser surface 63
Figure 56: Advancing water droplets on rusted condenser surface 64
Figure 57: Advancing water droplets on clean condenser surface 64
Figure 58: Receding water droplet sequence on rusted condenser surface 64
Figure 59: Receding water droplet sequence on clean condenser surface..... 64
Figure 60: Fluent simulation of inlet vapor flow without flow guide..... 67
Figure 61: Schematic diagram of flow in header flow guides 68
Figure 62: Polycarbonate header flow guide 69
Figure 63: Inlet header before installing flow guide..... 69
Figure 64: Polycarbonate header flow guide 69
Figure 65: Polycarbonate header flow guide 69
Figure 66: Header flow guide being inserted in header..... 69
Figure 67: Mesh for CFD model of air flow through air duct 70
Figure 68: 80mm fan x-velocity profile..... 71
Figure 69: Maximum velocity in air duct, average velocity at vertical cross section at……..
midpoint of constant-size duct section..... 72
Figure 70: X-Velocity pathlines for 60mm fan design 72
Figure 71: X-Velocity pathlines for 80mm fan design 73

Figure 72: X-Velocity pathlines for 100mm fan design 73
Figure 73: magnitude of x-velocity at a cross section halfway along straight duct section 74
Figure 74: Residuals for 100mm fan design; the 60mm and 80mm designs required……
fewer iterations to reach convergence..... 74
Figure 75: Position of wall thermocouples 75
Figure 76: Wall thermocouple embedding methods: hole drilled completely……..
through wall, tight hole, large hole 76
Figure 77: Results of three different measurement techniques and three different x locations.... 77
Figure 78: End view of full-tube condensers and fins 77
Figure 79: Side view of condenser tube and fins 78
Figure 80: Schematic drawing of half-tube cross section with viewing window 78
Figure 81: Construction diagram of condenser half-tube cross-section 79
Figure 82: Construction drawing of test facility cross-section 79
Figure 83: Schematic diagram of two-pane viewing window with heated wires 81
Figure 84: Condensation on viewing window with two-pane polycarbonate and heated wires... 84
Figure 85: 3-D model of supports for radiation shield 85
Figure 86: 3-D rending of radiation shield supports on thermocouple probe..... 85
Figure 87: Supports for radiation shield on probe 86
Figure 88: Installed radiation shield 86
Figure 89: Air duct construction drawing..... 87
Figure 90: Air duct top segment construction drawing 87
Figure 91: Polycarbonate viewing window construction drawing 88
Figure 92: 3-D rendering of condenser tube, air duct, and supporting truss;……
pink insulation slid back to show detail below 88
Figure 93: T_{satt}, T_{satb}, T_{wt}, T_{wb} along condenser at 0.3^o inclination..... 89
Figure 94: T_{ai}, T_{ao}, v_a along condenser at 0.3^o inclination 89
Figure 95: T_{satt}, T_{satb}, T_{wt}, T_{wb} along condenser at 6.0^o inclination..... 90
Figure 96: T_{ai}, T_{ao}, v_a along condenser at 6.0^o inclination 90
Figure 97: T_{satt}, T_{satb}, T_{wt}, T_{wb} along condenser at 13.2^o inclination..... 91
Figure 98: T_{ai}, T_{ao}, v_a along condenser at 13.2^o inclination 91
Figure 99: Uncertainty in Q_a at 13.2^o inclination..... 95
Figure 100: Uncertainty in condensation heat transfer coefficient..... 96

List of Tables

Table 1: System operating parameters 16
Table 2: Cross-sectional area of condensate river for numerical full-tube and experimental half-tube 28
Table 3: Contact angle and capillary rise of the condensate river on steel and polycarbonate 45
Table 4: Cross-sectional area of condensate river in numerical model and experimental results 46
Table 5: Velocity profile along fin height 48
Table 6: Heat transfer surface areas and UA values, both theoretical and measured 56
Table 7: UA_{loss} values for steam-side and air-side 56
Table 8: Position of and correction factors for Tao measurements 60
Table 9: Water inlet temperature, water and air heat transfer, and % error 61
Table 10: Static, advancing and receding contact angles for water on clean condenser tube 63
Table 11: Static, advancing and receding contact angles for water on rusted condenser tube 63
Table 12: Properties of thermal resistances on viewing window 81
Table 13: Summary of leading causes of uncertainty in h_s calculation 97

Nomenclature

A	Area	$[m^2]$
c_p	specific heat	$[J\ kg^{-1}\ K^{-1}]$
D	Diameter	[m]
G	mass flux	$[kg\ m^{-2}\ s^{-1}]$
g	Gravity	$[m\ s^{-2}]$
h	heat transfer coefficient	$[W\ m^{-2}\ K^{-1}]$
H	Height	[m]
i_{fg}	enthalpy of vaporization	$[J\ kg^{-1}]$
i	specific enthalpy	$[J\ kg^{-1}\ K^{-1}]$
k	thermal conductivity	$[W\ m^{-1}\ K^{-1}]$
L	Length	[m]
LMTD	log mean temperature difference	$[^0\ C]$
Nu	Nusselt Number	
Q	heat transfer	[W]
q’	heat flux	$[W\ m^{-1}]$
r	Radius	[m]
R	resistance to heat transfer	$[m^2\ K\ W^{-1}]$
t	Thickness	[m]
T	Temperature	$[^0\ C]$
u	uncertainty	
U	overall heat transfer coefficient	$[W\ m^{-2}\ K^{-1}]$
V	Velocity	$[m\ s^{-1}]$
$\dot{V}$	volumetric flow rate	$[m^3\ s^{-1}]$
W	Width	[m]
x	position along condenser height; quality	[m]; [-]
y	position perpendicular to tube face (along width)	[m]
z	position along condenser axis	[m]
α	void fraction	
B	volumetric expansion coefficient	$[K^{-1}]$

δ	capillary rise of condensate river	[mm]
θ	contact angle	[^{o}]
μ	Viscosity	[kg m^2 s]
ρ	density	[kg m^{-3}]
σ	line tension	[N m^{-1}]
φ	inclination angle	[^{o}]
X	Lockhardt-Martinelli parameter	

Subscript

1P	single-phase
2P	two-phase
a	air
atm	atmospheric
b	bottom
c	condensate
F	fin
f	fluid
g	gas
h	hydraulic
i	in
ins	insulation
loss	Heat transfer to ambient
nc	natural convection
o	out
pc	polycarbonate
pvc	polyvinyl chloride
s	steam
sat	saturation
sf	surface
sh	superheat

st	steel
T	tube
t	top
tt	turbulent-turbulent
w	wall

Chapter 1: Introduction

The macro-scale objective of this project is to improve the performance of a forced-convection air-cooled power plant condenser (ACC). ACCs are commonly used in dry regions that lack the large water source necessary for power-plant cooling. In the United States, approximately 0.9% of electricity is produced using ACCs. However, as demand for water increases and water-use regulations become stricter, their use will need to be expanded to less arid regions. Most water in use for power generation is withdrawn from a large fresh-water source (lake, river, reservoir), and then returned at a higher temperature. Thermoelectric power generation accounts for the largest proportion of freshwater withdrawals in the US, reaching 41% in 2005. However, increasing ACC use to 25% by 2035 could reduce US water withdrawals by 10.7%[1].

In addition to reducing water use, ACCs reduce the risk of Legionnaires' disease. Legionnaires' disease is a respiratory infection caused by bacteria that is commonly found in wet cooling towers. ACCs eliminate the large, damp areas where the bacteria can grow.

ACCs in power plants consist of an array of flattened steel tubes arranged in an A-frame configuration. The tubes have aluminum fins on each flat face. The steam inlet header is located at the top of the 'A' to allow for gravity-driven flow of condensate. Axial fans providing air flow are located at the frame base, as seen in figure 1. The condensate will typically drain into a receiver or pre-heater at the bottom of the condenser. A typical ACC array will have dozens of condensing steel tubes, each inclined at an angle of up to 60° to the horizontal.

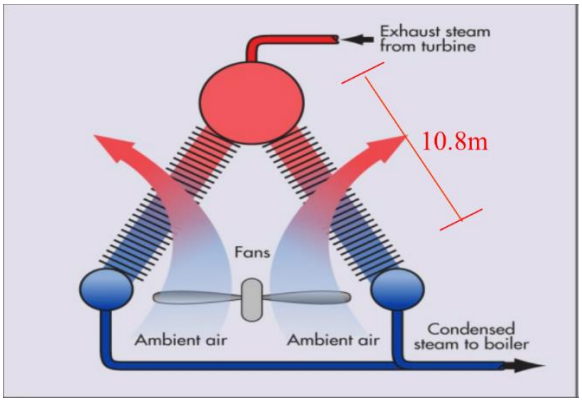

Figure 1: Schematic diagram of a forced-convection air-cooled condenser (ACC) [2]

For this investigation, the condensation of steam inside one 10.72 m flattened condensing tube will be observed and measured. Specifically, flow visualization and characterization will be performed, and steam-side heat transfer coefficient (HTC), heat flux, and void fraction will be analyzed along the length of the condenser. In addition, the effect of condenser inclination on each of these parameters will be investigated.

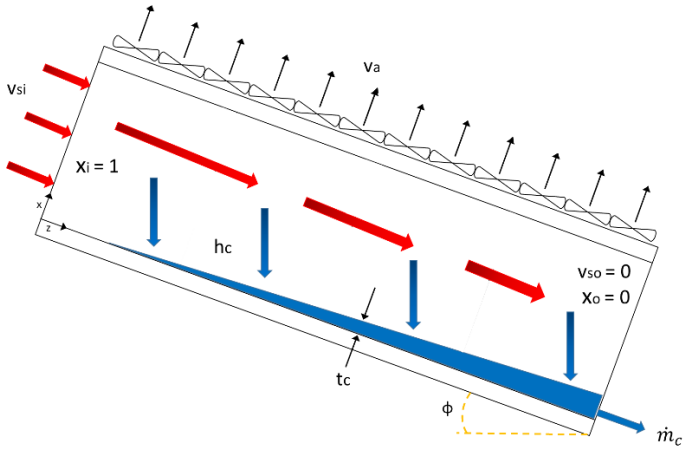

Figure 2: Diagram of vapor and condensate flow in condenser tube

As seen in Figure 2, steam flow occurs along the tube axis (z-direction). Steam enters with an inlet Reynolds number of approximately 7,500 and a velocity of 11 m/s, and decelerates to zero at the end of the tube. Condensate flows in two directions. A condensate film falls vertically along the tube wall due to gravity. Along the bottom of the tube face, a condensate river flows along the

tube length primarily due to gravity, but also aided by shear forces from the steam flow. The height of the condensate river increases along the tube length, due to the increasing volume of condensate. The condensate river acts as an extra resistance to heat transfer. Therefore, the steam-side heat transfer coefficient decreases along the length of the tube as the condensate river increases in depth.

The air-side heat transfer coefficient is independent of z position along the tube for a uniform air velocity, but heat transfer is highest at the air inlet, x = 0m, due to the large temperature difference.

Based on previously published work, an increase in the tube inclination angle, φ, is expected to decrease the height of the condensate river, and therefore increase the average steam-side heat transfer coefficient. These effects should be greater near the tube outlet, where the quality is lower and the area of the condenser covered by the condensate river is greater. For a constant inlet mass flux of steam, condenser capacity should also increase with increased inclination angle.

In order to verify these hypotheses, average steam-side heat transfer coefficient for the condenser and local steam-side heat transfer coefficient at twelve points along the tube length, L, were determined. In order to understand the mechanisms of these changes, a visualization study was performed in parallel to view the condensation and condensate flow regimes.

A companion study investigates pressure drop at each inclination. By combining these two studies, a recommendation for optimum inclination angle with regards to steam-side heat transfer and pressure drop performance can be made.

Chapter 2: Literature Review

This study investigates an inclined, flattened tube with internal convective condensation in both dropwise and filmwise modes, with a focus on air-cooled condenser (ACC) applications. Each of these physical aspects and phenomena have been studied individually, but never in this combination. Of these, internal, convective condensation is the most-studied aspect.

2.1 Internal Convective Condensation

Due to the high aspect ratio and low mass flux of steam, the classical film condensation model presented by Nusselt [3] serves as a rough approximation of the ACC internal condensation, and can serve as a lower bound for heat transfer. Nusselt's model assumes laminar film condensation and gravity-driven flow. The mean heat transfer coefficient over a flat plate is:

$$\bar{h} = 0.943 \left[\frac{i_{fg} \rho_f (\rho_f - \rho_g) g k_f^{\,3}}{W \mu_f (T_{sat} - T_w)} \right]$$

Where W, the condenser width, is the length parallel to gravity.

For flow through ducts, heat-transfer correlations are more commonly used, however. Derived from experimental results and physical principles, they simplify the complex phenomena that occur during turbulent convection condensation. Among the more recent experimental and analytical analyses for internal convective condensation, those correlations by Shah [4], Soliman et al.[5], Traviss et al. [6] and Chato [7] are the most commonly used. The correlation of Chato is

most applicable to this investigation, because it models separated flow at low mass fluxes. Chato assumes separated vapor and condensate flow, with filmwise condensation on the tube walls and a pool of condensate flowing along the tube bottom. In addition, because vapor velocity falls to zero at the tube exit, vapor shear along the condensate film is negligible for the downstream portion of the tube. Chato predicted that heat transfer through the laminar condensate layer would be by conduction only, making heat transfer through this layer negligible compared to that along the condenser wall. Therefore, heat transfer will decrease as the thickness of this layer increases.

Chato showed that the critical depth of the condensate flow along the tube bottom depended primarily on flow rate and tube dimensions:

$$\frac{h_c}{d_o} = 0.4212\left(\sqrt{\frac{\alpha}{\beta}}\frac{\dot{V}}{\sqrt{g r_o^5}}\right)$$

$$\sqrt{\frac{\alpha}{\beta}} = 1.4 \; for \; Re < 3000$$

$$\sqrt{\frac{\alpha}{\beta}} = 1.1 \; for \; Re > 3000$$

$$h_c = critical \; depth \; of \; condensate \; flow$$

$$d_o = tube \; diameter$$

$$r_o = tube \; radius$$

$$\dot{V} = volumetric \; flow \; rate$$

Chato's resulting correlation for internal convective condensation heat transfer coefficient, valid for inlet vapor Reynolds numbers below 35,000, is:

$$h = 0.728K_C \left[\frac{g\rho_f(\rho_f - \rho_g)k_f^3 i'_{fg}}{\mu_l(T_{sat} - T_w)D_h}\right]^{1/4}$$

$$i'_{fg} = i_{fg}\left[1 + 0.68\frac{c_{pf}(T_{sat} - T_w)}{i_{fg}}\right]$$

In a later study, Jaster and Kosky [8] found that K_C varied with void fraction as:

$$K_C = \alpha^{3/4}$$

$$\alpha = \left[1 + \frac{1-x}{x}\left(\frac{\rho_g}{\rho_f}\right)\right]^{-1}$$

In an ACC, however, where the inlet steam flow is in the turbulent regime and transitions to laminar and finally stagnation at the condenser outlet, it is difficult to characterize the heat transfer by one of the traditional correlations. For example, near the tube outlet, where steam flow rate is very low, free convection may become important. For this case, Metais and Eckert [9] have defined a criterion to determine whether free convection is important. This graphical criterion is based on the relationship between Reynolds number and Grashof and Prandtl numbers for the flow.

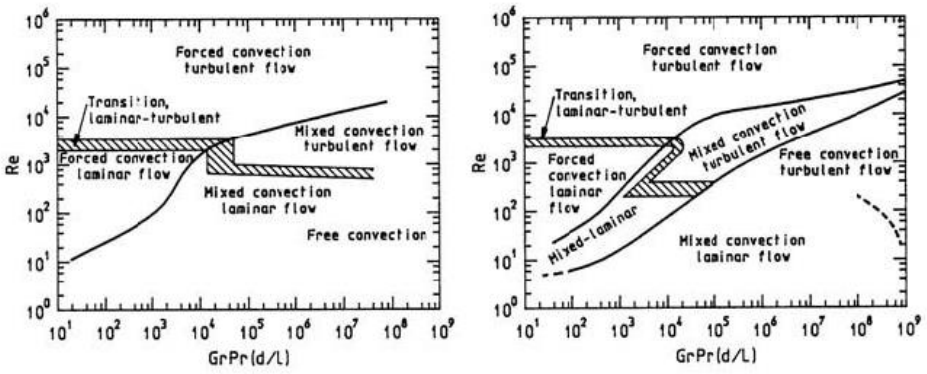

Figure 3: Mixed Convection a) Horizontal Tube b) Vertical Tube [9]

The Grashof number is defined as:

$$Gr = g\rho^2 D_h^3 \beta (T_w - T_{sat})/\mu^2$$

2.2 Inclined Condensation

For internal steam condensation, inclined convective condensation in a large, flattened tube has yet to be studied experimentally. However, numerous authors have studied downwardly inclined condensation in cylindrical tubes. Regardless of tube size, all of the theoretical analyses predict an increase in heat transfer coefficient for an increasing inclination angle. The experimental investigations, however, have produced mixed results, showing that the effect of inclination is moderated by other variables, most notably tube diameter, vapor quality and mass flux. In general, for large tubes, and low quality and mass flux, condensation heat transfer coefficient has been shown to at first increase with increasing inclination angle, then decrease after reaching a critical angle. The value of this critical angle has varied, depending on the study.

Therefore, while in-tube convective condensation has been studied extensively, strong correlations between heat transfer coefficient and moderating variables has left the effect of varying tube inclination not fully defined.

In an early study, both analytical and experimental, Chato [7] showed that heat transfer will increase for a slightly inclined tube versus horizontal, but it will decrease upon reaching a critical inclination angle. Assuming that any change in condensate depth was gradual, Chato derived the following equation for heat transfer through the bottom condensate:

$$\frac{q'}{L} = \frac{2k_f \Delta t}{\pi - \varphi} ln\left[\frac{d_o \sin^2 \varphi}{y_{so}} - 1\right]$$

$$L = tube\ length$$

$$k_f = thermal\ conductivity\ of\ liquid$$

$$\varphi = tube\ inclination$$

$$y_{so} = wall\ condensate\ film\ thickness\ at\ surface\ of\ bottom\ flow$$

For average heat transfer coefficient, he added a multiplier to the horizontal-flow correlation:

$$h = \left(0.728 K_C \left[\frac{g\rho_f(\rho_f - \rho_g)k_f^3 i'_{fg}}{\mu_l (T_{sat} - T_w) D_h}\right]^{\frac{1}{4}}\right) cos^{\frac{1}{4}} sin^{-1}(\varphi)$$

However, he suggests that for steeper angles, the correlation will change due to changes in flow regime.

More recent studies by Lips and Meyer [10], Noie et al. [11], and Lyulin et al. [12] have also shown that heat transfer coefficient at first increases for an increasing inclination angle in downward flow before reaching a critical angle and then decreasing to a lower heat transfer

coefficient in vertical downward flow. In their study with R134a in an 8.38mm diameter tube, Lips and Meyer showed that the optimum inclination angle for heat transfer coefficient occurred between 15° and 30°. Noie et al. studied an inclined thermosiphon with a diameter of 14.5mm and water as the working fluid. They found a similar result of 30-45° as the optimum angle. Lyulin et al. [12] studied low mass flux of condensing ethanol in a 4.8mm tube, and found a maximum HTC between 15 and 35° inclination. Even more recently, Olivier, et al. [13] expanded on the study of Lips and Meyer [10] to conclude that for low mass flux and quality, HTC and void fraction reach a maximum at 10-30° inclination in downward condensing flow.

Wurfel et al. [14] also found that heat transfer coefficient increased with increasing inclination angle. However, their experiment showed that heat transfer coefficient increased until reaching a maximum at vertical downward flow. They used a larger tube than the above-mentioned studies, 2cm, and studied n-heptane in shear-dominated flows. They developed a correlation for their results:

$$\frac{Nu}{Nu_o} = (1 + sin\beta)^{0.214}$$

Nu_o is the Nusselt number for a horizontal orientation.

In contrast to the above studies, Akhavan –Behabadi et al. [15] found that heat transfer coefficient decreased for all downward inclination angles. Like Lips and Meyer, they used R134a with high mass fluxes, but in a microfin tube. The correlation they developed is:

$$Nu = 1.09{Re_f}^{0.45} F_\varphi^{0.3} \sqrt{\frac{Pr_f}{\mathrm{X}_{tt}}}$$

Where,

$$Nu = \frac{\bar{h}D}{k_f}$$

$$Re_f = \frac{GD(1-x)}{\mu_f}$$

$$Pr_f = \frac{\mu_f c_{p,f}}{k_f}$$

$$\mathrm{X}_{tt} = \left(\frac{\rho_g}{\rho_f}\right)^{0.5} \left(\frac{\mu_g}{\mu_f}\right)^{0.1} \left(\frac{1-x}{x}\right)^{0.9}$$

$$F_\varphi = (1 + (1-x)^{0.2} \cos(\varphi - 10^o))/x^{0.4}$$

The previous work by Wang and Du [16] has clarified these mixed results by testing a range of small-diameter tubes at a range of mass fluxes and qualities. Their work is very relevant to the current study in that they examined steam at loss mass flux, albeit in much smaller tube diameters than that investigated here. Their results showed an increase in Nusselt number for increasing inclination in smaller tubes. For larger tubes, Nusselt number only increased at low qualities, and Nusselt number averaged across all qualities decreased. This study served to confirm that the effect of inclination is often overpowered by the effects of diameter, quality, and mass flux.

Other researchers have provided further insight by measuring related parameters in inclined tubes. Cheng et al. [17] used a numerical model to predict the depth of the condensate river for film condensation in a flattened ACC tube for tube inclination angles varying from 5 to 85º. They predicted that the maximum depth of the condensate river at the tube bottom would vary from 2.1 to 0.8 mm, corresponding to an increase in the tube inclination angle. Beggs and Brill [18] developed a correlation for void fraction for all tube inclinations, for both upward and downward flow:

$$1-\alpha=(1-\alpha_o)\left[1+C(sin1.8\varphi-\frac{1}{3}\sin^3 1.8\varphi)\right]$$

The mixed results of these studies perhaps indicate the reason for the durability of the correlation by Shah [4], which is applicable for all inclination angles, even though does not include inclination angle in the correlation. The effects of other parameters are often more important than the effect of inclination. One caveat is that the applicability of Shah's correlation does not extend to the large diameter and low mass fluxes encountered in this study.

$$h_{shah}=h_{dittus-boelter}\left[(1-x)^{0.8}+\frac{3.8x^{0.76}(1-x)^{0.04}}{(P/P_c)^{0.38}}\right]$$

$$h_{dittus-boelter}=0.023\left(\frac{k_f}{D}\right)\left(\frac{GD}{\mu_f}\right)^{0.8}{Pr_f}^{0.4}$$

In addition to the experimental correlations, two analytical solutions may be particularly applicable to this experiment. The modified Nusselt theory of Carey [19], developed for annular film condensation in downflow, is applicable to the low mass flux of this experiment.

$$\frac{hD}{k_f}=0.028{Re_f}^{0.9}{Pr_f}^{1/2}\left(1+\frac{20}{\mathrm{X}_{tt}}+\frac{1}{\mathrm{X}_{tt}^2}\right)^{1/2}$$

$$Re_f=\frac{G(1-x)D}{\mu_f}$$

X_{tt} is the Martinelli parameter for turbulent liquid-turbulent vapor flow.

$$\mathrm{X}_{tt}=\left(\frac{\rho_g}{\rho_f}\right)^{0.5}\left(\frac{\mu_g}{\mu_f}\right)^{0.125}\left(\frac{1-x}{x}\right)^{0.875}$$

Schulenberg [20] studied the specific case of low-pressure steam condensing in inclined tubes in air-cooled condensers. Using the correlation of Schulenberg, Kroger [21] assumed that all of the steam in tube would condense, and simplified the correlation to:

$$Nu_c = 1.197(sin\varphi)^{0.1755}\left(\frac{\rho_c}{\mu_c}\right)^{0.5}\left(\frac{\mu_g}{\rho_g}\right)^{0.5} Re_{gi}^{0.325}$$

Where Re_{gi} is the Reynolds number of the steam entering the tube.

2.3 Non-Circular Ducts

For laminar, fully-developed single-phase flow in rectangular ducts, analytical solutions exist for Nusselt number for both a constant wall temperature and a constant heat flux. Shah and London [22] have provided curves through these points:

$$Nu_T = 7.541\left[1 - 2.610\frac{b}{a} + 4.970\left(\frac{b}{a}\right)^2 - 5.119\left(\frac{b}{a}\right)^3 + 2.702\left(\frac{b}{a}\right)^4 - 0.548\left(\frac{b}{a}\right)^5\right]$$

$$Nu_{q"} = 8.235\left[1 - 2.0421\frac{b}{a} + 3.0853\left(\frac{b}{a}\right)^2 - 2.4765\left(\frac{b}{a}\right)^3 + 1.0578\left(\frac{b}{a}\right)^4 - 0.1861\left(\frac{b}{a}\right)^5\right]$$

For the ACC, with an aspect ratio of approximately 3/32, this will yield Nu_T = 6.0 and h_s = 110 W/m^2-K. Jamil [23] and Zarling [24] continued this analysis for ducts with circular ends, but Kroger [21] showed that these solutions converge for aspect ratios less than 1/5. In a circular duct, laminar, fully-developed, single-phase flow yields Nu_T = 3.66. Although both results are single phase, the large increase in Nu_T for flattened tubes indicates that the two-phase inclined

correlations for circular tubes may be under-predicting the heat transfer coefficient for the ACC condenser.

2.4 Air-Cooled Condensers

Air-cooled condensers (ACCs) have been studied extensively in the context of natural-draft dry cooling towers. In this realm, much of the research and design work has been in improving the air-side heat transfer performance, particularly with regards to ambient winds and physical layout of the condenser arrays. For example, Wu et al. [25] developed a computational model of air-side flow and heat transfer under ambient winds for two arrangements of condensers. Hooman [26] used scale analysis, assuming the condenser arrays were a porous medium, to verify the numerical results. Wei et al. [27] acquired full-scale experimental results in a wind tunnel to verify the airflow results.

For forced-convection ACCs, several studies have proposed improvements to the air side of the condenser. For example, Gadhamshetty et al. [28] proposed a chilled-water thermal energy storage system to cool the inlet air. In simulations for a 171 MW power plant in New Mexico, their design would increase net power output by 2.5%. None of the studies found investigated improvements to the steam-side performance.

Chapter 3: Experimental Facility

3.1 Overview

Steam was provided to the condenser by two boilers controlled by solid-state controllers, with capacities of 24 and 27 kW, respectively. An inlet heater and choke valve ensured that the steam was superheated at the condenser inlet. At the condenser outlet, condensate drained by gravity into a receiver, and a condensate pump refilled the boilers when the condensate receiver had filled.

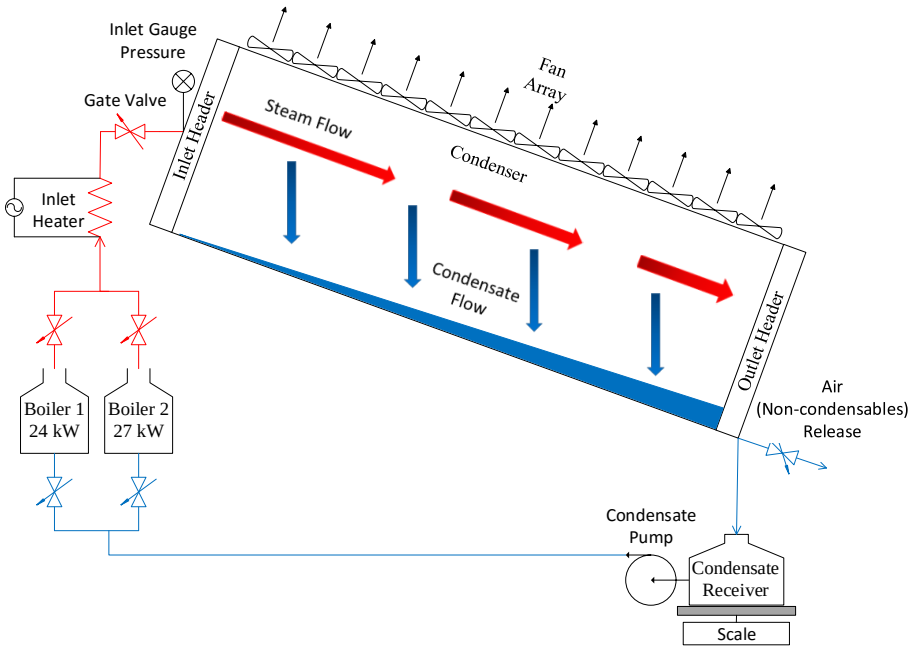

Figure 4: Schematic drawing of condenser test facility



Figure 5: Photograph of condenser test facility raised to 13.2º inclination

The tube was cut in half lengthwise in order to perform simultaneous visualization with the heat transfer and pressure drop measurements. The half tube was covered with a polycarbonate sheet to allow for visual access. The half-tube carbon-steel condenser had a major diameter of 214 mm and a minor diameter of 6.3 mm. The inner perimeter of the condenser, not including the polycarbonate window, was 222 mm. The fin length was 200 mm and the height was 19 mm. Air flow was provided by an array of 134 axial fans with diameter of 80 mm, arranged to pull air upwards through the aluminum fins. The fans were adjustable via 1kohm potentiometers, to allow measurement of various air velocity profiles. Both the air duct and the viewing window were insulated with 2" polystyrene foam insulation. The half tube configuration and dimensions can be seen in Figure 6 and Figure 7, respectively.

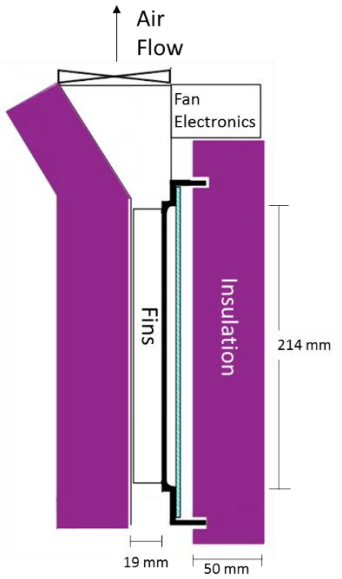

Figure 6: Test facility cross-section

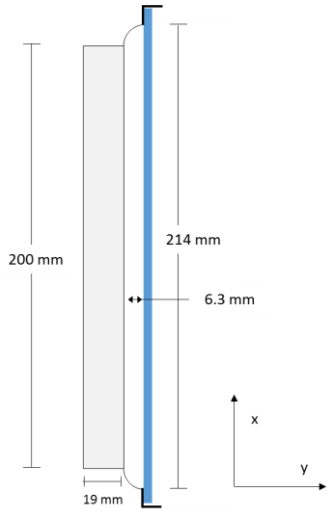

Figure 7: Condenser cross-section with dimensions

The range of operating parameters and their uncertainties are displayed in Table 1.

Table 1: System operating parameters

Parameter	**Range**	**Uncertainty**
Inlet vapor mass flux [kg m^{-2} s^{-1}]	6.5	±1
Mass flow rate [g s^{-1}]	10	±1
Condenser capacity [kW]	25.2 – 29.1	±3%
Air velocity (average) [m s^{-1}]	2.03	±7%
Vapor inlet pressure [kPa]	102 – 106	±0.1
Vapor inlet superheat [°C]	0.1 – 0.7	±.05
Inclination angle [°]	0.3 – 13.2	±0.4%

3.2 Measurements

Heat balance was determined on the steam side and on the air side to provide redundant measurements. On the air side, the measurements were divided into eleven 1-m sections along the tube. Air velocity was measured with an Alnor Compuflow 8585 hot wire anemometer, calibrated

using a procedure detailed in Appendix B. Local air velocity varied extensively, due to slight geometric differences in the fins and due to the inherent non-uniformity in air flow from an axial-flow fan. As a result, an average air velocity per section was determined by measuring at 5 cm increments along the length of the condenser, and at three points along the fin height. Average velocity per section varied $\pm 10\%$ around the overall average velocity.

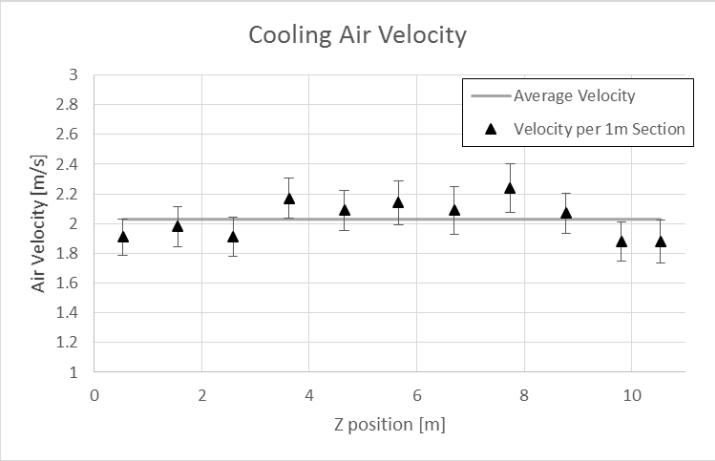

Figure 8: Average air velocity per 1m section along the condenser, measured at the inlet to the fins

Temperatures were measured at 1-m intervals along the condenser, as diagramed in Figure 10. At each point, steam saturation temperature, condenser wall temperature, air temperature across the fins, and local air temperature were measured. Saturation temperature of the steam and condenser wall temperature were measured at x-locations 160.5 and 53.5 mm, in order to detect temperature gradients along the tube height. T_{amb}, T_{satt}, T_{satb}, T_s, T_{ai} and T_{ao} were measured using sheathed T-type thermocouples. T_{wt}, T_{wb}, T_{at}, and T_{ab} were measured using welded-bead 30-gauge T-type thermocouple wire. Saturation temperatures were measured at the halfway point of the duct cross section, equidistant from the duct wall and the polycarbonate window. Wall temperatures were measured by embedding the thermocouple beads in the wall, entering from the air side. Local air temperatures, T_{at} and T_{ab}, were measured by attaching the thermocouple beads to the fins with

aluminum tape, as seen in Figure 9. All thermocouples were calibrated before installation in the facility in a Neslab thermal bath with temperature control with an ISOTECH TTI-22 standard RTD thermometer as a reference.

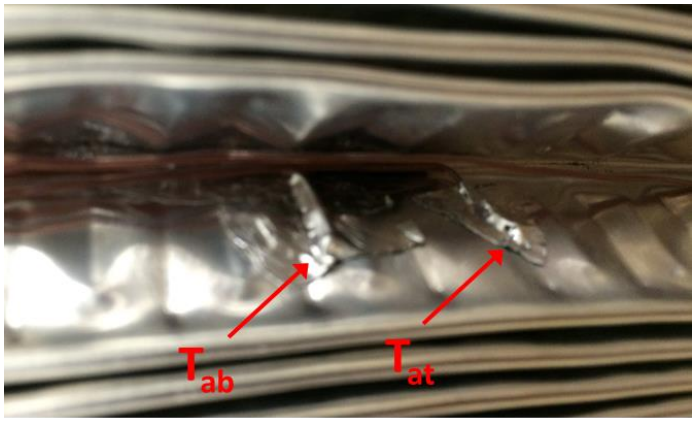

Figure 9: Configuration of T_{ab} and T_{at} thermocouples. Fins were returned to proper angle after installation

All pressure measurements were recorded using Rosemount 1151 differential pressure transmitters. The pressure transmitters were calibrated versus a manometer after being installed in the system. Gauge pressure was measured at the tube inlet and outlet, and steam-side differential pressure along the condenser was measured at 2.14 m intervals along the tube. Atmospheric pressure was recorded from the local weather station.

Condensate mass flow rate was measured at the receiver by weight, using a Global Industrial digital scale. The scale was calibrated using a graduated cylinder filled to various heights with water.

Time was recorded by an HP 3852A data logger.

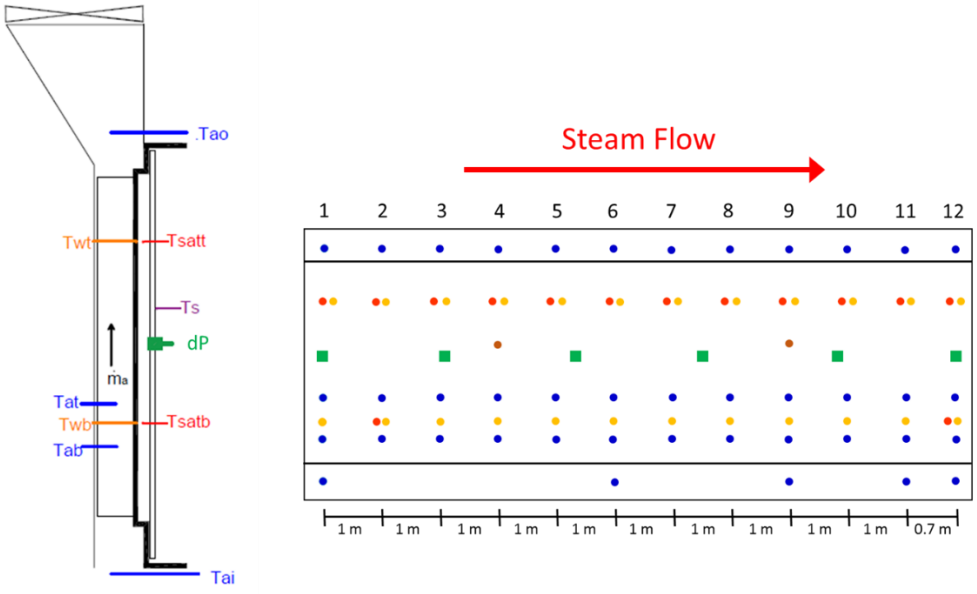

Figure 10: Schematic drawing of temperature and pressure measurements

Height of the condensate river along the polycarbonate viewing window was measured using a ruler. Diffuse light was shined on the condensate river, and the reflection from the river surface made the height clearly visible. This height was then converted to height along the steel surface using a procedure outlined in Appendix A.

3.3 Visualization Facility

Visualization was performed along the entire length of the condenser tube. During data acquisition, the polycarbonate window was covered with opaque polystyrene foam insulation. When the insulation was removed for visualization, condensate would form on the window, obscuring the view and slightly altering the internal regime. In order to prevent this, the viewing window was kept at 100° C by via a 300W lamp. Further details of this process are available in Appendix G.6.

High-speed video recordings of the condensate flow were acquired at 1,000 frames per second and a resolution of 512 x 512 pixels. Phantom Cine software from Vision Research was used to process the video.

Normal-speed video recordings, as well as still photos were taken with an iPhone 4s and iPhone 5s from Apple. Windows Movie Maker, VideoLAN VLC Player and Lenovo Photo Editor were used to process and edit the video and photos.

Chapter 4: Visualization

Before analyzing the condensation pattern, it is important to consider any possible differences that may arise for the experimental half tube versus the full tube in an operating ACC. The steel surface is initially identical between the two systems. However, due to constant operation with non-condensables removed, an operating ACC may experience less rusting than the experimental system. However, that difference is unknown. Therefore, the condensation regime is assumed to be the same in the experimental system as in an operating system. In addition, the inlet vapor velocity is similar for both systems, so no differences in flow pattern were expected for a half tube versus a full tube. Finally, although the cross-sectional area for condensate flow at the tube bottom was halved, the volume of condensate generated was also decreased by half versus the full tube. As a result, the proportion of heat transfer surface area covered by condensate was assumed to be the same for the experimental half tube versus the full tube in an operating ACC.

4.1 Flow Pattern

As diagramed in Figure 2 above, the general pattern of flow was axial vapor flow, with mixed filmwise and dropwise condensation on the tube wall. In the dropwise regions, droplets of critical size would fall due to gravity, sliding along the steel surface and cleaning the surface below of droplets. These falling droplets would almost exclusively originate at the top of the tube, because droplets lower on the surface would be continuously swept off by droplets falling from above. These falling droplets would eventually join the condensate river at the tube bottom. The

condensate river also flowed in the axial direction, predominantly due to gravitational force. The condensate river gradually increased in depth and velocity from tube inlet to tube outlet.

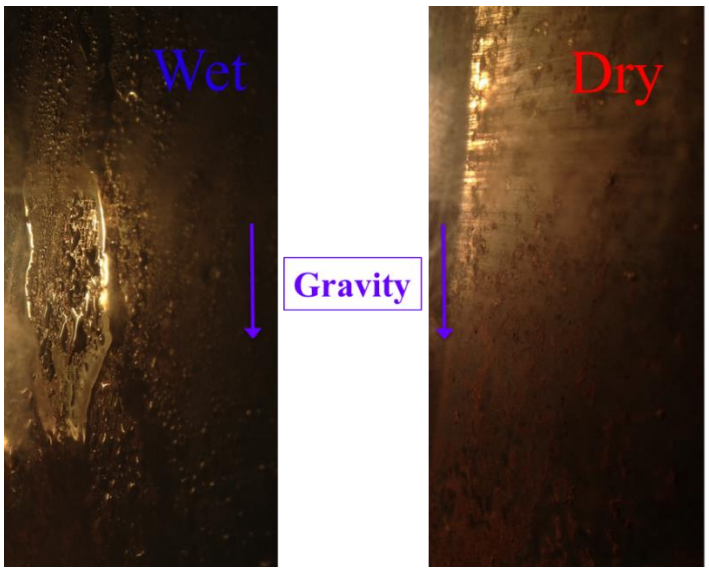

Figure 11: Mixed-mode condensation at z = 10m; left shows dropwise condensation and rivulets, right shows condenser surface before steam is run in order to clarify the 'wet' image

From this basic description, the flow pattern could then be divided into four different flow regions along the length of the condenser: the entrance region, wavy region, transition region and stagnation region.

4.1.1 Entrance Region

This region began at the condenser inlet and extended less than 0.5 m into the tube. However, the exact length where the entrance region ended and the wavy region began was difficult to define. In this region there was developing turbulent vapor flow and both filmwise and dropwise condensation on the tube wall. Falling droplets of condensate were subjected to significant shear stress, so they were carried downstream while falling under the influence of gravity. As a result, there was no significant condensate river in this region.

4.1.2 Wavy Region

This region had developed vapor flow and filmwise and dropwise condensation on the wall. In this region, the condensate river had reached a depth of a few millimeters. However, due to the high vapor velocity, the condensate river had a distinct wave pattern caused by a Helmholtz instability. These waves served to stimulate heat transfer by inducing turbulence in the liquid and vapor. This region was very short, with a length of less than 1 m. It was only present in the horizontal orientation.

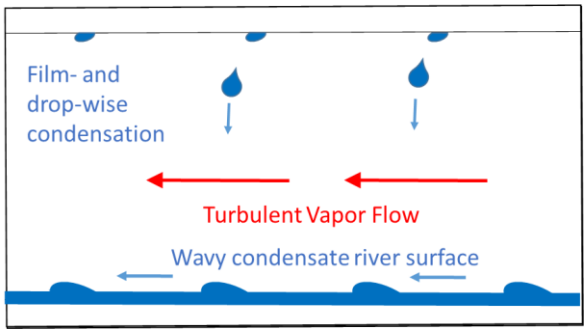

Figure 12: Schematic diagram of wavy condensate region

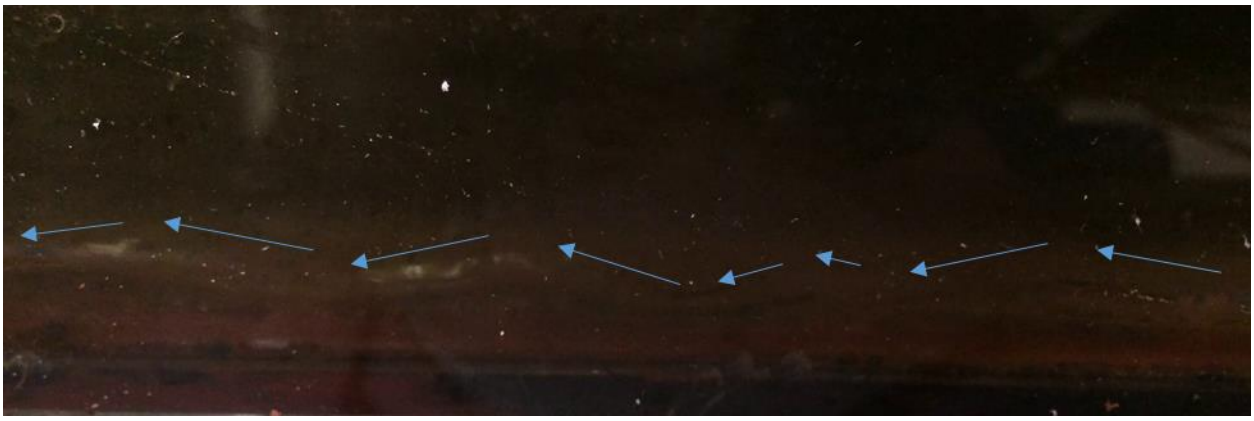

Figure 13: Waves in the condensate river caused by high-velocity vapor shear

4.1.3 Transition Region

The transition region was characterized by a smoother vapor-condensate interface at the tube bottom. The condensate river had increased in depth, and the vapor velocity had decreased. In this region, the vapor flow transitioned from turbulent to laminar. As a result, the flow of condensate was almost entirely gravity driven. The falling condensate droplets fell parallel to the force of gravity, and the condensate river slowly accelerated with gravity. This region encompassed the majority of the condenser's length.

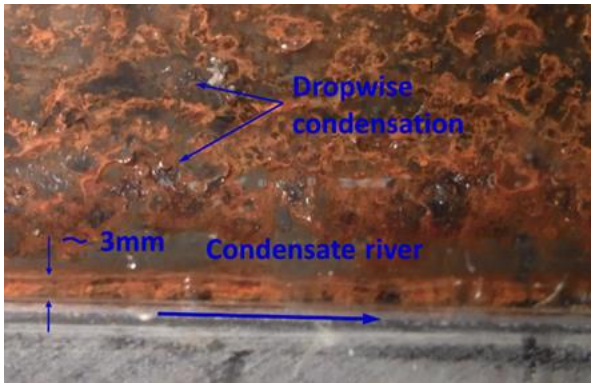

Figure 14: Condensate river in transition section

4.1.4 Stagnation Region

The stagnation region occurred only near the tube outlet. In this region, vapor velocity fell to zero, and the condensate flow was completely dominated by gravity. Velocity and mass flow rate of the condensate river was at a maximum in this region. For the horizontal configuration, depth of the condensate river decreased in this section. For all other inclinations, the condensate river

increased to a maximum at the condenser outlet. The low vapor velocity and thicker layer of condensate at the tube bottom should lead to a decrease in heat transfer coefficient of steam.

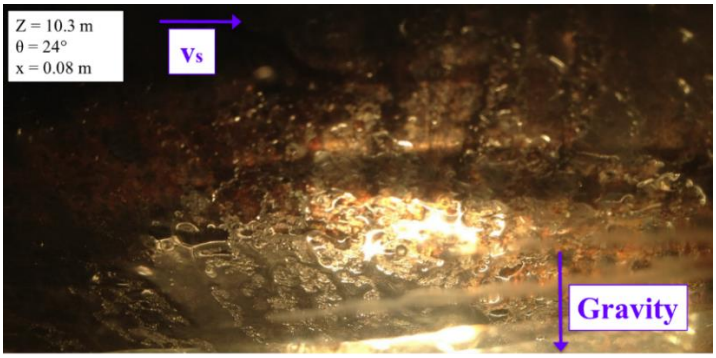

Figure 15: Mixed-mode condensation near tube outlet

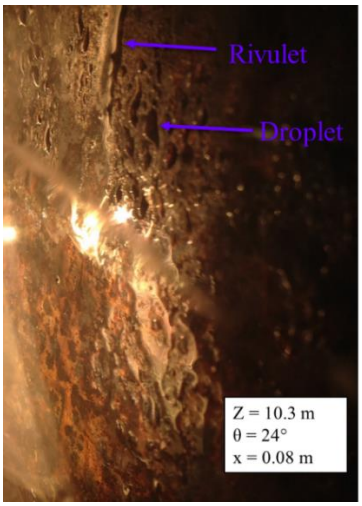

Figure 16: Mixed-mode condensation near tube outlet

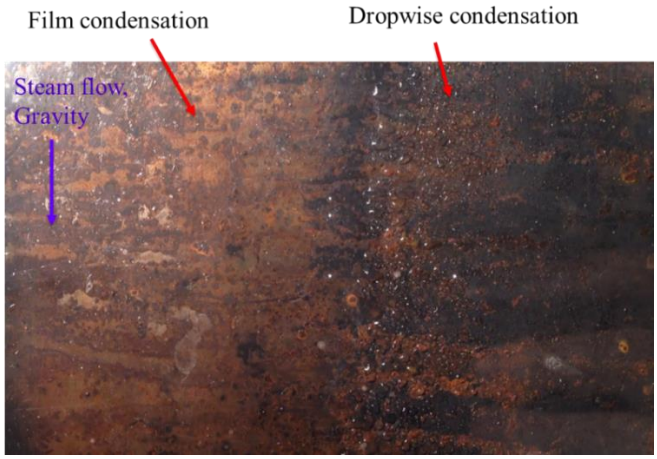

Figure 17: Film condensation alongside dropwise condensation in vertical downward flow

4.2 Effect of Inclination

For each tube inclination, some changes in each of the four regions above could be observed. In addition, the depth of the condensate river varied greatly with inclination.

The wavy region, as defined above, was only present when the condenser was near horizontal. For any other inclination, the condensate river was very thin near the tube entrance. As a result, the shear forces of the vapor acting on the liquid were not able to overcome the viscous forces in the condensate river. For these inclinations, the regime transitioned directly from the entrance region into the transition region.

The depth of the condensate river was also measured at five points along the condenser. Figure 18 and Figure 19 show that for all inclinations above horizontal, the depth of the condensate river gradually increased along the condenser length. This result agrees with that predicted by Cheng at al. [17]. However, the depth of the condensate river found experimentally was much greater than the depth in Cheng's model. For example, the maximum film thickness at 5° inclination in

the model was 2.1 mm, versus 8.3 mm for 6° in the experiment. However, the depths cannot be compared directly, due to the differing geometries. The model is a full tube and assumes a semi-circular tube bottom, while the experimental half tube bottom is a circular sector. Therefore, an equivalent volumetric flow rate of condensate passing at equivalent velocities will have differing heights between the full-tube model and half-tube experiment. Comparing cross-sectional area of the condensate flow at each location can clarify this discrepancy.

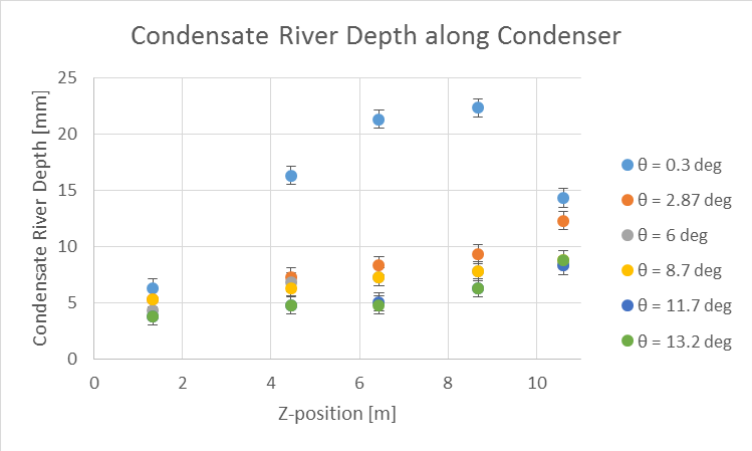

Figure 18: Depth of condensate river at discrete locations along condenser, at six different inclination angles

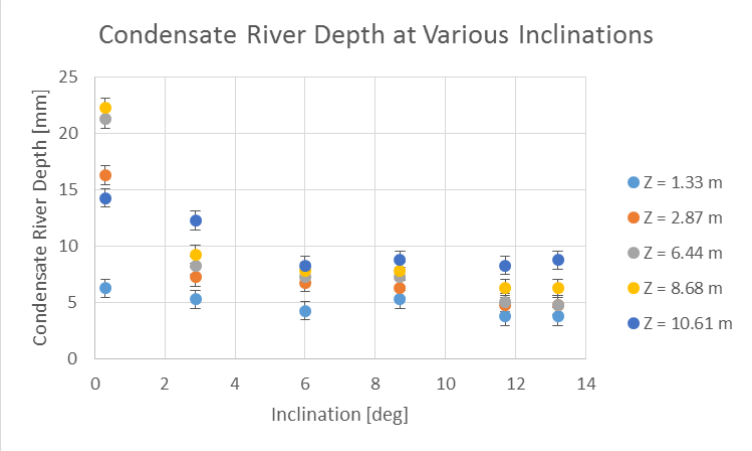

Figure 19: Condensate river depth at different inclination angles, at five discrete points along the condenser

To compare cross-sectional areas, the numerical model at 5° inclination and the experimental result at 6° inclination were compared. A depth of 2.1 mm in the bottom of Cheng's tube for a 5°

inclination equated to a cross-sectional area of 55.8 mm^2. A depth of 8.3 mm in the bottom of the half-tube at 6° inclination equated to a cross-sectional area of 24.5 mm^2, which is 12% lower than the area predicted by the numerical model. This difference is surprising, considering that Cheng's model assumed a lower 15.8 g/s steam flow rate for a full tube, while this experiment had a 10 g/s flow rate for a half tube.

Table 2: Cross-sectional area of condensate river for numerical full-tube and experimental half-tube

	Full-Tube Numerical Model [17]	**Half-Tube Experimental Result**
Inclination [deg]	5	6
Condensate Area [mm^2]	55.8	24.5

4.2.1 Effect on Heat Transfer

The condensate river affects the heat transfer by decreasing the available condensation area. Heat transfer by single-phase laminar convection of liquid is less than 10% of that of condensing vapor. Therefore, overall heat transfer coefficient can be assumed to be reduced by an amount proportional to the condenser area covered by the condensate river.

At a given axial location, the steel portion of the half tube had a perimeter of 222 mm. At an inclination of 6° and position of 1.3 m, the condensate height on the condenser surface was 4.3 mm. At 10.6 m the height was 8.3 mm. This corresponded to heights of 4.3 mm and 8.3 mm on the steel at each location, respectively. This equated to a 1.8% loss in heat transfer area between 1.3 m and 10.6 m along the condenser.

Chapter 5: Heat Transfer

5.1 Data Reduction

Air-side heat balance was determined per measurement section, *j*, as:

$$Q_{a,j} = v_{a,j}\rho_{a,j}H_a\Delta z\left(c_{p,a,out,j}T_{ao,j} - c_{p,a,in,j}T_{ai,j}\right) + Q_{a,loss,j}$$

$$Q_{a,loss,j} = UA_{a,loss}LMTD_{a,j}$$

$$Q_a = \sum_{j=1}^{11} Q_{a,j}$$

Steam-side heat balance was determined for the entire condenser based on inlet and outlet conditions, instead of by section.

$$Q_s = \dot{m}_c(i_i - i_o) - Q_{s,loss}$$

Steam entered the condenser slightly superheated, so it could be assumed that all condensate exiting the condenser had condensed inside. Also assuming negligible superheat and subcooling, Q_s was simplified to:

$$Q_s = \dot{m}_c\left(i_{fg}\right) - Q_{s,loss}$$

$$Q_{s,loss} = UA_{s,loss}LMTD_s$$

Overall heat transfer coefficient, U, was determined using the uncertainty-weighted average of the steam-side and air-side heat transfers, and a heat-transfer resistance network:

$$\bar{Q} = \frac{\left(\frac{1}{{u_a}^2}\right) Q_a + \left(\frac{1}{{u_s}^2}\right) Q_s}{\frac{1}{{u_a}^2} + \frac{1}{{u_s}^2}}$$

$$\bar{Q} = UA \times LMTD$$

$$LMTD = \frac{(T_{satt} - T_{ai}) - (T_{satt} - T_{ao})}{\ln\left(\frac{T_{satt} - T_{ai}}{T_{satt} - T_{ao}}\right)}$$

$$\frac{1}{UA} = \frac{1}{\bar{h}_a A_a} + \frac{t_{st}}{k_{st} A_s} + \frac{1}{\bar{h}_s A_s}$$

As overall resistance could be divided into air-side, nearly-negligible conduction through the steel, and steam-side, as shown in the equation above, steam-side heat transfer coefficient could be determined with all other variables known.

The correlation for air-side heat transfer coefficient for this particular geometry was provided from experimental work performed by Creative Thermal Solutions:

$$Nu = 0.1871 {Re_a}^{0.5}$$

In addition to an overall steam-side HTC, steam-side HTC was determined locally by using the temperature difference between the wall and the saturated steam. These measurements are shown in Figure 20.

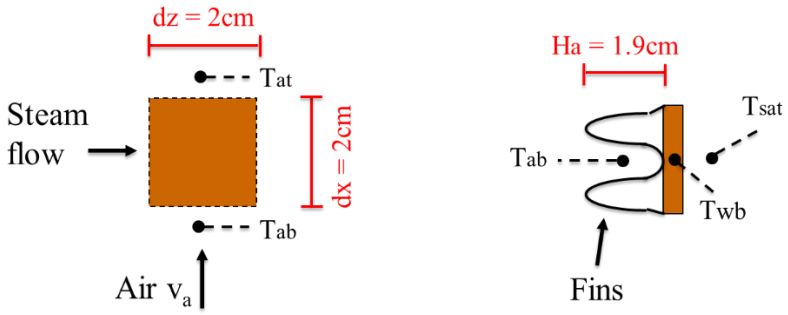

Figure 20: Schematic diagram of local heat transfer coefficient measurements a) condenser face; b) condenser cross-section

$$q'_{a,local} = \rho_a v_a H_a \left(c_{p,a,top} T_{at} - c_{p,a,bot} T_{ab}\right)$$

$$q'_{s,local} = h_{s,local} dx (T_{sat} - T_{wb})$$

$$q'_{a,local} = q'_{s,local}$$

All of the results for HTC in the half tube are assumed to be equivalent to those in a full tube, due to symmetry. The exchange of half of the condenser tube for a polycarbonate viewing window was not expected to affect the heat transfer of steam to the cooling air. The polycarbonate viewing window was insulated, and therefore adiabatic. The full tube was also adiabatic at the center, due to symmetry. In addition, the HTC was expected to be largely dependent on local void fraction, and not Reynolds number of the vapor flow. Therefore, any additional shear imposed on the vapor flow by the stationary polycarbonate window was not expected to have a significant effect on the HTC results.

5.2 Heat Transfer Results and Discussion

Based on previously published results, steam-side heat transfer coefficient was expected to be a function of inclination angle, φ. The maximum overall heat transfer coefficient was expected to

occur between an inclination angle of 15 and 45°. Overall steam-side heat transfer coefficient showed an increase of up to 30% versus the horizontal for inclinations of 6° and higher. However, the large amount of scatter in the data and the significant uncertainty made the correlation between inclination angle and steam-side HTC weak. A linear regression of HTC over inclination angle indicated that 24% of the variation in HTC was due to inclination angle. The correlation between HTC and inclination angle was 0.49, and the slope was 0.013, with a standard error of 0.006. This indicates with 98% confidence that the slope was above 0.001. These data indicate that heat transfer coefficient was a function of inclination angle as expected. However, a reduction in the uncertainty, an improvement in the repeatability, and an increase in the inclination angle will be necessary to make a stronger conclusion about the relationship between inclination and steam-side heat transfer coefficient.

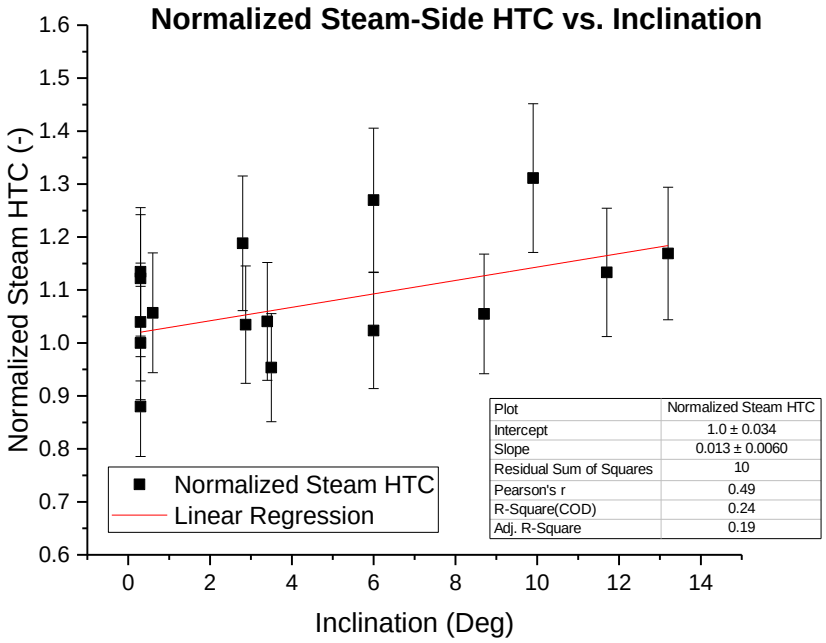

Figure 21: Steam-side heat transfer coefficient normalized to HTC in the horizontal inclination

When comparing the relative heat transfer coefficient among different inclinations, the uncertainty was 10% per point. This was lower than for the absolute heat transfer coefficient data, because some systematic error could be removed when comparing relative values. For the absolute HTC, uncertainty increased to approximately 17% per point. However, compared to the HTC predicted by Nusselt condensation [3] and Kroger's correlation [21], the measured HTC was less than one-third of the anticipated values.

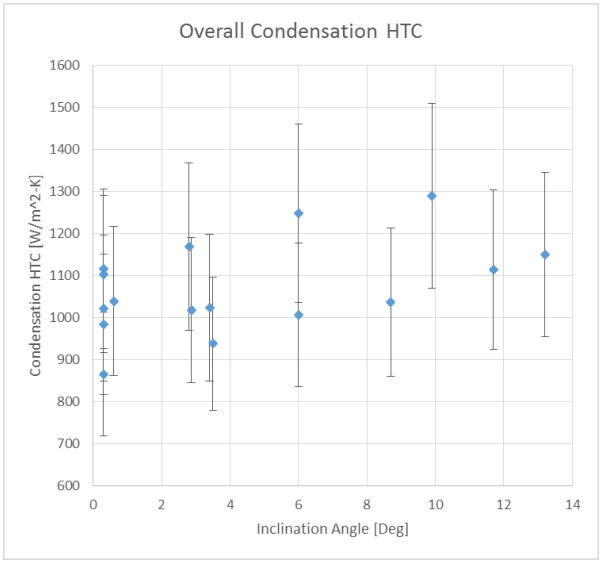

Figure 22: Steam-side heat transfer coefficient vs. inclination angle

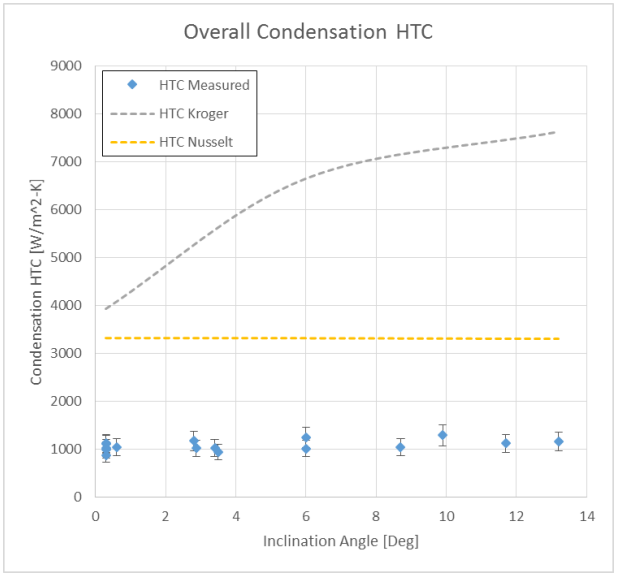

Figure 23: Measured steam-side heat transfer coefficient compared to predictions from Nusselt [3] and Kroger [22]

Figure 24-Figure 27 show air-side heat flux at each measurement section along the condenser, for five different inclinations from 0.3 – 13.2º. Heat flux for each section is normalized to the horizontal inclination. The data show that inclination angle had the most significant effect on heat flux in the entrance region of the condenser. Inclinations of 2.87º and 6º showed a decrease in heat flux over the first three meters of the condenser. Heat flux over the first meter of the tube then slowly increased for angles 8.7-13.2º, reaching a maximum improvement of 5% versus the horizontal for the maximum inclination of 13.2º. The increase in heat flux over the second and

third meters was not significant. The change in heat flux versus inclination was not significant for other portions of the tube, except for the 6° inclination. For this inclination, the heat flux decreased versus the horizontal for the first nine meters of the condenser tube. The portion of the tube that showed the least effects of inclination was the final two meters.

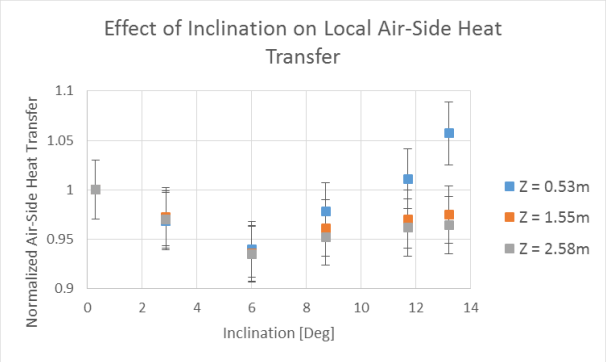

Figure 24: Air-side heat flux over 0-3m axial position along the condenser, normalized to the horizontal inclination

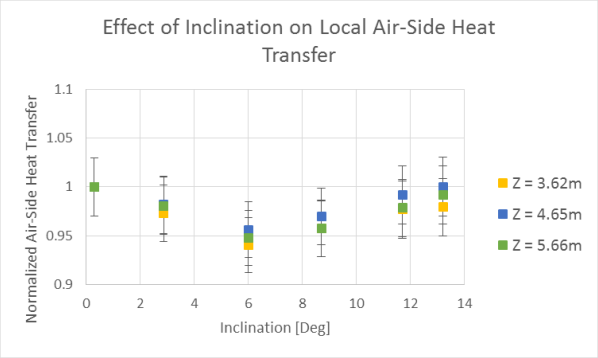

Figure 25: Air-side heat flux over 3-6m axial position along the condenser, normalized to the horizontal inclination

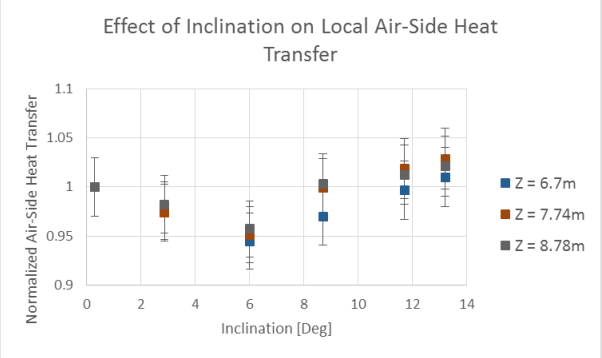

Figure 26: Air-side heat flux over 6-9m axial position along the condenser, normalized to the horizontal inclination

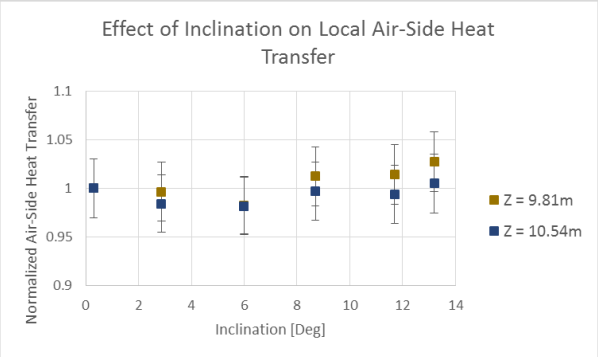

Figure 27: Air-side heat flux over 9-10.7m axial position along the condenser, normalized to the horizontal inclination

These results are surprising in that the inclination effect has been previously shown to be more pronounced for low quality and low vapor mass flux. These two variables are lowest near the condenser outlet. However, previous studies did not investigate vapor mass fluxes near stagnation, and in fact, the entrance vapor mass flux of 6.5 kg/m^2-s was below the range of operating conditions studied by Wang and Du [16].

As seen in Figure 28-Figure 33, heat flux along the condenser for a given inclination varied over 40% from the lowest to the highest heat-flux section. However, most of that variation in heat flux was caused by variations in air velocity. Although the data seemed to indicate a lower heat flux in the first 1 m and last 2 m of the condenser, a strong conclusion could not be made from these figures alone.

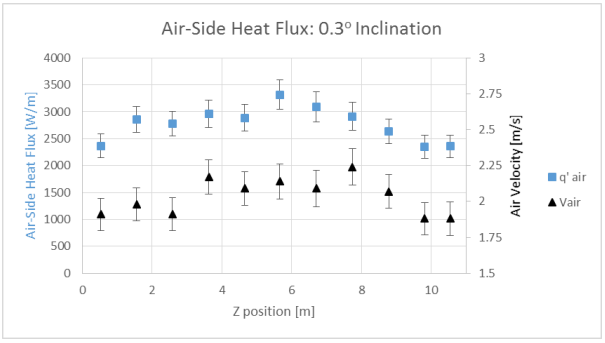

Figure 28: q'_a and v_a along the condenser for 0.3° inclination

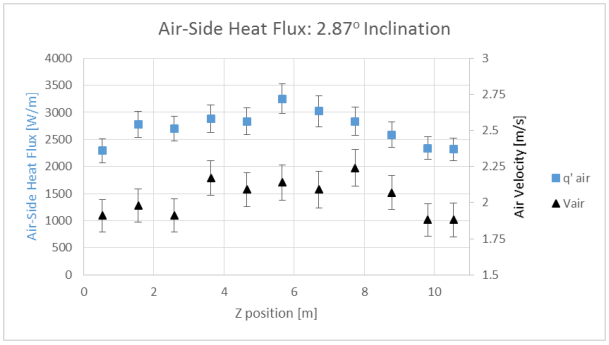

Figure 29: q'_a and v_a along the condenser for 2.87° inclination

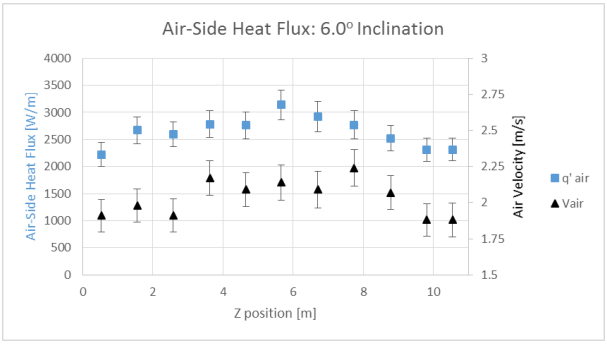

Figure 30: q'_a and v_a along the condenser for 6.0° inclination

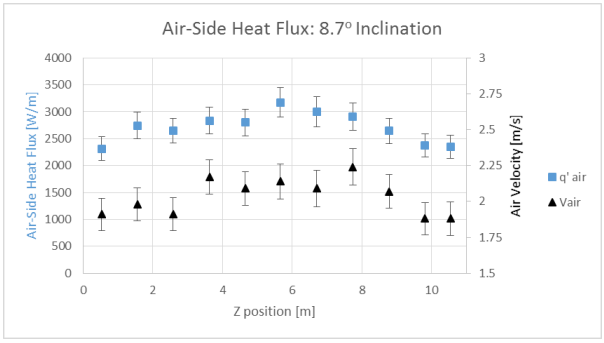

Figure 31: q'_a and v_a along the condenser for 8.7° inclination

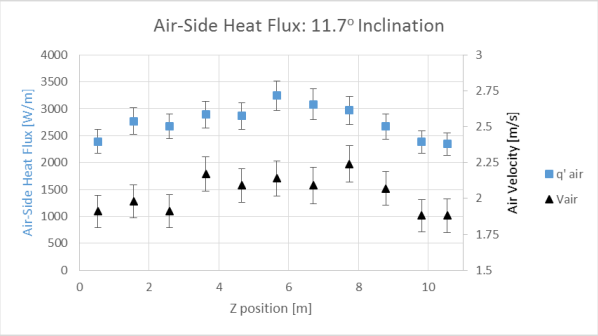

Figure 32: q'_a and v_a along the condenser for 11.7° inclination

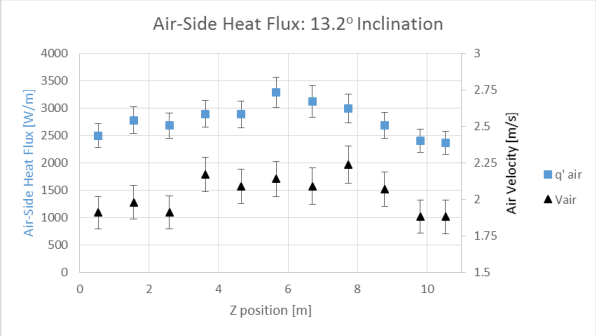

Figure 33: q'_a and v_a along the condenser for 13.2° inclination

As shown in Figure 34 below, air-side heat flux and air velocity had a correlation of 0.84, and a slope of 1.5. 71% of the changes in heat flux could be attributed to changes in velocity. The strength of the relationship between velocity and heat flux makes it imperative that air velocity be uniform in order to understand the relationship between heat flux and inclination and position along the condenser.

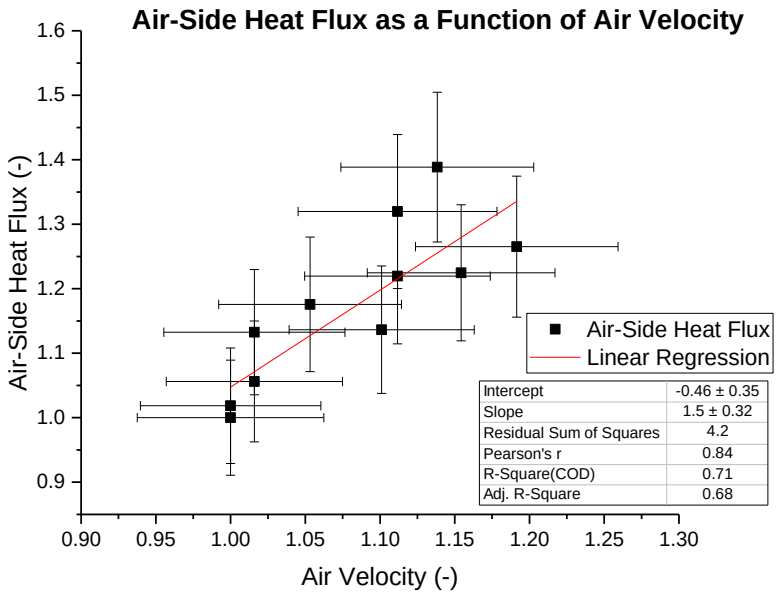

Figure 34: Normalized air-side heat flux vs air velocity

With the effects of changes in velocity removed, the inlet section still displayed the lowest heat flux for all inclinations. This was surprising because this section had the highest vapor velocity and the lowest amount of condenser area covered by condensate. More investigation is necessary to identify if the lower heat flux is due to a physical phenomenon inside the condenser. Additionally, the relatively higher heat flux over the final condenser section was also unexpected. In direct contrast to the entrance region, the exit region is characterized by a thicker condensate river and stagnation of the vapor, both of which lead to lower steam-side heat transfer coefficient.

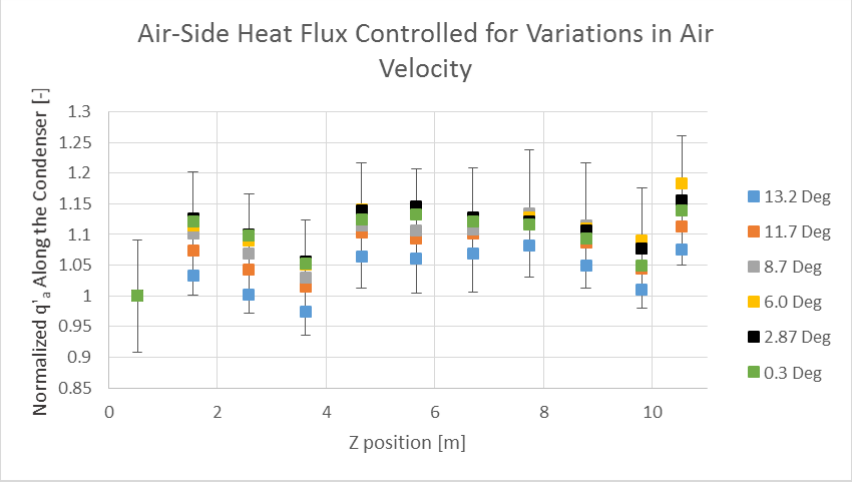

Figure 35: Normalized heat flux along the condenser controlled for variations in air velocities

To better understand the effect of changing inclination on the heat flux, Figure 36 shows heat flux along the condenser normalized to heat flux at the inlet of the horizontal inclination. The chart shows that heat flux varies around 10% with small changes in inclination. The chart also displays

that the 6° inclination had the lowest heat flux for all sections, while the highest inclinations had slightly higher heat flux at the inlet region, as well as from 7-9 m along the condenser.

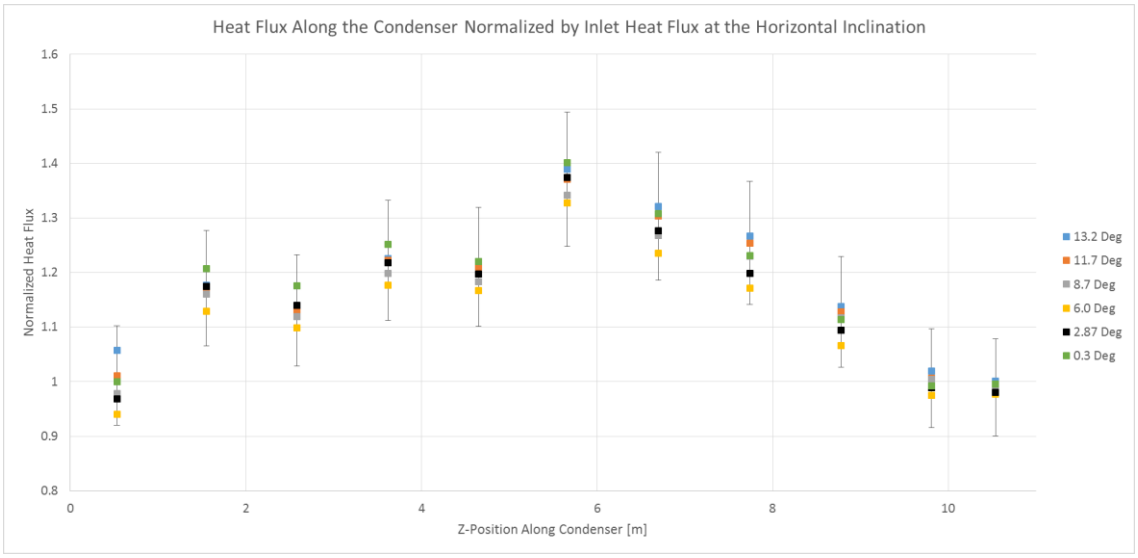

Figure 36: Heat flux along the condenser normalized to inlet heat flux at the horizontal inclination

Local steam-side heat transfer coefficient, $h_{s,local}$, was not accurate enough to provide significant information. The local HTC was measured independently from air-side heat flux, so it could be potentially used to corroborate changes in heat flux along the condenser. As seen in Figure 37, the data appeared to indicate a higher heat transfer coefficient over 4-7m along the condenser, along with a slight increase in HTC at the condenser end. This agreed with the higher heat fluxes measured over these sections. However, the uncertainty of the $h_{s,local}$ values ranged from 33% – 216%. Therefore, no certain conclusions could be made.

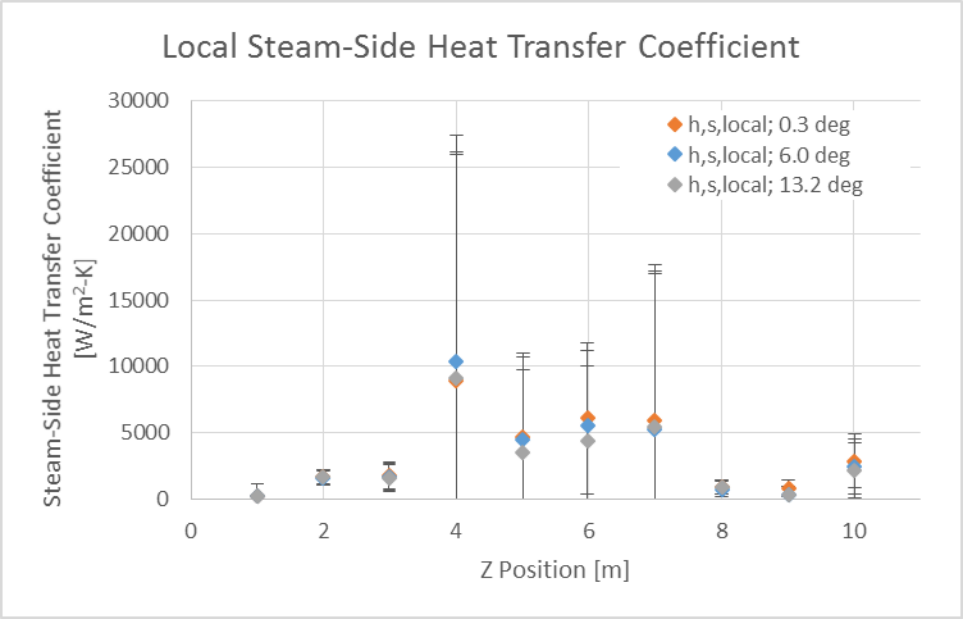

Figure 37: Local steam-side heat transfer coefficient, from wall temperature

Chapter 6: Conclusion

6.1 Summary

Visually, the steam condensation and heat transfer occurred as expected, with mixed-mode dropwise and filmwise condensation, and a condensate river at tube bottom that increased in depth while progressing down the length of the condenser. The condensation mode and flow regime did not change with an increase in inclination from horizontal to 13.2^{o}. However, the depth of the condensate river decreased at all positions along the condenser with an increase in inclination.

The average steam-side heat transfer coefficient increased with an increase in inclination. A 1-degree increase in inclination increased the heat transfer coefficient by approximately 1%. However, this relationship was obscured by high uncertainty in the data. A strong relationship between air velocity and heat flux also obscured the effect of axial position on heat flux. The data did, however, indicate a lower heat transfer coefficient and heat flux at the condenser inlet.

The magnitude of average heat transfer coefficient was lower than that predicted by either classical Nusselt condensation [3], or by Kroger's [21] correlation for air-cooled condensers. Local heat transfer coefficient measured from wall temperatures were higher than the average steam-side coefficient measured. However, the extremely high uncertainty in these measurements made it difficult to draw conclusions from the data.

6.2 Future Work

The promising early results of this work combined with the high uncertainty in many of the measurements lead to multiple possibilities for future work. Future work will be focused on several aspects:

1) Achieve a more accurate steam-side HTC – Although the relative values of HTC are valuable in determining the optimal inclination angle for heat transfer, more accurate results for the magnitude of HTC are necessary to validate and/or improve on current correlations for inclined, flattened-tube condensation heat transfer.
2) Test condenser at higher inclinations, up to vertical – This is the simplest and most obvious of the directions for future work. The current data show a dependence on inclination angle for heat transfer for the low inclination angles tested. The data set needs to be completed to verify this dependence over all inclinations and to find the optimal inclination for steam-side heat transfer.
3) Measure different air-velocity profiles – The current tests were performed with a semi-uniform air velocity. A set of tests needs to be completed with perfectly-uniform air velocity in order to perform a proper characterization of the steam-side condenser performance. Once this basic characterization is complete, performance under various operational air velocity patterns can be tested to gauge performance of the optimal inclination under normal operating conditions.
4) Mechanistic model of condensation – Finally, creating and validating a mechanistic model of condensation in the inclined, flattened-tube condenser will aid in understanding the relevant physical phenomena, as well as aid in improving the engineering design of air-

cooled condensers. A mechanistic model will allow for accurate modeling and parametric testing of various improved condenser designs. In order to achieve this, droplet size, film thickness, condensate river velocity, stability of condensate river surface, void fraction, and local vapor flow rate will all need to be modeled and validated by experimental measurements.

Appendix A: Calculation of Condensate River Cross-Sectional Area

The depth of the condensate river reported by Cheng et al. [17] is defined differently than the depth reported in this study. Cheng uses the maximum thickness of the condensate river at the tube bottom, while this study uses the height of the condensate river along the viewing window. Cheng's model assumes uniform film condensation along the tube wall, and a smooth transition between falling condensate film and the condensate river at the tube bottom. In the experiment, a discrete condensate river was observed, separate from the condensing and falling film and the droplets on the condenser wall. As a result, the condensate river depth was easily defined in the experiment but not in the model.

To compare the results, the cross-sectional area of the condensate film inside the bottom semi-circular region of the tube is calculated and compared to the cross-sectional area of the condensate river found in the experiment. Cheng's model uses the geometry shown in Figure 38, with a semi-circle with a diameter of 9.5mm. Cheng found that the liquid film thickness did not vary significantly over the tube bottom, so it was assumed to be constant for the purposes of the area calculation.

$$A_{Cheng} = \frac{\pi D^2}{4} - \frac{\pi (D - t_c)^2}{4}$$

$$t_c = thickness\ of\ condensate\ film$$

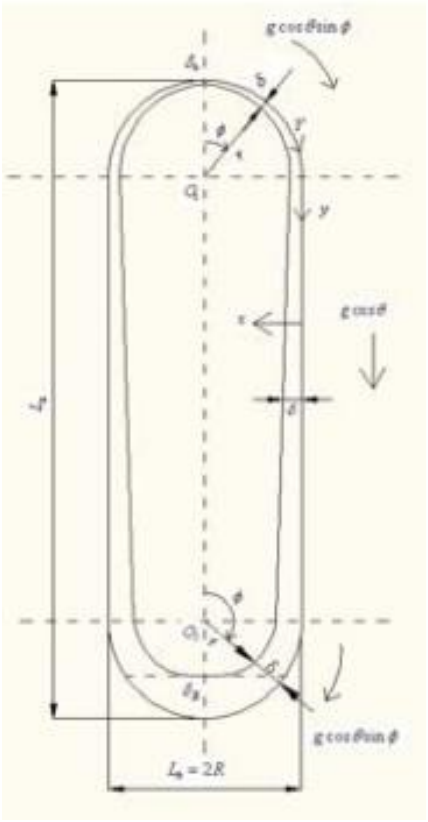

Figure 38: Physical model of the flattened tube of Cheng et al. [17]

For the experimental cross-sectional area, the geometry of the tube bottom was found by tracing a photograph of the half-tube in Solidworks. Then, the height of the condensate on the polycarbonate window and the steel tube were measured and determined, respectively. A smooth curve was then drawn in Solidworks to approximate the condensate surface, and the area was calculated by Solidworks.

The height of the condensate river on the steel was determined by first assuming a triangular shape of the condensate along both walls. This can be seen in Figure 40. The capillary rise on both walls was then calculated by equating the forces of the water surface's line tension and buoyancy of liquid water in water vapor. The difference between the capillary rise on the steel and polycarbonate was then added to the measured condensate river height on the polycarbonate.

$$\sigma \cos \theta_{st} = g(\rho_l - \rho_v) \frac{\delta_{st}^2 \tan \theta_{st}}{2}$$

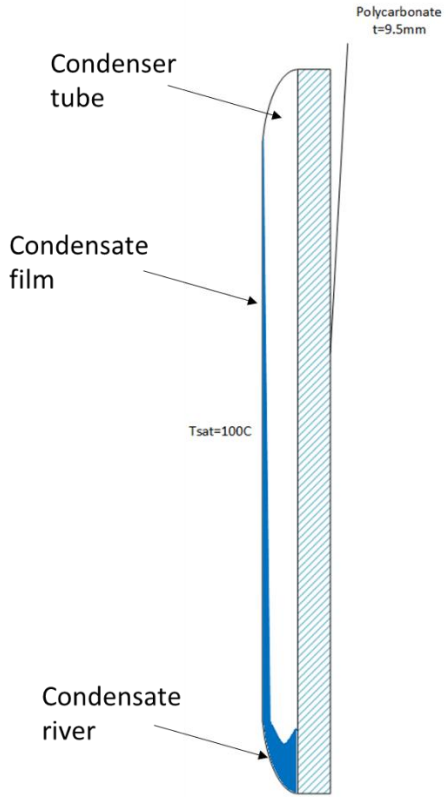

Figure 39: Schematic diagram of condensate in half-tube

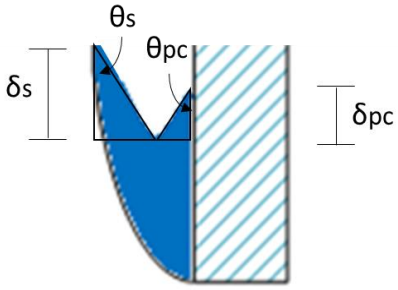

Figure 40: Assumptions of condensate river consisting of two right triangles above the main flow

The contact angle was taken as the static contact angle of water on each surface. The contact angle of water on the rusted condenser surface was measured using a goniometer. The contact angle of water on polycarbonate was taken from experimental work by Diversified Enterprises [29]. Due to the lesser contact angle of water on steel, the capillary rise of water on the steel surface is approximately five times greater than the rise on the polycarbonate.

Table 3: Contact angle and capillary rise of the condensate river on steel and polycarbonate

	Steel	Polycarbonate
θ [deg]	52	82
δ [mm]	2.5	0.5

The condensate river was then drawn in the Solidworks model of the duct, and the area was determined. The resulting experimental area came to 44% of the numerical model of Cheng [17], meaning that the model over-predicted the amount of condensate by 12% for this particular point.

Table 4: Cross-sectional area of condensate river in numerical model and experimental results

	Full-Tube Numerical Model [17]	**Half-Tube Experimental Result**
Inclination [deg]	5	6
Condensate Area [mm^2]	55.8	24.5

Appendix B: Air Velocity Measurement

The air velocity measurement was performed by using a hot-wire anemometer placed at the bottom of the fin arrays. Due to extensive local variation in the air flow, an average air flow along each 1 m section of condenser was measured and computed. Air velocity was measured in 5 cm increments along the length of the condenser, and at the fin base, middle, and top at each measure point, as shown in Figure 41.

The entrance to the air duct was not uniform, but had structural bolts and nuts located at 5cm intervals partially obstructing the duct entrance. This can be seen in Figure 42. These bolts covered approximately 1/11 of the duct entrance area. Therefore, 1/11 of the velocity measurements were taken behind these bolts in order to have an accurate sample of the entire population of velocity measurements.

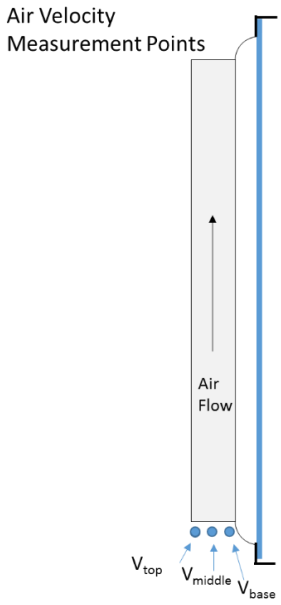

Figure 41: Air velocity measurement points



Figure 42: Anemometer in position to measure air velocity at middle of fins. Note screws covering 1/11 of duct face area.

Individual fans were controlled with 1kohm potentiometers. The initial velocity measurement was performed with each fan drawing the same power. Once all of the velocity measurements were complete, the sections with the lowest velocity were increased in power, and the highest-velocity sections were decreased in power. After a few iterations, the final average velocity per section ranged from 1.88 m/s to 2.24 m/s. The maximum velocities were at the middle of the condenser, and the minimum velocities were located at the inlet and outlet. The average velocity was 2.03 m/s, as seen in Figure 43.

Along the fin height, a slightly higher velocity was measured at the middle of the fin than at the fin base or top, as seen in Table 5.

Table 5: Velocity profile along fin height

V_{top}	V_{middle}	V_{bottom}
m/s	m/s	m/s
2.00	2.12	1.97

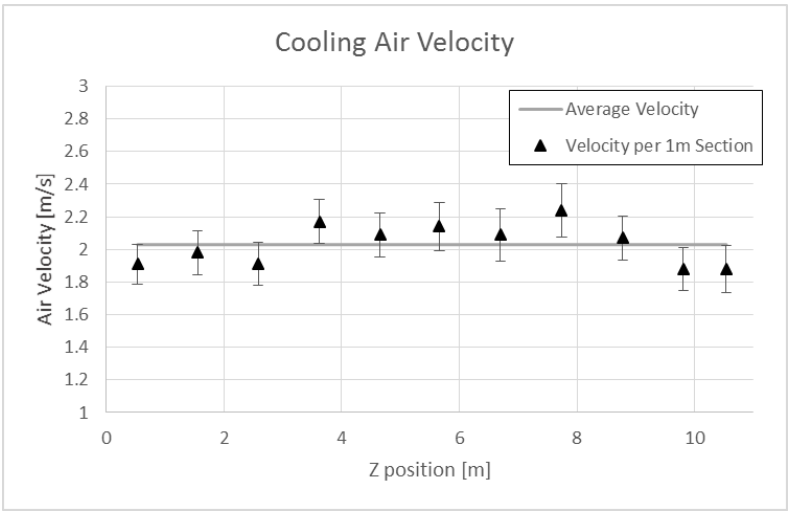

Figure 43: Air velocity per section, and average air velocity for the entire condenser

To verify accuracy, the anemometer was calibrated before use. The anemometer calibration was performed in a wind tunnel against the differential pressure across a nozzle, according to ASHRAE standard 41.2-1987. The calibration was performed at 14 points (one repeated to verify repeatability) from 0.18 – 4.2 m/s. Calibration results and facility schematic are below.

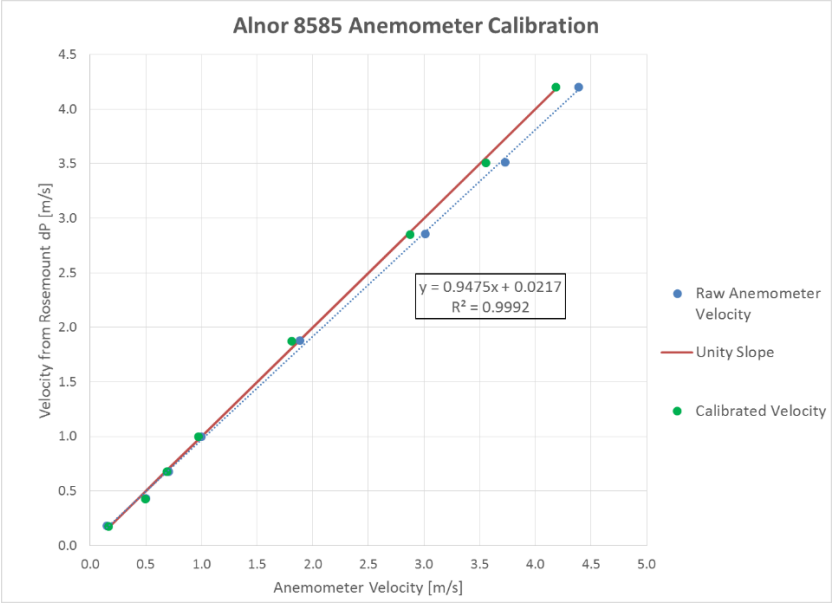

Figure 44: TSI Anemometer calibration results

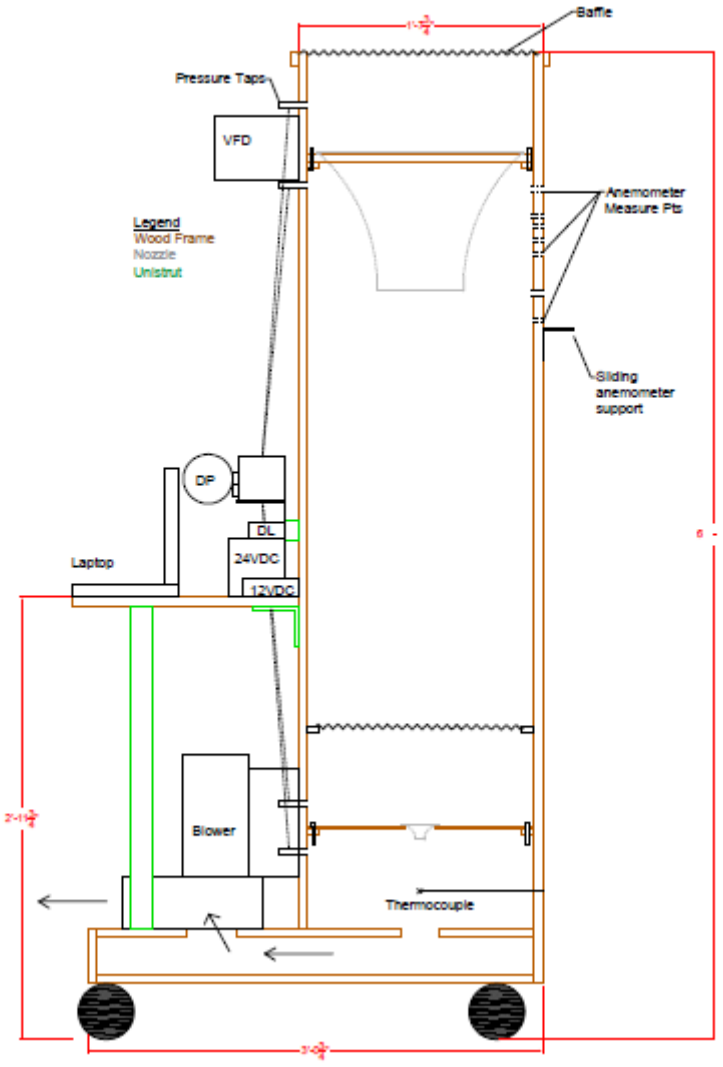

Figure 45: Anemometer calibration facility

Differential pressure in the calibration facility was measured across the bottom ¾" nozzle using a Rosemount 1151 differential pressure transducer. The calibration was valid for a velocity range across the bottom nozzle of 15-35 m/s. Atmospheric dry-bulb temperature, humidity, and pressure were recorded from measurements taken by a local weather station. From these data, air velocity through the bottom nozzle was determined. Air flow through the top nozzle was verified to be uniform within the precision of the anemometer (0.01 m/s). Therefore, velocity through the top, larger nozzle could be determined using geometry. The anemometer was placed at the outlet of

this top, larger nozzle. Four different sizes of top nozzle were used: 7", 5.5", 3" and 2", and the blower speed was also varied to achieve air velocities from 0.1 – 5 m/s. In this manner a calibration curve was determined for the anemometer.

Appendix C: Heat Loss Calibration

Heat loss calibration was performed for the system with single-phase water in the condenser tube, the fans off, and the air duct inlet and outlet covered with polyethylene foam insulation. Water was heated from the boiler and pumped through the condenser. The boiler power was adjusted to achieve three different inlet water temperatures. Inlet and outlet water temperatures were measured by beaded-wire thermocouples wrapped around the inlet and outlet copper pipes. This measurement location was required because temperature stratification of the water flow inside the flattened-tube condenser made accurate measurement of flow enthalpy difficult inside the condenser tube. Therefore, the test section length for this heat loss calibration was 10.98m, whereas the test section length for two-phase steam tests was only 10.72m. Water mass flow rate was measured at the condenser inlet using a Micromotion CMF025 Coriolis mass flow meter. The heat loss was determined for each inlet temperature, corrected for the longer test section length, and plotted to find a linear regression for the system UA value for single-phase water.

$$Q_{loss} = \dot{m}_f \left(c_{p,f,in} T_{f,in} - c_{p,f,out} T_{f,out} \right) \frac{L_{test}}{L_{heat\ loss}}$$

$$Q_{loss} = UA_{tot,1P} LMTD$$

$$LMTD = \frac{\left(T_{f,in} - T_{atm} \right) - \left(T_{f,out} - T_{atm} \right)}{\ln\left(\frac{T_{f,in} - T_{atm}}{\left(T_{f,out} - T_{atm} \right)} \right)}$$

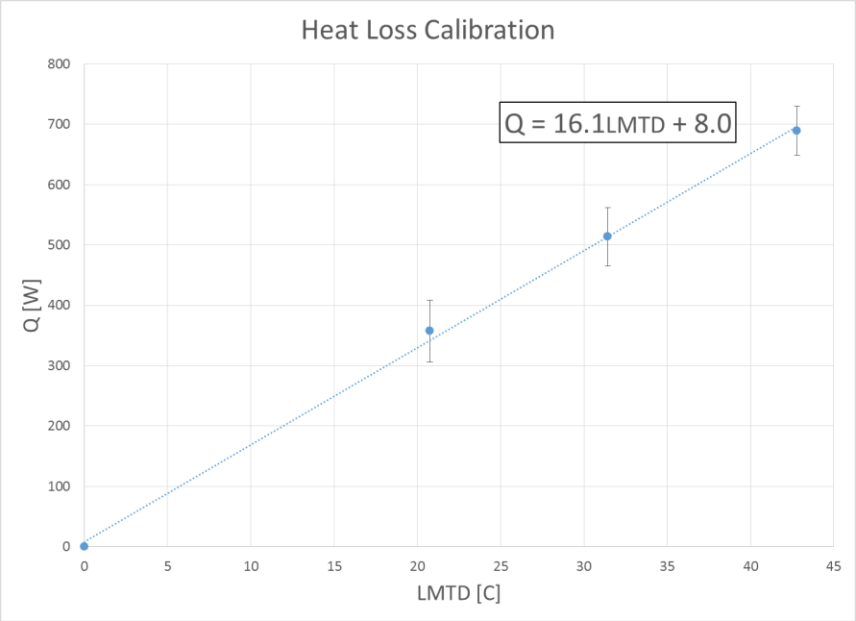

Figure 46: Heat loss at three different inlet temperatures, along with line of best fit

The $UA_{tot,1P}$ value of 16.1 W/K was found from a least-square linear regression. The uncertainty of $UA_{tot,1P}$ was 0.3 W/K.

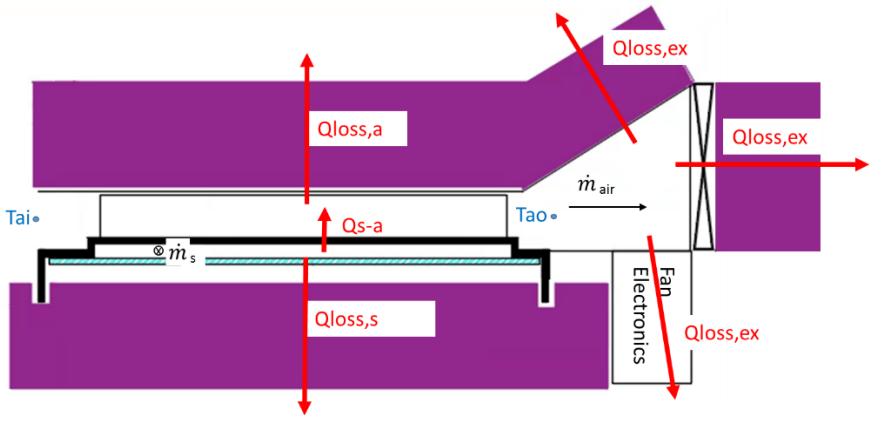

Figure 47: Schematic diagram of condenser cross-section during heat loss calibration

Total heat loss, and the total UA value, were then divided into three parts: heat lost from the steam-side, heat lost from the air-side test section, and heat lost from the excess air duct area outside of the test section. Theoretical UA values were calculated for each of the three sections, as follows:

$$UA_{s,1P,theory} = \left(\frac{1}{h_{nc}A_{s\,surface}} + \frac{t_{ins}}{A_{s\,surface}k_{ins}} + \frac{1}{h_{nc,enc,s}A_{a\,surface}} + \frac{t_{pc}}{A_{s\,surface}k_{pc}} + \frac{1}{A_{s\,surface}h_{1P}}\right)^{-1}$$

$$UA_{a,theory} = \left(\frac{1}{A_{a\,surface}h_{nc}} + \frac{t_{ins}}{A_{a\,surface}k_{ins}} + \frac{t_{stl}}{A_{a\,surface}k_{stl}} + \frac{1}{h_{nc,enc,a}A_{a\,surface}}\right)^{-1}$$

$$UA_{ex,theory} = \left(\frac{1}{A_{ex\,surface}h_{nc}} + \frac{t_{ins}}{A_{a\,surface}k_{ins}} + \frac{t_{stl}}{A_{a\,surface}k_{stl}} + \frac{1}{h_{nc,enc,a}A_{a\,surface}}\right)^{-1} +$$

$$\left(h_{nc}A_{conduit\,top}\right) + \left(\frac{1}{h_{nc}A_{conduit\,side}} + \frac{t_{pvc}}{k_{pvc}A_{coduit\,side}}\right)^{-1}$$

$$h_{nc} = 10\frac{W}{m^2K}$$

$$h_{nc,enc,s} = 2.5\frac{W}{m^2K}$$

$$h_{nc,enc,a} = 2.3\frac{W}{m^2K}$$

$$h_{1P} = \frac{k_f Nu}{d_h}$$

Where, for fully-developed laminar forced convection with uniform wall temperature and the tube is over 800 diameters in length, Nu = 3.66. The assumption of uniform wall temperature is a poor one, but the water flow is the minor heat transfer resistance, so its exact value does not have a large effect on the overall UA value.

$h_{nc,enc}$ was estimated using Markatos and Pericleous' correlation from a numerical model for natural convection inside a cavity [30].

$$\overline{Nu} = 0.143Ra^{0.299} \tag{47}$$

Rayleigh number for the steam-side enclosure was estimated at approximately 650, therefore an average Nusselt number of 0.99 was recommended, with average Nusselt number defined as:

$$\overline{Nu} = \frac{\bar{h}_{nc,enc} t_a}{k_a} \tag{48}$$

Steam-side heat transfer coefficient through the air enclosure was estimated to be 2.5 W/m^2-K. For the air-side, Ra, $\overline{Nu}$ and $\bar{h}_{nc,enc}$ were estimated to be 2830, 1.5, and 2.3 W/m^2-K, respectively.

The electrical conduit was not insulated during this test or during any of the data acquisition, and it contributed greatly to the third UA value being the highest. Theoretical UA values can be found in Table 6.

To verify the theoretical UA calculations, heat transfer through the steam and air-side insulations were then measured directly. On the steam side, a thermocouple was placed on the polycarbonate surface and on the insulation surface. Assuming the above value of enclosed-air natural convection heat transfer coefficient, and conduction through the insulation, heat flux was determined. Using this value for heat flux, and the LMTD between the internal water and the ambient, an experimental steam-side UA value was found.

On the air side, temperature on the inner and outer surfaces of the insulation were measured directly, and heat flux by conduction through the insulation was determined. Using this value for heat flux, an experimental air-side UA value was found.

Using the experimental values for heat transferred through the air- and steam-sides, the remaining quantity of heat lost by the water in the condenser was assumed to be lost through the excess area. This area was located at the top of the air duct. Therefore, the temperature difference was defined as:

$$\Delta T_{excess} = (\bar{T}_{ao} - T_{atm})$$

$$UA_{excess} = \frac{Q_{excess}}{\Delta T_{excess}}$$

Table 6: Heat transfer surface areas and UA values, both theoretical and measured

	Area [m^2]	UA [W/K]	
		Theoretical	Measured
Steam-side	3.2	1.4	1.4
Air-side	3.2	1.4	1.4
Excess Area	4.2	12.7	13.3
Total	10.6	15.5	16.1

The measured UA values for the air-side and steam-side were nearly identical to the theoretical values. The UA value for the excess area was slightly greater than expected. This value is not important, in that it is not involved in any calculations for the two-phase data. The accuracy of this value only aids in validating the heat loss model. Due to the similarity between the theoretical and measured results, the theoretical results are used, after correcting for the slightly different conditions found during two-phase measurements.

The steam-side UA measurement was adjusted to assume a steam-side heat transfer coefficient based on Nusselt condensation in place of the h_{1P} value used during the heat loss calibration. The air-side UA value was adjusted to assume a higher heat transfer coefficient for the forced internal convection of air. The final UA_{loss} values and anticipated heat loss during two-phase tests were:

Table 7: UA_{loss} values for steam-side and air-side

	UA [W/K]	Q [W] (anticipated)
Steam-side	1.4	110
Air-side	1.7	50

The UA values were then used to correct the energy balances on both sides:

$$Q_a = \dot{m}_a c_{p,a}(T_{ao} - T_{ai})$$

$$Q_a = Q_{s-a} - Q_{loss,a}$$

$$Q_s = \dot{m}_s c_{p,s}(T_{si} - T_{so})$$

$$Q_s = Q_{s-a} + Q_{loss,s}$$

$$Q_{s-a} = Q_a + Q_{loss,a}$$

$$Q_{s-a} = Q_s - Q_{loss,s}$$

$$Q_{loss,s} = UA_{loss,s} * LMTD_s$$

$$Q_{loss,a} = UA_{loss,a} * LMTD_a$$

$$Energy\ Balance\colon\ Q_s - Q_{loss,s} = Q_a + Q_{loss,a}$$

Appendix D: Air (T_{ao}) Temperature Profile

The air-temperature measurement was prone to error due to the measurement being made at a discrete point within the air flow. Across the air duct, the air flow varied in both velocity and temperature. To accurately find the average air temperature, the spatial temperature profile was measured across the air duct at the location of the T_{ao} measurements. In addition, the air velocity profile was modeled at the measurement location. These two profiles were combined to find an average temperature of the flow from the Tao measurement.

$$T_{ao,average} = \frac{\sum_{i=1}^{N} v_{air,i} T_i}{v_{air,average}}$$

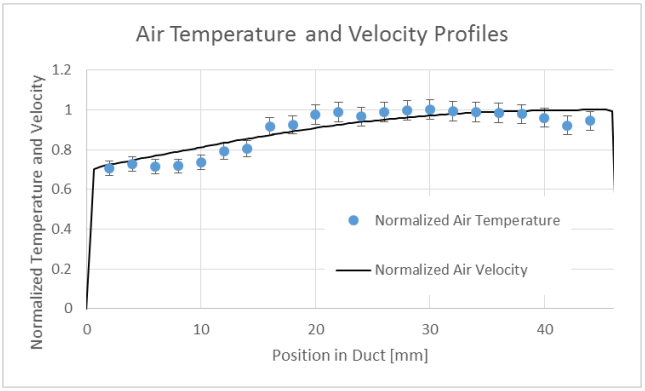

Figure 48: Modeled velocity and measured temperature profiles in air duct

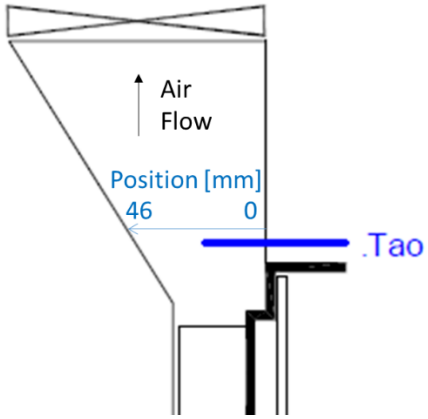

Figure 49: Schematic drawing of air temperature measurement

The air velocity profile was determined from a 2-D Fluent model. The air duct cross-section was modeled assuming no flow resistance due to the fins and laminar flow of air ($Re_{Dh} > 650$).

An outlet velocity profile was imposed based on a sinusoidal axial fan profile. A uniform inlet velocity profile was also modeled, and it did not produce a significant change in the results. A

uniform velocity outlet profile was then modeled. This produced approximately a 4.5% increase in the predicted average temperature. Physically, this boundary condition is the least accurate of the three assumptions. The sinusoidal axial profile was selected due to it being the most physically accurate. The uncertainty in average temperature caused by the uncertainty in boundary conditions is discussed in Appendix I.

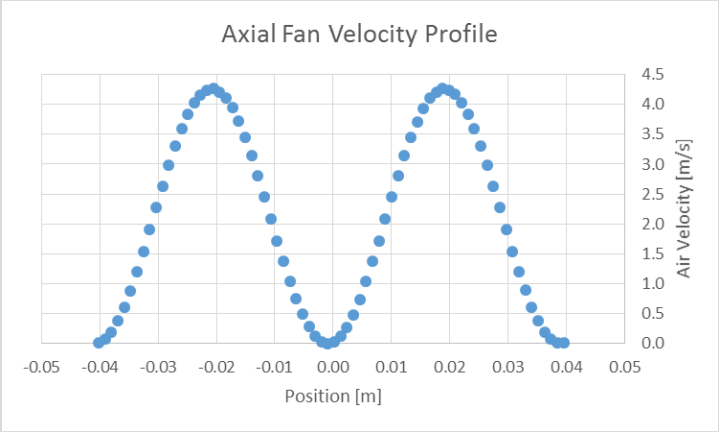

Figure 50: Axial fan profile for fluent model

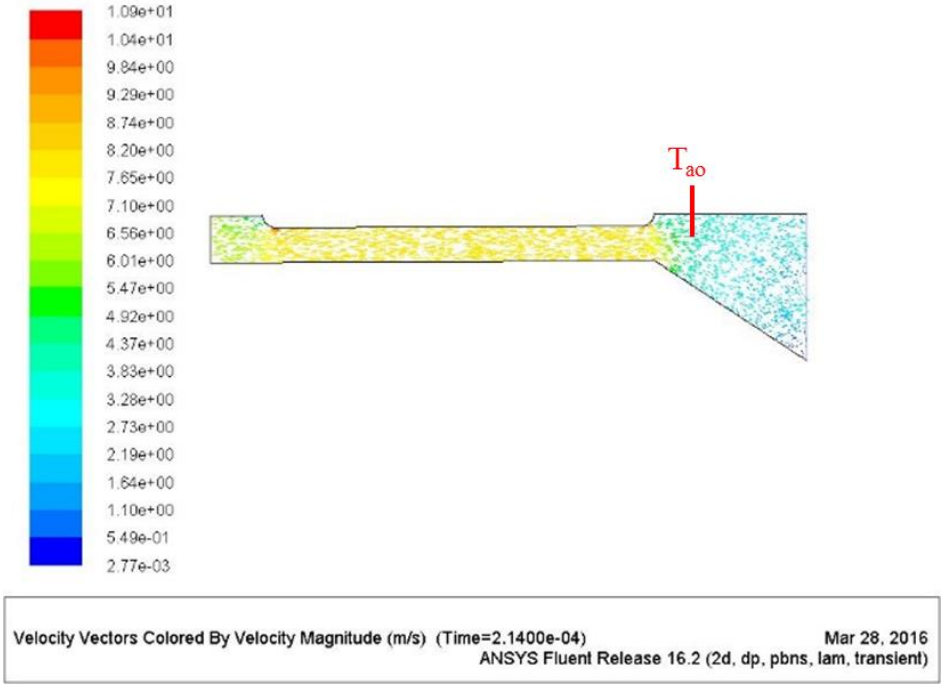

Figure 51: Velocity vectors of airflow in air duct. A high velocity gradient is present in the vicinity of the Tao measurement

Position of each thermocouple probe in the duct was measured, and a correction factor for each measurement was applied.

Table 8: Position of and correction factors for Tao measurements

Measurement Point	Distance from top of duct [mm]	Correction Factor on T_{ao}
1	14.8	1.06
2	18.5	0.99
3	19.9	0.96
4	16.8	1.02
5	18.5	0.99
6	17.7	1.00
7	17.2	1.01
8	19.5	0.97
9	22.3	0.93
10	19.5	0.97
11	20.7	0.95
12	14.3	1.07

Appendix E: Energy Balance Verification

A verification of the system energy balance was made between the condenser hot and cold sides. Single-phase water was run on the hot side, and the fans pulled cooling air on the cold side. Water mass flow rate was measured with a Micromotion CMF025 coriolis mass flow meter. As in the heat loss calibration, inlet and outlet temperatures were measured with T-type welded-bead thermocouples attached to the walls of the inlet and outlet copper pipes. On the air side, air inlet velocity and inlet and outlet temperatures were measured. Heat loss was accounted for, and an error was determined:

$$\%Error = \frac{Q_a - Q_s}{Q_a} \times 100\%$$

Table 9: Water inlet temperature, water and air heat transfer, and % error

Tsi	Qs	Qa	% Error
C	kW	kW	
36.8	5.63	3.52	37%
38.7	6.38	3.95	38%
54	12.7	8.28	35%
56.7	13.7	9.00	34%
59.7	8.48	9.82	-16%

The first four tests had a significantly higher heat transfer measurement on the water side than on the air side. The final test had a higher heat transfer measurement on the air side. The large decrease in heat transfer measured on the water side for the final data point raised doubts about its validity and it was discarded.

Appendix F: Contact Angle Measurements

Contact angle of water was measured on both a rusted and a clean section of the steel condenser tube. Contact angle was measured using a goniometer. A small droplet of water was gently placed on the horizontal steel surface and a picture was taken of the droplet and steel. Contact angle was then measured using the KSV CAM Optical Contact Angle and Pendant Drop Surface Tension Software.

Advancing and receding contact angles were also measured using a similar procedure. For the advancing contact angle, water was slowly added to the droplet while pictures were taken at 0.3 s intervals. The contact angle of the droplet slowly increased until reaching a critical angle and the contact point slipped along the steel surface. This critical angle was the advancing contact angle. Receding contact angle was measured by slowly removing water from the droplet. For the receding case, the contact point never slipped along the steel surface, indicating a receding contact angle of 0°.

As expected, static and advancing contact angles were significantly higher for the clean tube than for the rusted tube. In addition, uncertainty of the contact angles was much lower for the clean tube. The rusted tube had an irregular surface, making the contact angle dependent on the area tested.

Table 10: Static, advancing and receding contact angles for water on clean condenser tube

Clean Tube			
	Static	Advancing	Receding
Contact Angle [deg]	95	114	0
Range [deg]	93-98	114-115	0
Beta (abs)	0.17	1.6	0
Std Error	1.3	0.5	0



Figure 52: Clean condenser face

Table 11: Static, advancing and receding contact angles for water on rusted condenser tube

Rusted Tube			
	Static	Advancing	Receding
Contact Angle [deg]	52	74	0
Range [deg]	38-61	63-85	0
Beta (abs)	1.8	0.73	0
Std Error	4.2	11	0



Figure 53: Rusted condenser face

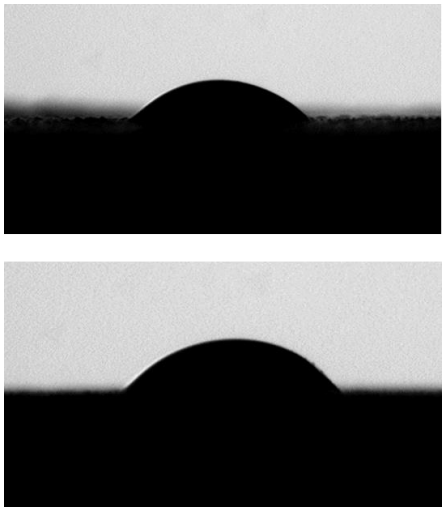

Figure 54: Static water droplet on rusted condenser surface

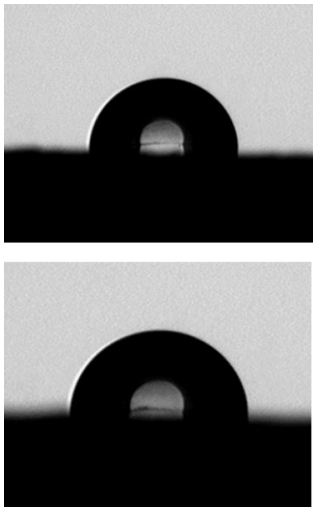

Figure 55: Static water droplet on clean condenser surface

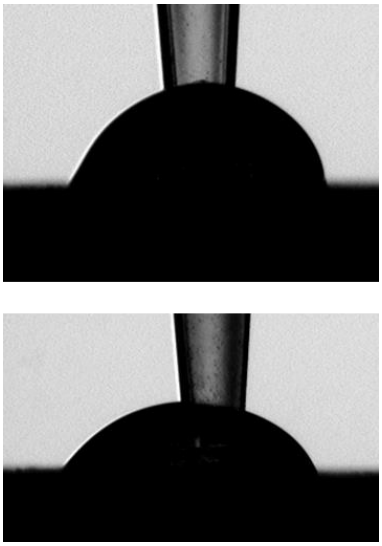

Figure 56: Advancing water droplets on rusted condenser surface

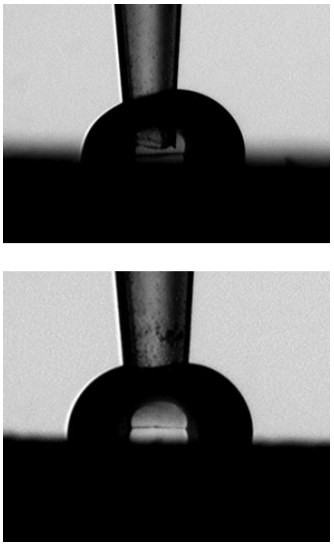

Figure 57: Advancing water droplets on clean condenser surface

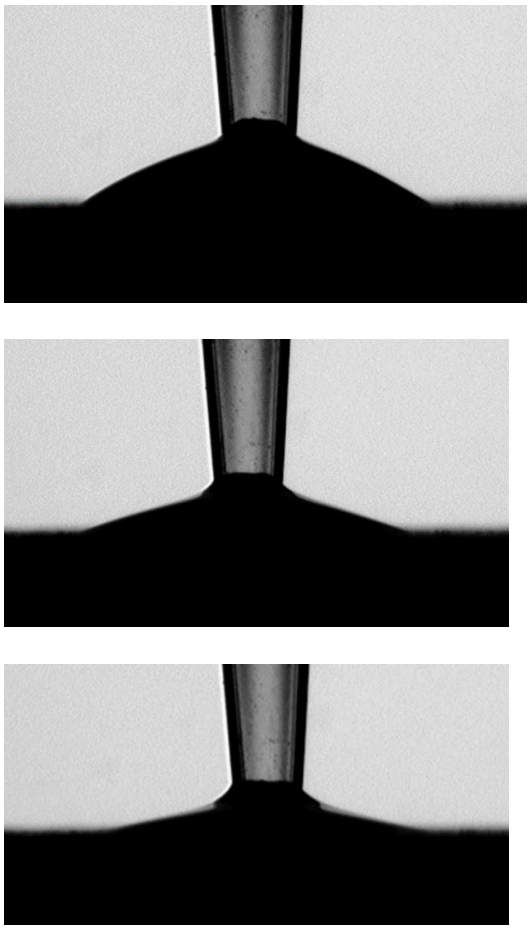

Figure 58: Receding water droplet sequence on rusted condenser surface

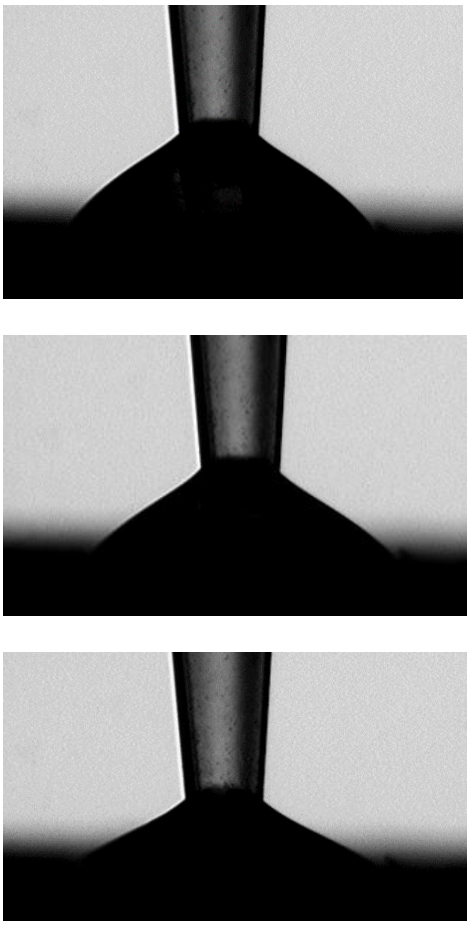

Figure 59: Receding water droplet sequence on clean condenser surface

Appendix G: Engineering Design

G.1 Inlet Steam Heater

One half of the energy balance was a measurement of condensate flow rate, with an assumption that all condensate exiting the condenser had condensed inside the condenser:

$$\dot{Q}_C = \dot{m} h_{fg}$$

In order to validate this assumption, the inlet steam had to be slightly superheated. Therefore, the above equation became:

$$\dot{Q}_C = \dot{m}(h_{fg} + (i_{sh} - i_{sat}))$$

To create superheated steam, the steam was heated and passed through a choke valve before entering the condenser. In order to design the heater and valve system, the un-treated inlet bulk enthalpy needed to be predicted. First, the steam quality at the boiler exit needed to be predicted. The steam leaving the boiler always entrained some fluid. Ramirez de Santiago and Marvillet [31] experimentally found the fluid entrainment limit to be 8.8×10^{-5} kg liquid/kg vapor. Sterman's [32] correlation for pool-boiling liquid entrainment, when applied to our system, estimated an entrainment of 4.8×10^{-6} kg liquid/kg vapor. Sterman's result was approximately 20 times greater than that of Ramirez de Santiago, so the greater result was used to ensure adequate sizing of the inlet heater.

$$E_{fg,Sterman} = 6.09 \times 10^{9} j_g^{*2.76} h^{*-2.3} \left(\frac{\rho_g}{\Delta\rho}\right)^{-0.26} N_{\mu f}^{2.2} \left(\frac{\Delta\rho}{\rho_f}\right)^{1.1}$$

$$j_g^* = dimensionless\ superficial\ gas\ velocity$$

$$h^* = dimensionless\ height\ above\ liquid\ surface$$

$$N_{\mu f} = liquid\ viscosity\ number$$

In addition to the fluid entrainment, the steam underwent condensation along the length of the 50-foot steam hose from the boiler exit to the condenser inlet. Using Shah's [4] correlation for internal convective turbulent condensation, estimated heat loss along the pipe was 677 W.

$$h_{shah} = h_{dittus-boelter}\left[(1-x)^{0.8} + \frac{3.8x^{0.76}(1-x)^{0.04}}{(P/P_c)^{0.38}}\right]$$

$$h_{dittus-boelter} = 0.023\left(\frac{k_l}{D}\right)\left(\frac{GD}{\mu_l}\right)^{0.8} Pr_l{}^{0.4}$$

In order to ensure 1°C of superheat, the inlet vapor required a power input of 710 W. A Watlow mineral-insulated nozzle heater with a rating of 1300W at 240VAC was selected. In order to account for losses to the ambient, the required heater power was 760 W. At this power, the copper pipe was expected to reach a temperature of 269°C. This was above the melting temperature of solder, so the copper fittings were brazed. In addition, with a desired steam temperature of 101°C, a large radial temperature gradient was expected in the steam flow. To counteract this, the heater was installed 30 cm upstream of the inlet header. This allowed time for the flow to mix before entering the condenser.

In addition to the heater, a brass gate valve was installed downstream of the heater and before the inlet header. This gate valve served three purposes:

1) Helping to mix the flow to ensure a more uniform temperature at the inlet of the condenser

2) Superheating the vapor by lowering the pressure, thereby decreasing the required heater power, and lowering the temperature gradient.
3) Providing a greater resistance to heat conduction along the copper pipe, thereby protecting the polycarbonate flow-guiding insert in the inlet header.

With these system modifications, inlet superheat of up to 0.1° C or more was achieved for all but the horizontal data points.

G.2 Inlet Flow Guides

In order to compare all sections of the condenser under equal conditions, a short entrance length was desired. A computational fluid dynamics (CFD) model of the system in Fluent indicated that entrance length without an inlet flow guide would be over 0.66 m in length. This would complicate the comparisons between the inlet portion of the condenser and downstream sections.

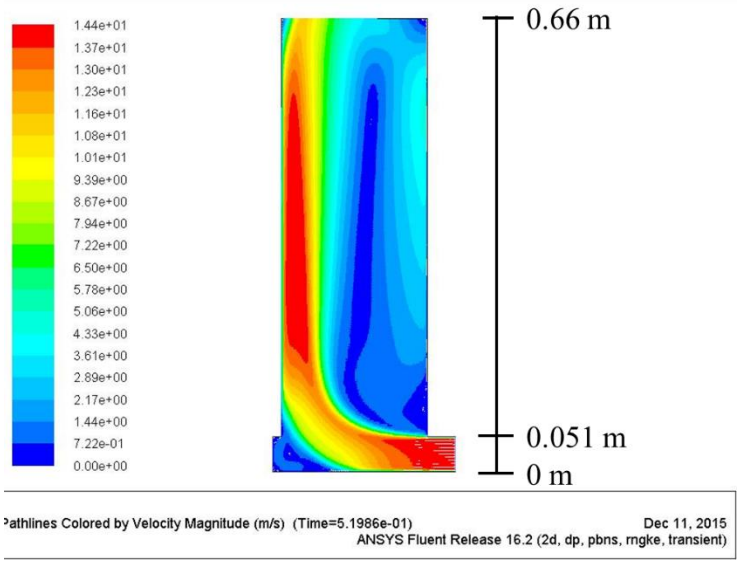

Figure 60: Fluent simulation of inlet vapor flow without flow guide

As a result, a polycarbonate flow-guide insert was designed to be installed inside the copper-pipe header. The polycarbonate was necessary to withstand the steam saturation temperature of 100° C. The design was modeled in Solidworks, and manufactured with a Fortus 360 MC fused-deposition-modeling machine.

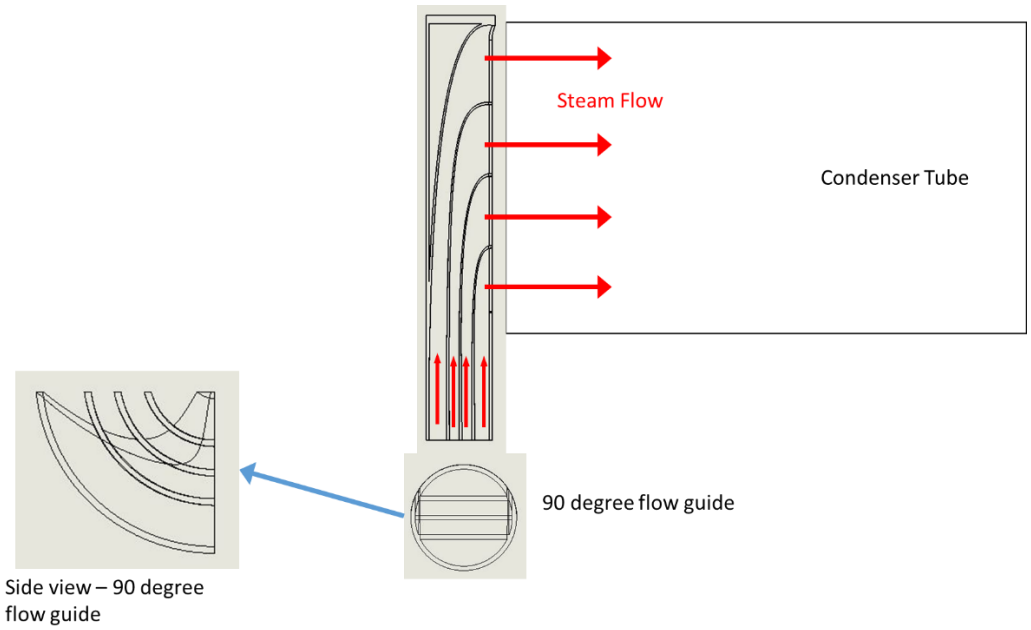

Figure 61: Schematic diagram of flow in header flow guides

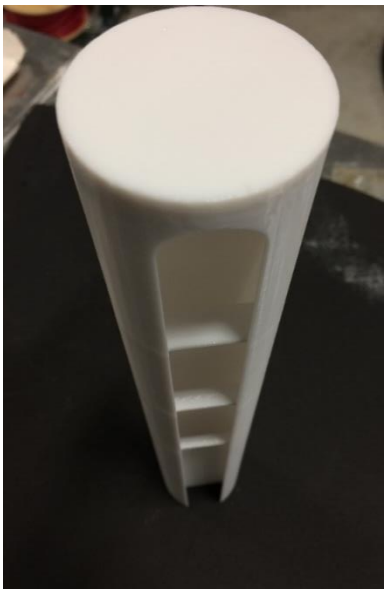

Figure 62: Polycarbonate header flow guide



Figure 63: Inlet header before installing flow guide

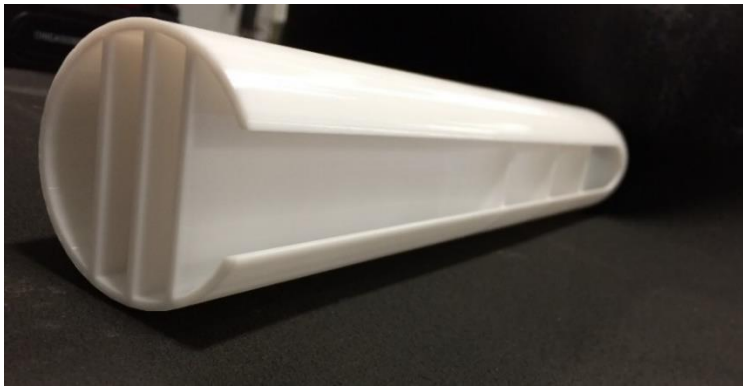

Figure 64: Polycarbonate header flow guide

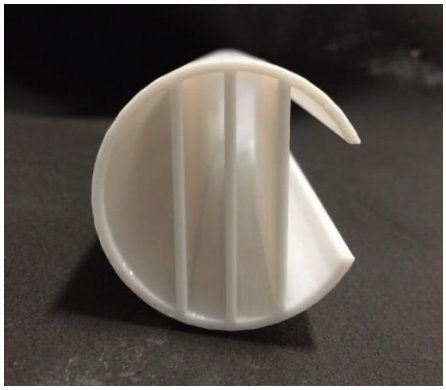

Figure 65: Polycarbonate header flow guide



Figure 66: Header flow guide being inserted in header

G.3 Air Duct and Fan Design

The test facility had an inherently different air-side design than that of an operating ACC. An operating ACC has an array of condensers in an A-frame configuration, with a single row of axial fans at the base of the condensers

The test facility had only one condenser, and used an array of small axial fans along the length of the condenser, pulling air in a cross-flow pattern to the steam flow. This design had the advantage of customizability. The individual fans were connected to potentiometers, and therefore could be varied in speed.

The facility required a maximum velocity of 3 m/s through the condenser fins. The fin height was 19mm, therefore a volumetric flow rate per unit length of .057 m^2/s was required. In order to generate the required velocity, an axial fan with diameter much large than the fin height was required. To verify the correct fan size, a CFD model was completed using Fluent software.

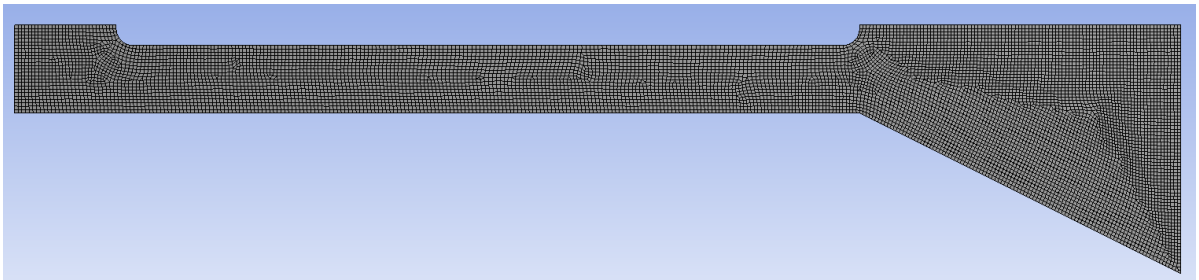

Figure 67: Mesh for CFD model of air flow through air duct

For the simulations, three different fan sizes were investigated: 60mm, 80mm, and 100mm. The basic air-duct geometry remained the same, while the fan opening was varied. Because of the large variety of fans available, and the wide range of flow rates reported by manufacturers, an average flow-rate of the low-cost providers was used for each fan size. The air velocity was

approximated to have a sinusoidal profile at the fan exit. The equation and profile for the 80mm fan were:

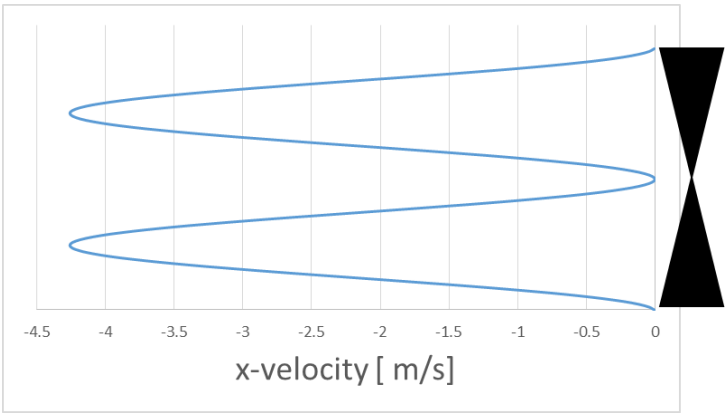

Figure 68: 80mm fan x-velocity profile

$$v(y) = \frac{4.261}{2}\sin\left(\frac{y + .0475}{.0058489} - \frac{\pi}{2}\right) + 1$$

In Fluent, a 2-D model was used for all simulations. A meshing element size of 1e-3 m was used, resulting in approximately 10,000 elements in each mesh. The mesh for the 80mm design can be seen above. With an expected air velocity of 3 m/s, the Reynolds number based on fin height was 3,170. Therefore, a turbulent k-epsilon, RNG model was used, with standard wall functions. The model converged to a steady-state solution with residuals of all equations below 1e-3.

Average and maximum velocity results can be seen below for all three fan sizes. From the results below, it is clear that all three fans provided the required 3 m/s velocity. However, this 2-D simulation neglected the effects of a narrow channel width between the fins, with would cause a significant pressure drop. Therefore, the actual air velocity was expected to be lower than the simulated velocity. As a result, a factor of safety of two was used, resulting in the selection of the 80mm fans.

CFD Results		
Fan Diameter	**Vmax**	**Vave**
[mm]	[m/s]	[m/s]
60	6.91	5.70
80	9.00	7.72
100	8.59	7.32

Figure 69: Maximum velocity in air duct, average velocity at vertical cross section at midpoint of constant-size duct section

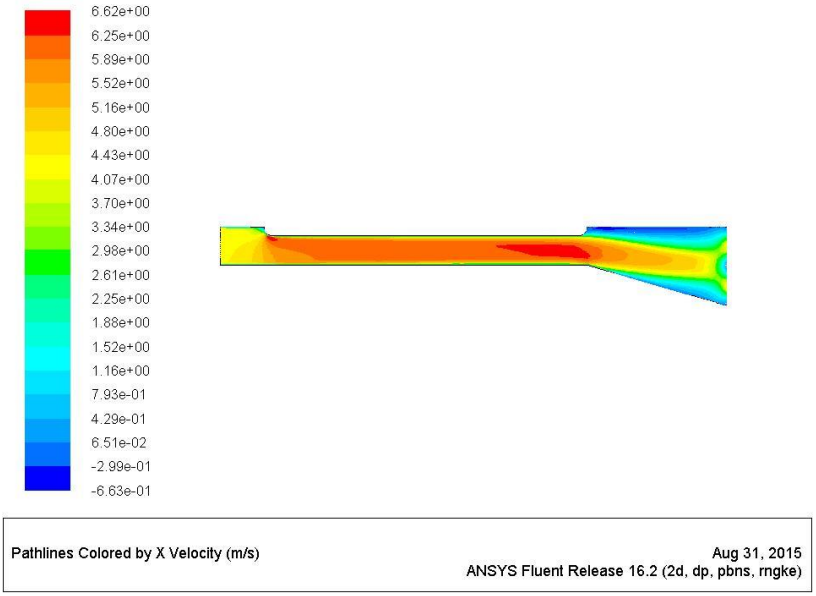

Figure 70: X-Velocity pathlines for 60mm fan design

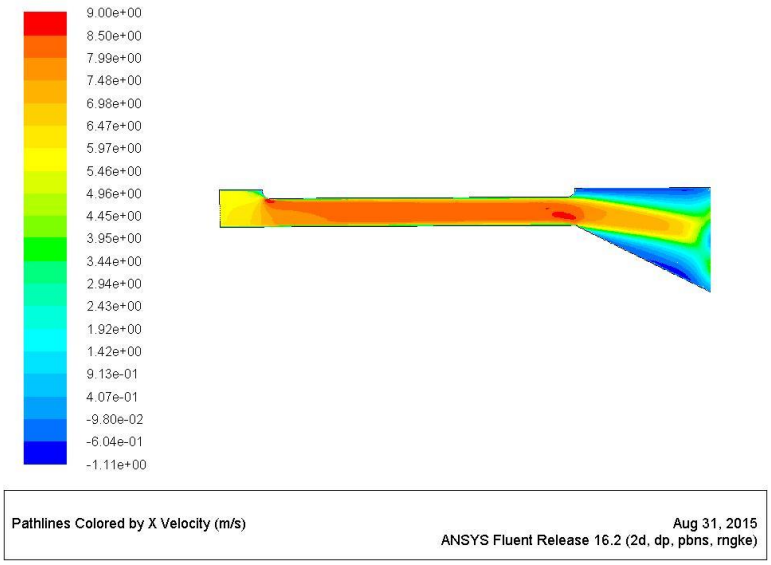

Figure 71: X-Velocity pathlines for 80mm fan design

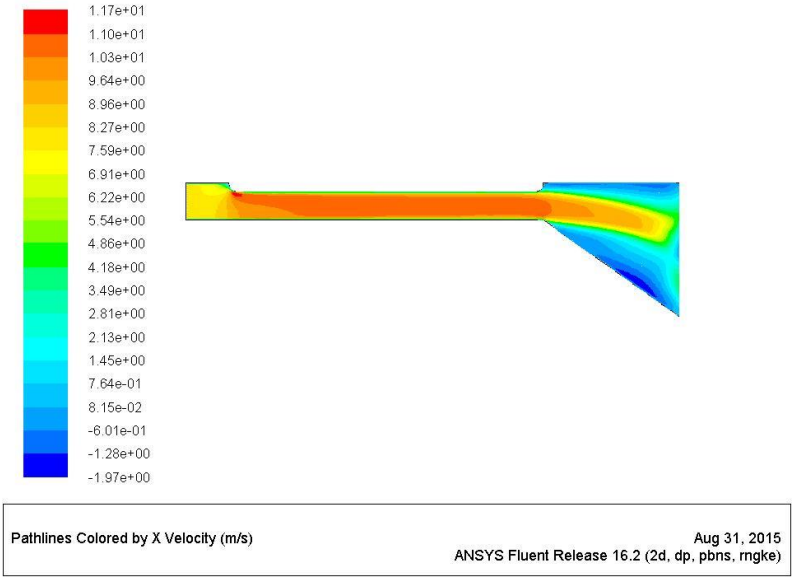

Figure 72: X-Velocity pathlines for 100mm fan design

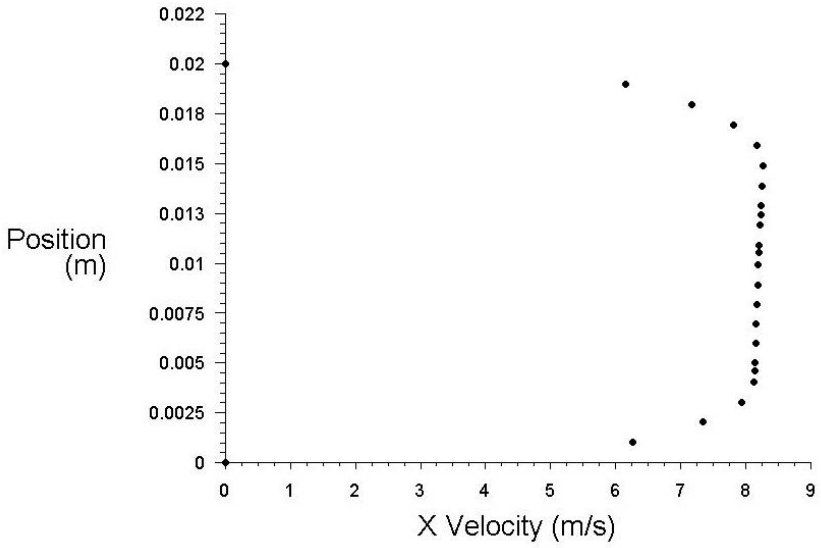

Figure 73: magnitude of x-velocity at a cross section halfway along straight duct section

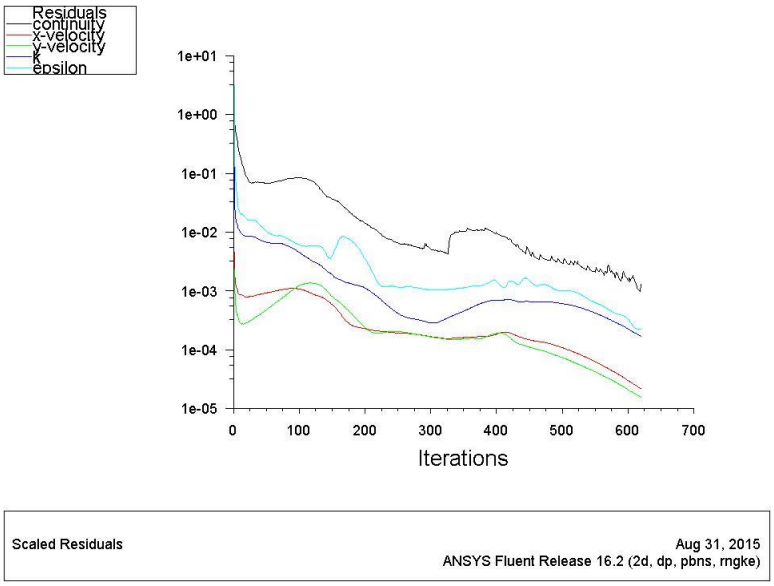

Figure 74: Residuals for 100mm fan design; the 60mm and 80mm designs required fewer iterations to reach convergence

G.4 Wall Temperature Measurement

Due to the large uncertainties in measuring air temperature and velocity, the determined local heat transfer coefficient, $h_{s,local}$ had a large initial uncertainty when making measurements on the pilot system. This could be improved greatly by calculating $h_{s,local}$ using the difference between saturation and wall temperature. Accurate measurement of T_w was able to decrease the uncertainty in $h_{s,local}$ for the pilot system to 11%. However, the measurement of T_w also needed refinement in the pilot system.

To test different Tw measurement techniques, thermocouples were embedded in the condenser tube at three different Z locations and three different X locations, for a total of nine measurements (one measurement was faulty and was omitted).

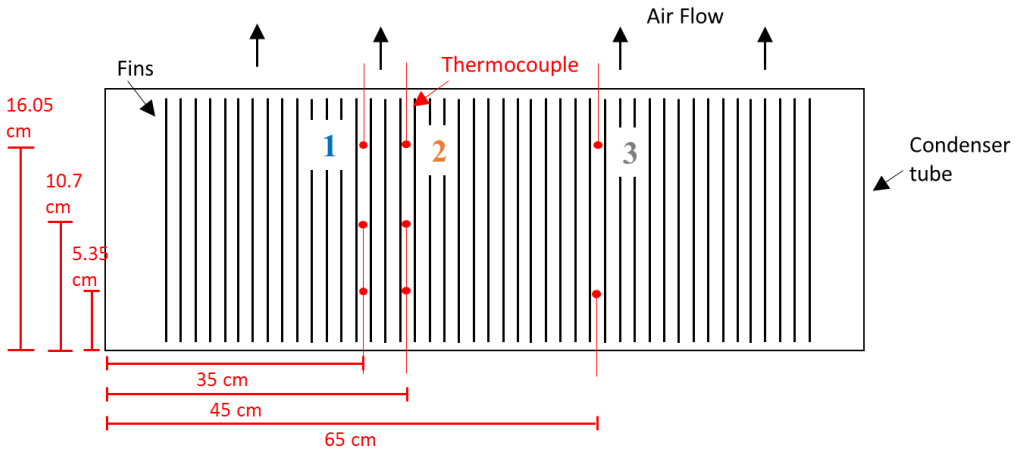

Figure 75: Position of wall thermocouples

The thermocouples were inserted from the air side. Holes were drilled to insert the exposed portion of the 30-ga thermocouple wire into the wall. The holes were then covered with JB Weld epoxy to affix and insulate the thermocouple. In addition to varying position, the embedding method was also varied. Three different embedding techniques were used: a hole drilled completely through

the wall, a hole drilled exactly to the size of the thermocouple bead but stopping halfway through the wall, and a large hole drilled halfway through the wall.

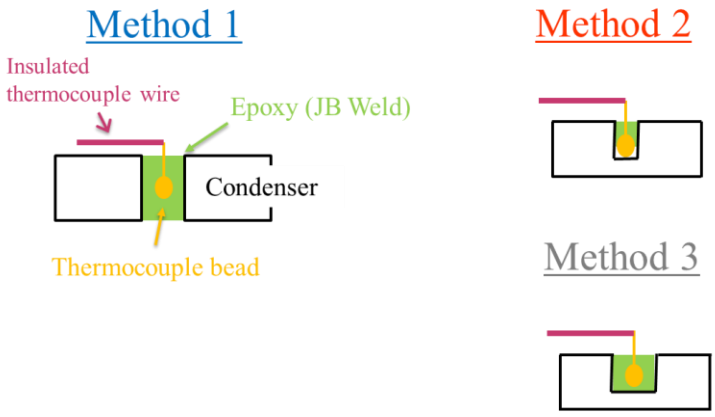

Figure 76: Wall thermocouple embedding methods: hole drilled completely through wall, tight hole, large hole

The second method was expected to be the best, because it provided the best thermal contact between the thermocouple and wall, as well as insulating the bead from the steam and the air. The results showed that the first and second method produced similar results, with the first method reading slightly higher temperatures. The third method produced significantly lower temperatures, likely due to its poor thermal contact. The higher temperatures of the first method were assumed to be due to leaking of steam into the hole. Therefore, the second method was selected as the most reliable.

Also, as expected, wall temperature increased greatly from air inlet to air outlet. This was due to the lower air temperature at the inlet, leading to a much higher rate of heat transfer. As a result of this temperature difference, wall temperature measurements were made at two different x-location for every measure point on the final system.

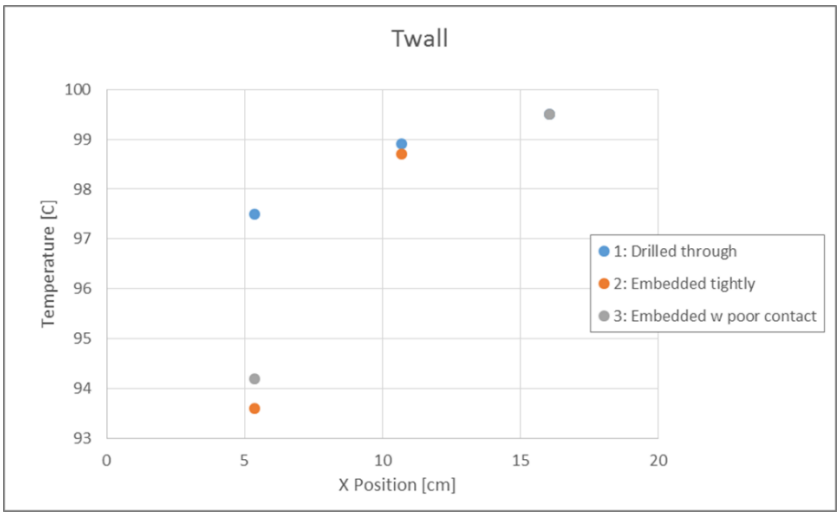

Figure 77: Results of three different measurement techniques and three different x locations

G.5 Condenser and Viewing Window

In an industrial setting, the air-cooled condenser is a flattened steel tube, with aluminum fins on each flat side. The individual condenser is approximately 11m long, and is arranged in an A-frame array of approximately 20 condenser tubes, with axial fans running along the bottom. The tube itself is made of structural steel, 2 mm thick, with a width of 214 mm and a height of 20 mm (inner dimensions).

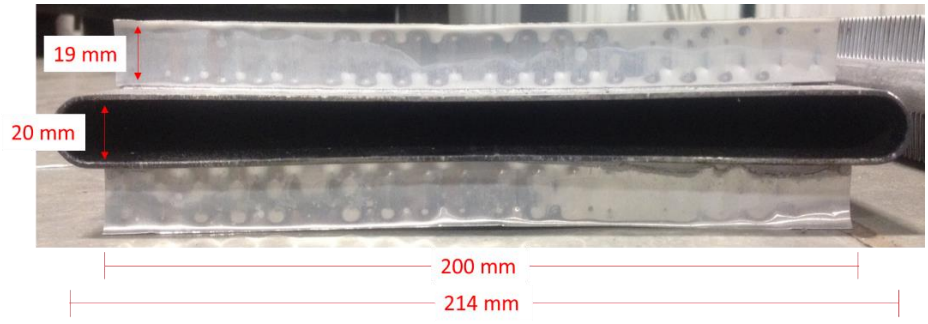

Figure 78: End view of full-tube condensers and fins



Figure 79: Side view of condenser tube and fins

In order to allow visualization of the steam condensation, the tube was cut in half, and a polycarbonate viewing window was placed along the open condenser tube.

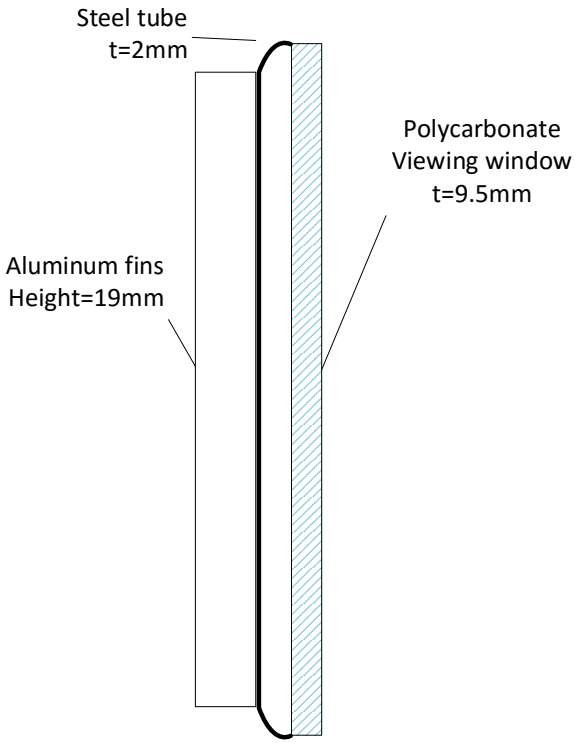

Figure 80: Schematic drawing of half-tube cross section with viewing window

Despite the relatively simple geometry, the design of a facility for a half-tube was made complex due to the weakness of the structure. Due to its length, the half tube could not support its own weight. To solve this instability, 1”x1” steel flanges were welded along the half-tube edges. The

entire system was then attached to a 20.5”x20.5” aluminum truss for support when lifting to various inclination angles.

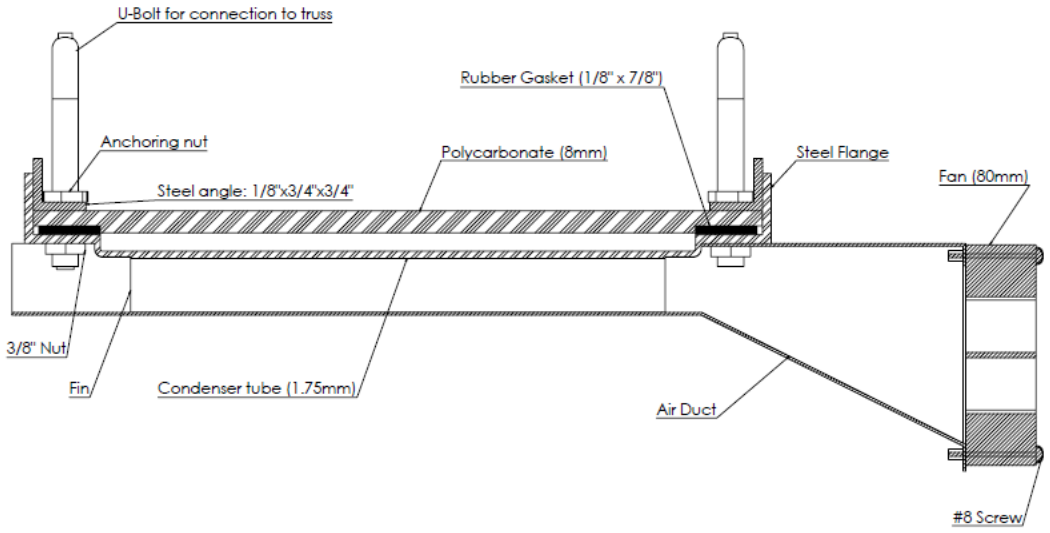

Figure 81: Construction diagram of condenser half-tube cross-section

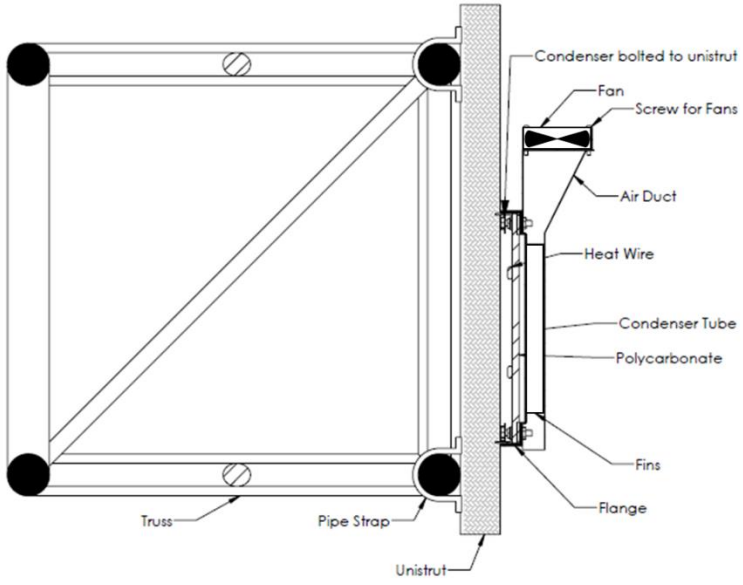

Figure 82: Construction drawing of test facility cross-section

G.6 Avoiding Condensation on Viewing Window

Avoiding condensation on the viewing window proved difficult due to the large temperature difference between the condensing steam (100 ^{o} C) and the outside air (20° C). Once the insulation was removed, condensation along the entire viewing window obscured all visibility. This condensation could either be removed or prevented. Removal was performed by adding heat via a 300W lamp. The lamp was positioned to shine light onto the viewing window of the condenser tube, while simultaneously measuring the surface temperature of the viewing window. The surface thermocouple was shielded by aluminum foil to eliminate radiation effects. The lamp position was varied until the surface temperature maintained a steady state of 100 ^{o} C. This temperature indicated that no excess heat was added to or lost from the system, and the visualization results would be accurate. This was achieved at a lamp distance of 121mm from the viewing surface.

Finally, the condensation removal procedure proceeded in two steps. First, the lamp was positioned a distance of less than 121mm from the viewing window to evaporate condensate off of the window. Second, the lamp was moved to the equilibrium distance of 121mm to ensure an adiabatic viewing surface. This technique was relatively simple and did not complicate the built facility. However, it only yielded a small 0.17 m^2 viewing window, and in total it required about 45 min to clear the window of condensate and then allow the condenser to return to steady-state.

The alternative, and more desirable method was to avoid condensation on the window completely. This could be achieved via two methods – insulating with foam, or insulating with a second layer of polycarbonate. Both methods also utilized an air layer and constant-wattage heat wire. The polycarbonate method was desirable because it allowed visualization without having to remove the insulation layer. The foam insulation was easier to design and install, however.

To calculate the thickness of the insulation and amount of heat wire required, the system was modeled as a series of thermal resistances, depicted in Figure 83 below. To avoid condensation on the inner surface of the polycarbonate, a 1° C temperature drop through the viewing window was assumed, and all the heat lost was designed to be replaced by heated wire. Starting from this assumption of 99° C surface temperature of the polycarbonate, to the atmospheric temperature of 20° C, three resistances were present. In order, they were the layer of trapped air, the outer layer (foam insulation or polycarbonate) and natural convection of air on the outer surface. Heat transfer coefficient for natural convection of air was assumed to be 10 W/m^2-K.

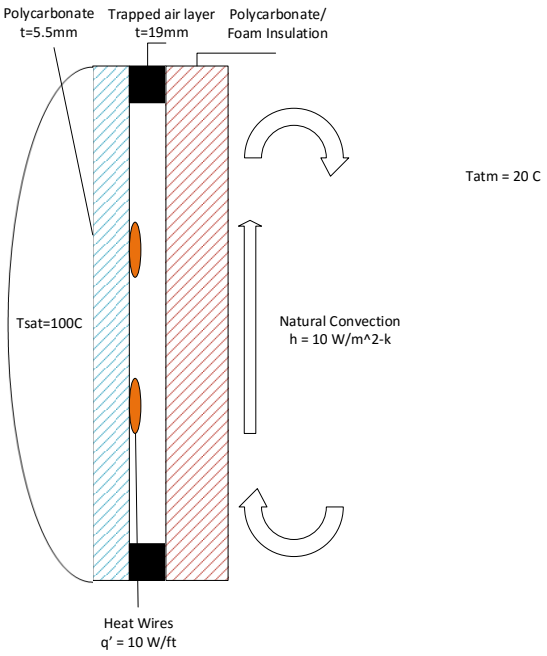

Figure 83: Schematic diagram of two-pane viewing window with heated wires

Layer	t	k	h	r
	m	W/m-k	W/m^2-K	m^2-K/W
Polycarbonate	0.0055	0.23	-	0.024
Trapped Air	0.0191	0.031	-	0.62
Foam Insulation	0.0508	-	-	2.21
Natural convection	-	-	10	0.1

Table 12: Properties of thermal resistances on viewing window

Using the thickness of the inner layer of polycarbonate and the temperature difference of 1° C between its inner and outer surfaces, the heat transfer was calculated.

$$q' = k\frac{dt}{dx}width$$

$$k = 0.23\ \frac{W}{m\,K}$$

$$\frac{dt}{dx} = \frac{1℃}{5.5\ mm}$$

$$width = 0.214\ m$$

This yielded a heat transfer of

$$q' = 8.9\frac{W}{m} = 2.7\frac{W}{ft}$$

The resistances in series were added to yield:

$$R = r_{air} + r_{foam} + r_{nc}$$

Using the calculated heat transfer and a temperature difference of 79° C, the necessary foam insulation resistance was calculated:

$$q' = \frac{dT * w}{R}$$

$$r_{foam} = 1.2\ \frac{m^2K}{W}$$

Using Johns Manville foil-faced foam insulation, this R-value corresponded to an insulation thickness of 1.5".

To validate this calculation, the system was tested with 2" foam insulation. At steady-state, the surface of the polycarbonate was only 89° C, instead of the required 99° C. When removing the insulation, condensation was observed along the entire viewing window. As a result, the insulation thickness was changed to 3" (with a corresponding R-value of 3.36 m^2-K/W), and two 10 W/ft heat wires were attached to the inner wall of the insulation. This configuration yielded a window surface temperature of 95° C. When removing the insulation, condensation was observed covering approximately half of the viewing window. This was acceptable for visualization.

The second method, using a second pane of polycarbonate, had an advantage over foam insulation in that the entire viewing window was visible while still being covered by an insulating layer. When using foam insulation, the insulation must be removed to observe and record the in-tube condensation. While the foam was removed, the condensation slowly covered the viewing window.

Required thickness of the second pane of polycarbonate was calculated in a similar manner to that of the foam insulation. Using the same 10 W/ft heat wire, the required polycarbonate thickness was found to be 5 mm. The system was tested with a 5.5 mm sheet of polycarbonate, and the results were not satisfactory. As can be seen below, less than half of the window was visible, and only in the regions adjacent to the heat wire. Strips of aluminum tape were used in an attempt to distribute the heat, but the distribution was still poor. In the end, the first method of opaque insulation without heated wires was used, and condensation was removed with the lamp.



Figure 84: Condensation on viewing window with two-pane polycarbonate and heated wires

G.7 T_{ao} Radiation Shield

The thermocouples measuring air exit temperature were exposed to the white air duct surface which was at a lower temperature than the air. Therefore, the thermocouples were anticipated to measure a lower temperature than the surrounding air temperature due to heat loss by radiation to the surrounding air duct. The potential error was calculated by equating heat lost by radiation and heat transferred to the thermocouple by convection of the air. Convection heat transfer was estimated using the Hilpert correlation [33].

$$Nu_{conv} = 0.683 Re^{0.466} Pr^{1/3}$$

$$Q_{rad} = \frac{A_{Tao}}{2} \sigma_B \left({T_{ao}}^4 - {T_{duct}}^4 \right)$$

$$Q_{rad} = Q_{conv}$$

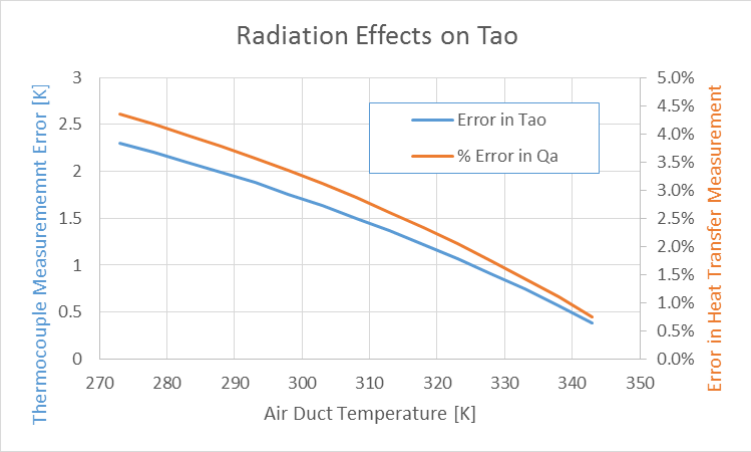

With an air duct temperature around 50° C, anticipated error in Q_a was approximately 2%. Therefore, a radiation shield was installed for the T_{ao} thermocouple probes. The shield support was designed in Solidworks and manufactured using selective laser sintering. The radiation shield was made from aluminum foil and attached to the pair of supports pictured below. The shield was designed to allow air flow past the thermocouple while still shielding the probe from the air duct.

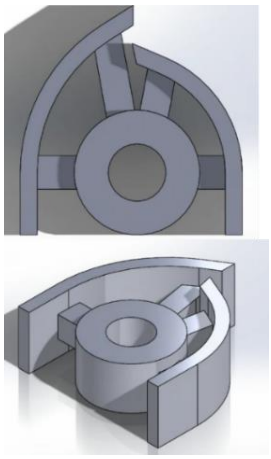

Figure 85: 3-D model of supports for radiation shield

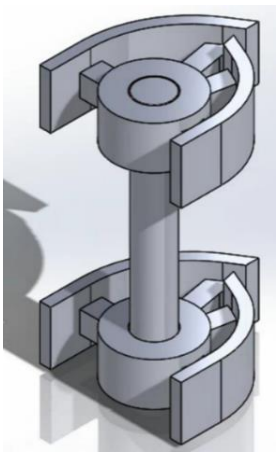

Figure 86: 3-D rendering of radiation shield supports on thermocouple probe

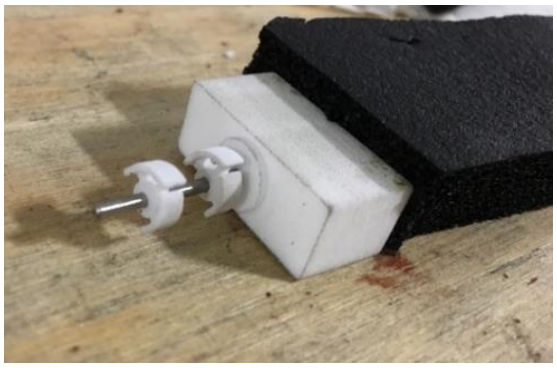

Figure 87: Supports for radiation shield on probe



Figure 88: Installed radiation shield

G.8 Construction Drawings

Figure 89 – Figure 92 display construction drawings and 3-D renderings of the air duct, polycarbonate viewing window, and integrated facility.

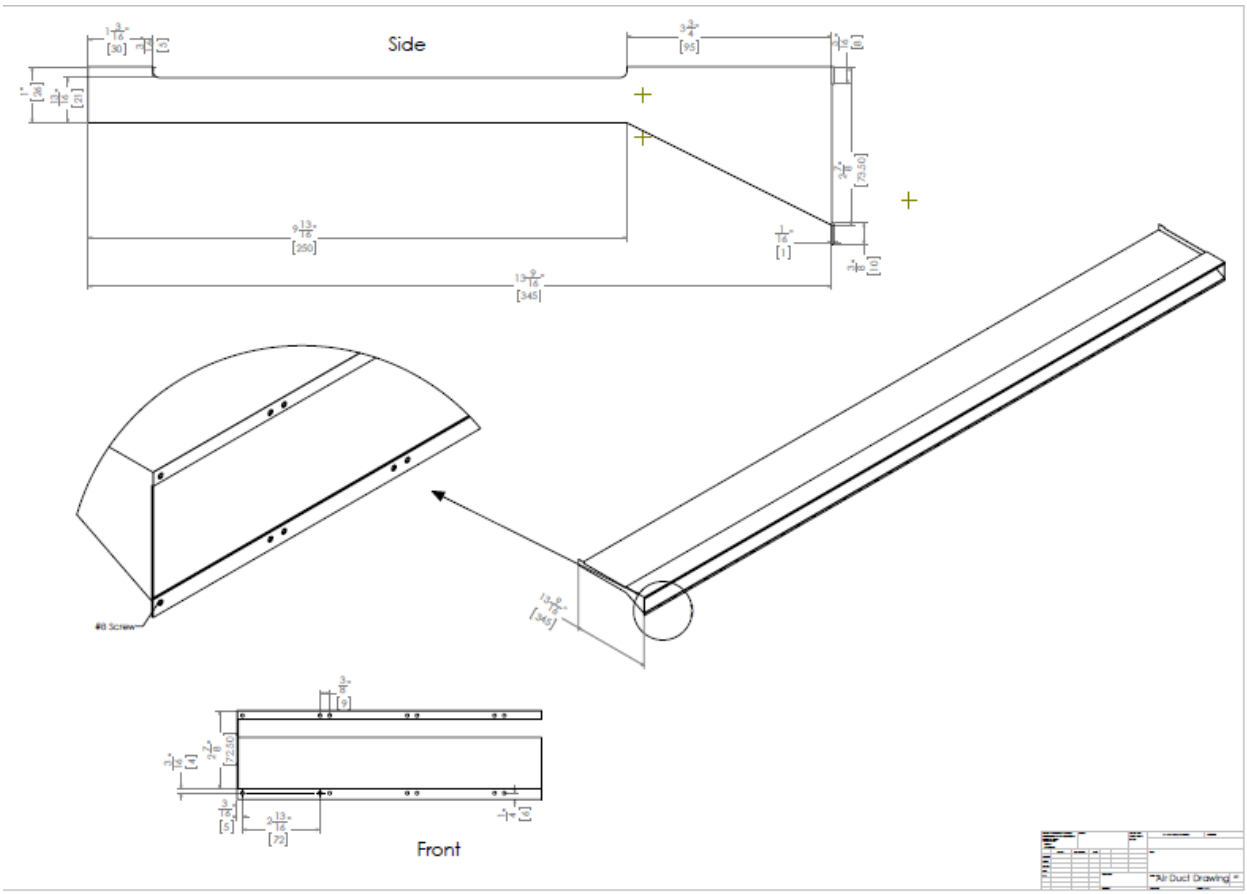

Figure 89: Air duct construction drawing

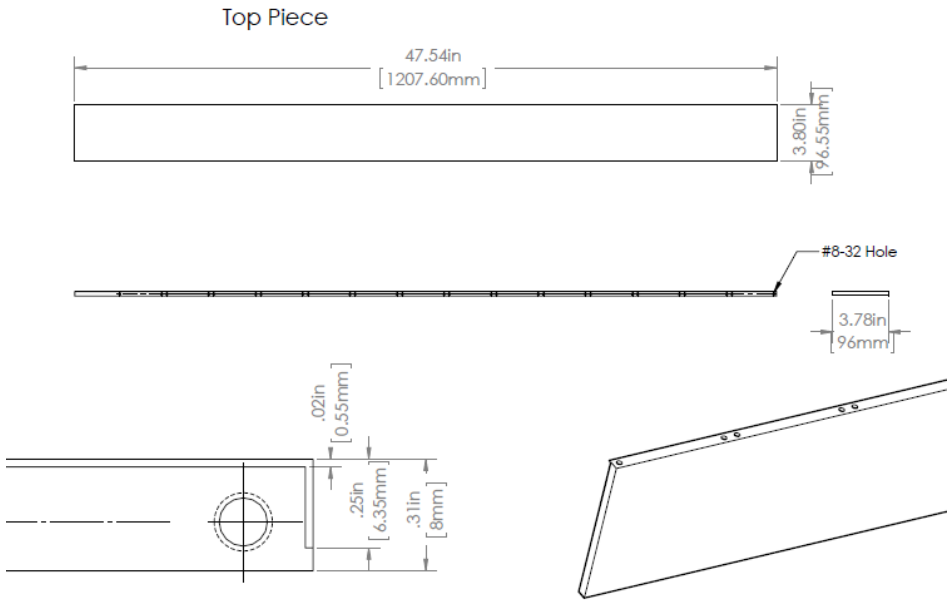

Figure 90: Air duct top segment construction drawing

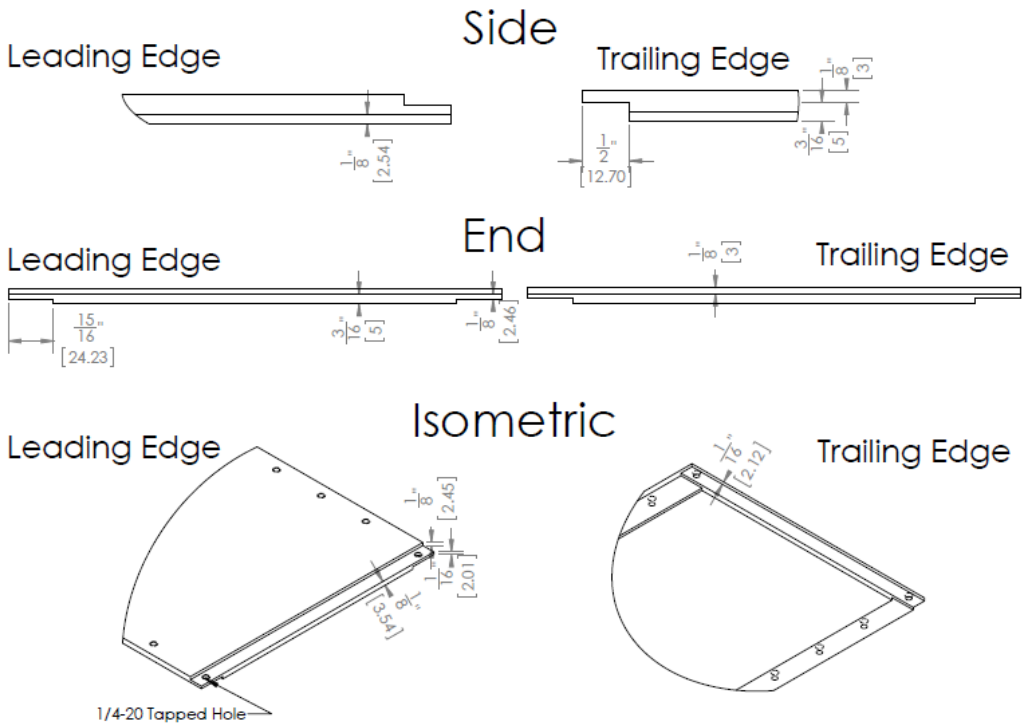

Figure 91: Polycarbonate viewing window construction drawing

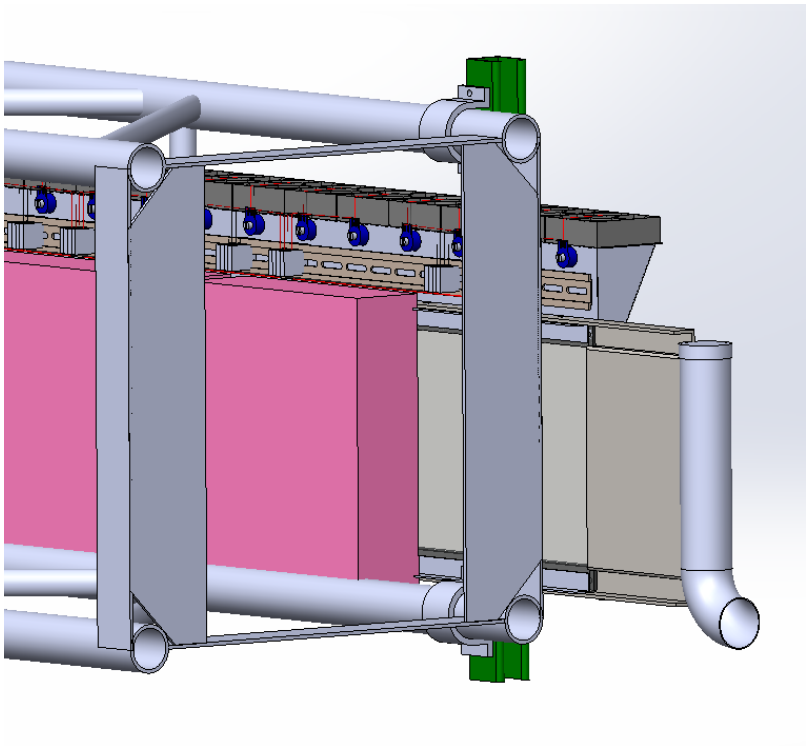

Figure 92: 3-D rendering of condenser tube, air duct, and supporting truss; pink insulation slid back to show detail below

Appendix H: Selected Temperature Measurements

Temperature measurements along the condenser are presented at three different inclinations: 0.3°, 6.0°, and 13.2°.

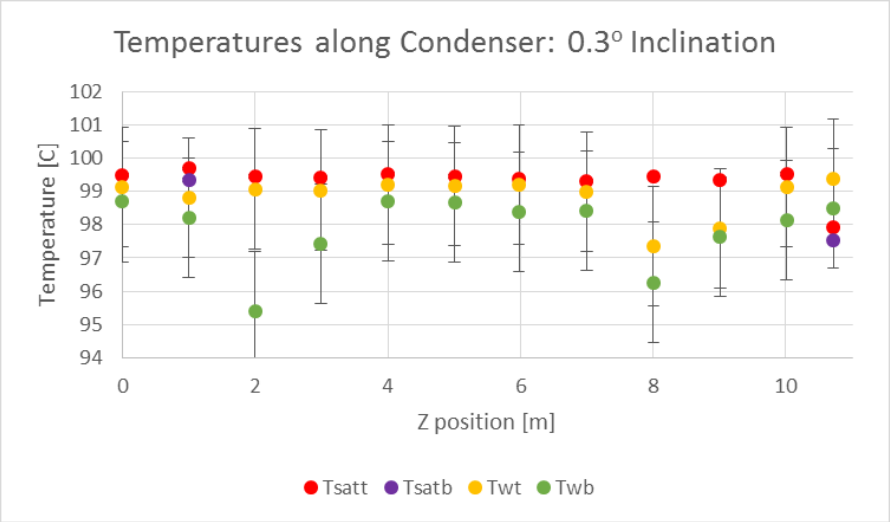

Figure 93: T_{satt}, T_{satb}, T_{wt}, T_{wb} along condenser at 0.3° inclination

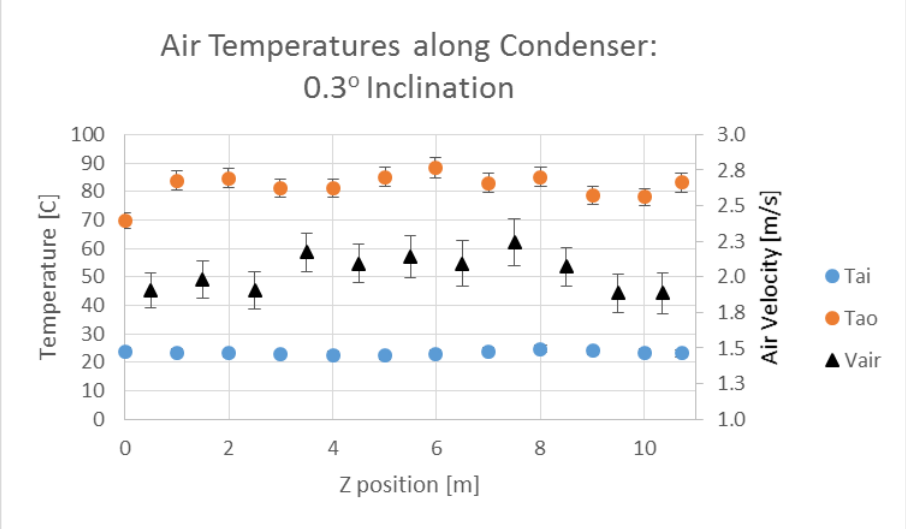

Figure 94: T_{ai}, T_{ao}, v_a along condenser at 0.3° inclination

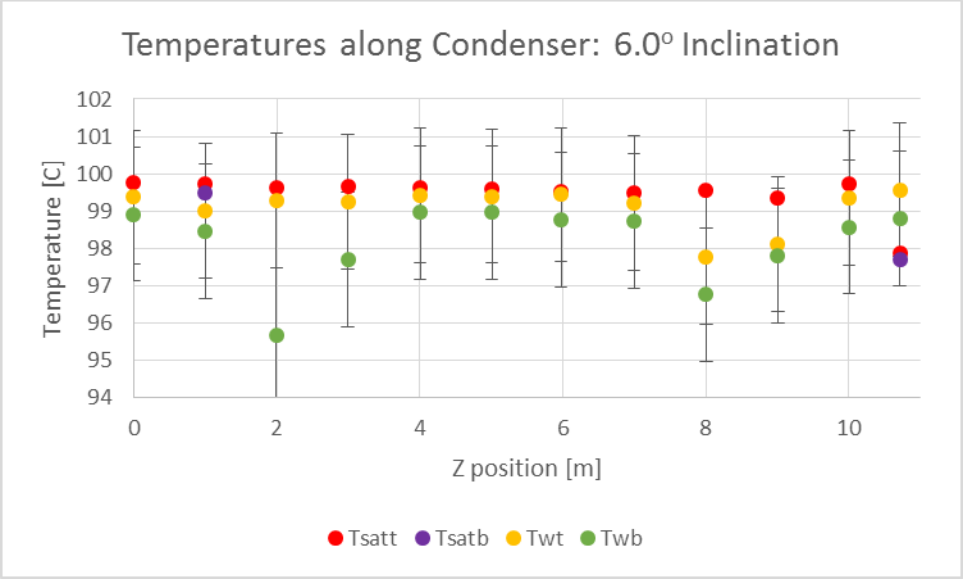

Figure 95: T_{satt}, T_{satb}, T_{wt}, T_{wb} along condenser at 6.0° inclination

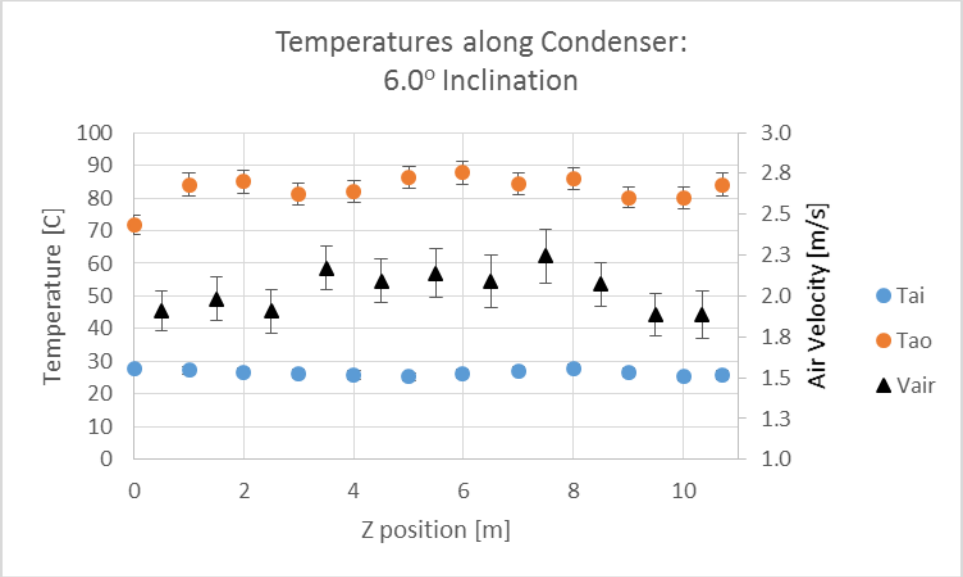

Figure 96: T_{ai}, T_{ao}, v_a along condenser at 6.0° inclination

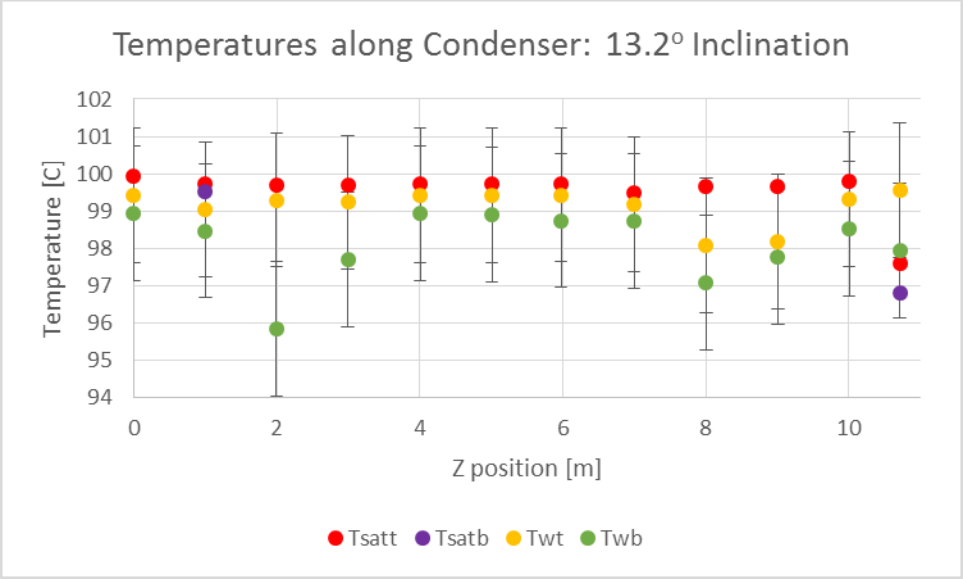

Figure 97: T_{satt}, T_{satb}, T_{wt}, T_{wb} along condenser at 13.2° inclination

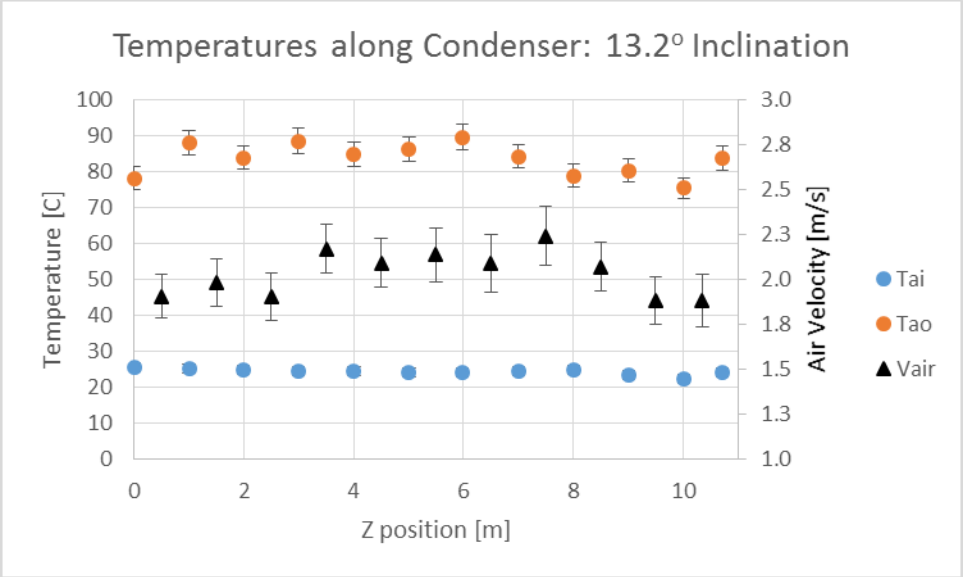

Figure 98: T_{ai}, T_{ao}, v_a along condenser at 13.2° inclination

Appendix I: Uncertainty

I.1 Instrument Uncertainties

Measured Variable	Instrument	Uncertainty
V_{air}	Alnor Compuflow 8585 Hot-Wire Anemometer	$\pm 3\%$ of reading
T_{satt}, T_{satb}, T_{ao}, T_{ai}, T_s, T_{amb}	Sheathed T-Type Thermocouple	$\pm 0.05\ K$
T_{wt}, T_{wb}, T_{at}, T_{ab}	Twisted T-Type Thermocouple	$\pm 0.16\ K$
P_{gauge}	Rosemount 1151 diaphragm differential pressure transducer, 0-30inH_2O	$\pm 7\ Pa$
ΔP_1	Rosemount 1151 diaphragm differential pressure transducer, 0-2inH_2O	$\pm 1\ Pa$
ΔP_2, ΔP_3	Rosemount 1151 diaphragm differential pressure transducer, 0-1inH_2O	$\pm 0.5\ Pa$
ΔP_4	Rosemount 1151 diaphragm differential pressure transducer, 0-0.5inH_2O	$\pm 0.25\ Pa$
ΔP_5	Rosemount 1151 diaphragm differential pressure transducer, 0-0.35inH_2O	$\pm 0.2\ Pa$
$\dot{m}_s$	Global Industrial Electronic Counting Scale	$\pm 0.5\ g$
H_T, F_P, F_T, H_a, dx	Pittsburgh 6" Composite Digital Caliper	$\pm\ .02\ mm$

I.2 Total Measurement Uncertainties

All uncertainties are reported at a 95% confidence interval. Uncertainty in measured quantities was determined by combining instrument, calibration, and statistical uncertainties for each measurement. Instrument uncertainty is the published accuracy of the measuring device. Calibration uncertainty was significant only for the v_{air} measurement. Statistical uncertainty was calculated as the standard error of the measurement, multiplied by a factor of 1.96 to convert to a 95% confidence interval (assuming a normal distribution of measurement data).

$$u_{stat} = \frac{Std.Dev.of\ Sample}{\sqrt{n}} \times 1.96$$

Statistical uncertainty was mitigated in most cases by taking a large quantity of measurements. However, statistical uncertainty was significant for v_{air}, T_{ai}, H_a, P_{gauge}, and H_T. T_{ao} had significant additional uncertainty due to uncertainty in position of the thermocouple. The steep gradient of the temperature profile in the air duct meant that a small change in thermocouple position could result in an large change in the temperature measured. This caused the large uncertainty in the T_{ao} measurement.

The instrument, calibration and statistical uncertainties were combined by using summation in quadrature:

$$u_{total} = \sqrt{{u_{ins}}^2 + {u_{cal}}^2 + {u_{stat}}^2}$$

Measured Variable	Total Uncertainty
v_{air}	$\pm 7\%$
T_{ao}	$\pm 4.1\%$
T_{ai}	$\pm 1.25^{o}C$
T_{atm}	$\pm 0.05^{o}C$
H_a	$\pm 2.8\%$
$\dot{m}_s$	$\pm 1\ g/s$
P_{gauge}	$\pm 1.6\%$
T_{satt}	$\pm .05^{o}C$
Duct Perimeter	$\pm 4\ mm$
F_p	$\pm .04\ mm$
H_T	$\pm 0.8\ mm$
dx	$\pm 2\ mm$
T_{at}, T_{ab}	$\pm 0.4\%$
T_{wb}, T_{wt}	$\pm 1.8℃$
φ	$\pm 0.4\%$
θ_{st}	$\pm 8.2°$
$t_{c,pc}$	$\pm 0.6\ mm$

I.3 Uncertainties of Determined Quantities

Uncertainty for determined quantities was found by assuming that all of the measurement uncertainties were independent and random, not systematic. The total uncertainty for each determined quantity was then found as the square-root of the sum of the squared partial derivatives, weighted by the component uncertainties [34]:

$$u_y = \sqrt{\sum_i \left(\frac{\partial y}{\partial x_i}\right)^2 {u_x}^2}$$

Uncertainty calculations were performed using the EES software.

I.3.1 Air-Side Heat Transfer, Q_a

Uncertainty in air-side heat transfer arose from measurement of air velocity, v_{air}, air temperatures, T_{ai} and T_{ao}, ambient temperature, T_{atm}, and air duct height, H_a. The largest uncertainty came from the T_{ao} and v_{air} measurements, each accounting for 40-45% of the total uncertainty in air-side heat transfer measurement in each section. Uncertainty in the H_a and v_a measurements accounted for approximately 5-8% of the uncertainty each. Uncertainty in air-side heat transfer measurements averaged 9% per section. Uncertainty in the total air-side heat transfer was only 2.7%.

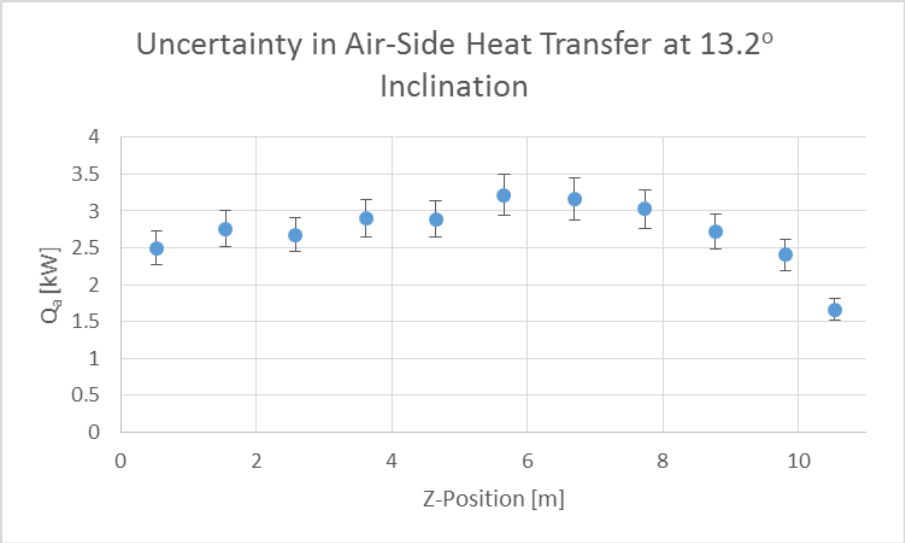

Figure 99: Uncertainty in Q_a at 13.2° inclination

I.3.2 Steam-Side Heat Transfer, Q_s

The uncertainty in finding steam-side heat transfer was caused by measurement uncertainty in $\dot{m}_s$ and T_{satt}, and uncertainty in calculating $UA_{loss,steam}$. T_{satt} was used to determine i_{fg} and to determine

the amount of superheat at the inlet to the condenser. Total uncertainty of Q_s was 10%. Nearly 100% of the uncertainty arose from the $\dot{m}_s$ measurement, and uncertainty caused by all other measurements was negligible.

I.3.3 Condensation Heat Transfer Coefficient, h_s

The uncertainty in the condensation heat transfer coefficient was affected by the majority of the system measurements recorded. However, the majority of the error was caused by uncertainties in T_{ao}. Total uncertainty ranged from 52% - 64%, and generally increased with an increase in inclination. T_{ao} measurements accounted for nearly 60% of the uncertainty, followed by fin pitch, F_p, at 23% and fin thickness, F_t, at 10%.

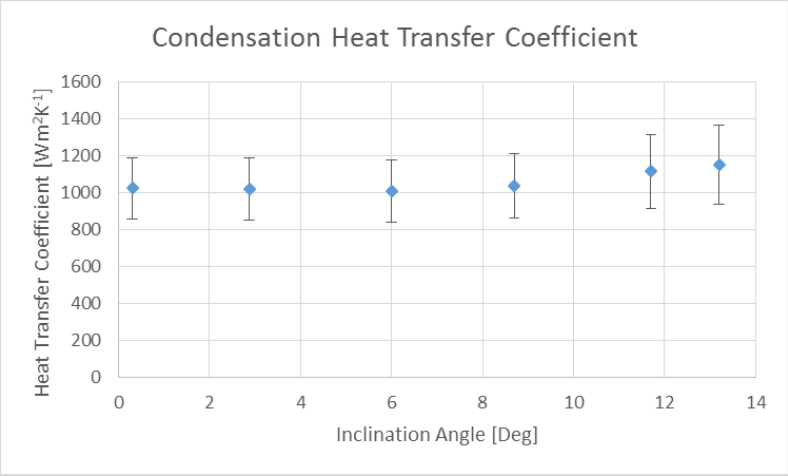

Figure 100: Uncertainty in condensation heat transfer coefficient

Table 13: Summary of leading causes of uncertainty in h_s calculation

Quantity	% of uncertainty
T_{ao}	59%
F_p	22.5%
F_t	10.4%
$\dot{m}_s$	3.1%
V_{air}	3.1%
Peri	1.1%

I.3.4 Heat Loss Calibration, UA_{loss}

Only three data points were taken for calculating $UA_{loss,s}$ and $UA_{loss,a}$, with an average uncertainty of 11% for each point. The overall uncertainty for $UA_{loss,s}$ was 2%, and 11% for $UA_{loss,a}$ the higher uncertainty for $UA_{loss,a}$ was due to uncertainty in separating the excess heat loss from the heat lost by the air over the measurement section. Neither uncertainty had a large effect on any of the other measurements, due to the small magnitudes of UA_{loss}.

I.3.5 $h_{s,local}$

Uncertainty in local steam HTC was very high due to the small temperature difference between saturation temperature and wall temperature. In addition, there was a large uncertainty (0.95° C) in measuring wall temperature. Uncertainty in $h_{s,local}$ ranged from 33-292%, with an average of 138%.

I.3.6 Condensate River Depth

Condensate river depth, t_c, was determined from measurements of the condensate river height on the polycarbonate, $t_{c,pc}$ and of the contact angle of water on steel, θ_{st}. Uncertainty in condensate river depth was $\pm 0.8\, mm$, with 52% of the uncertainty caused by uncertainty in θ_{st} and 48% caused by uncertainty in $t_{c,pc}$.

References

[1] E. Shuster, *Estimating freshwater needs to meet future thermoelectric generation requirements*: National Energy Technology Laboratory, 2007.

[2] R. Goldstein, "Water Use for Electric Power Generation," 2008.

[3] W. Nusselt, "Die Oberflachenkondesation des Wasserdamffes the surface condensation of water," *Zetrschr. Ver. Deutch. Ing.,* vol. 60, pp. 541-546, 1916.

[4] M. Shah, "A general correlation for heat transfer during film condensation inside pipes," *International Journal of heat and mass transfer,* vol. 22, pp. 547-556, 1979.

[5] M. Soliman, J. Schuster, and P. Berenson, "A general heat transfer correlation for annular flow condensation," *Journal of Heat Transfer,* vol. 90, pp. 267-274, 1968.

[6] D. P. Traviss, W. M. Rohsenow, and A. B. Baron, "Forced Convective Condensation in Tubes: A Heat Transfer Correlation for Condenser Design," *ASHRAE Transactions,* vol. 79, pp. 157-165, 1972.

[7] J. C. Chato, "Laminar condensation inside horizontal and inclined tubes," Massachusetts Institute of Technology, 1960.

[8] H. Jaster and P. Kosky, "Condensation heat transfer in a mixed flow regime," *International Journal of Heat and Mass Transfer,* vol. 19, pp. 95-99, 1976.

[9] B. Metais and E. Eckert, "Forced, mixed, and free convection regimes," *Journal of Heat Transfer,* vol. 86, pp. 295-296, 1964.

[10] S. Lips and J. P. Meyer, "Experimental study of convective condensation in an inclined smooth tube. Part I: Inclination effect on flow pattern and heat transfer coefficient," *International Journal of Heat and Mass Transfer,* vol. 55, pp. 395-404, 2012.

[11] S. Noie, M. Sarmasti Emami, and M. Khoshnoodi, "Effect of inclination angle and filling ratio on thermal performance of a two-phase closed thermosyphon under normal operating conditions," *Heat transfer engineering,* vol. 28, pp. 365-371, 2007.

[12] Y. Lyulin, I. Marchuk, S. Chikov, and O. Kabov, "Experimental study of laminar convective condensation of pure vapor inside an inclined circular tube," *Microgravity Science and Technology,* vol. 23, pp. 439-445, 2011.

[13] S. Olivier, J. Meyer, M. De Paepe, and K. De Kerpel, "Measured void fraction and heat transfer coefficients during condensation," in *11th International Conference on Heat Transfer, Fluid Mechanics and Thermodynamics (HEFAT)*, 2015, pp. 408-416.

[14] R. Würfel, T. Kreutzer, and W. Fratzscher, "Turbulence transfer processes in adiabatic and condensing film flow in an inclined tube," *Chemical Engineering and Technology,* vol. 26, pp. 439-448, 2003.

[15] M. Akhavan-Behabadi, R. Kumar, and S. Mohseni, "Condensation heat transfer of R-134a inside a microfin tube with different tube inclinations," *International Journal of Heat and Mass Transfer,* vol. 50, pp. 4864-4871, 2007.

[16] B.-X. Wang and X.-Z. Du, "Study on laminar film-wise condensation for vapor flow in an inclined small/mini-diameter tube," *International journal of heat and mass transfer,* vol. 43, pp. 1859-1868, 2000.

[17] T. Cheng, X. Du, L. Yang, and Y. Yang, "Co-current Condensation in an Inclined Air-cooled Flat Tube with Fins," *Energy Procedia,* vol. 75, pp. 3154-3161, 2015.

[18] D. H. Beggs and J. P. Brill, "A study of two-phase flow in inclined pipes," *Journal of Petroleum technology,* vol. 25, pp. 607-617, 1973.

[19] V. P. Carey, *Liquid-Vapor Phase-Change Phenomena*. New York: CRC Press, 2008.

[20] F. Schulenberg, "Wärmeübergang und Druckverlust bei der Kondensation von Kältemittel-Dämpfen in luftgekühlten Kondensatoren," *Kältetechnik-Klimatisierung,* vol. 22, pp. 75-81, 1970.
[21] D. G. Kröger, *Air-cooled heat exchangers and cooling towers* vol. 1: PennWell Books, 2004.
[22] R. K. Shah and A. L. London, *Laminar flow forced convection in ducts: a source book for compact heat exchanger analytical data*: Academic press, 2014.
[23] M. Jamil, "Laminar Forced Convection in Noncircular Ducts," MS Thesis, University of Alberta, 1967-Joshi, HM and Webb, RL," Heat'hansfer and F'riction in the Offset Strip Fin Heat Exchanger", International Journal of Heat and Mus Tbansfer, 1987.
[24] J. Zarling, "Application of Schwarz-Neumann technique to fully developed laminar heat transfer in noncircular ducts," *Journal of Heat Transfer,* vol. 99, pp. 332-335, 1977.
[25] X. P. Wu, L. J. Yang, X. Z. Du, and Y. P. Yang, "Flow and heat transfer characteristics of indirect dry cooling system with horizontal heat exchange A-frames at ambient winds," *International Journal of Thermal Sciences,* vol. 79, pp. 161-175, 2014.
[26] K. Hooman, "Dry cooling towers as condensers for geothermal power plants," *International Communications in Heat and Mass Transfer,* vol. 37, pp. 1215-1220, 2010.
[27] Q.-d. Wei, B.-y. Zhang, K.-q. Liu, X.-d. Du, and X.-z. Meng, "A study of the unfavorable effects of wind on the cooling efficiency of dry cooling towers," *Journal of wind engineering and industrial aerodynamics,* vol. 54, pp. 633-643, 1995.
[28] V. Gadhamshetty, N. Nirmalakhandan, M. Myint, and C. Ricketts, "Improving air-cooled condenser performance in combined cycle power plants," *Journal of energy engineering,* vol. 132, pp. 81-88, 2006.
[29] D. Enterprises. (2016, 4/7). *Critical Surface Tension and Contact Angle with Water for Various Polymers*. Available: https://www.accudynetest.com/polytable_03.html?sortby=contact_angle#branding
[30] N. C. Markatos and K. Pericleous, "Laminar and turbulent natural convection in an enclosed cavity," *International Journal of Heat and Mass Transfer,* vol. 27, pp. 755-772, 1984.
[31] M. R. de Santiago and C. Marvillet, "Pool entrainment phenomenon: Measurement of size and velocity distributions of droplets at several distances above the bubbling surface," *International communications in heat and mass transfer,* vol. 18, pp. 207-218, 1991.
[32] L. Sterman, "On the theory of steam separation," *Soviet Physics-Technical Physics,* vol. 3, pp. 1440-1451, 1958.
[33] F. Incropera and D. DeWitt, "Fundamentals of Heat and Mass Transfer, Wiley, New York, 1996."
[34] B. N. Taylor and C. E. Kuyatt, "NIST technical note 1297," *Guidelines for evaluating and expressing the uncertainty of NIST measurement results,* p. 24, 1994.